UCL
Université catholique de Louvain

Faculté des Bioingénieurs

Using GPR to analyze regeneration success of cork oaks in the Maâmora forest (Morocco)

Présenté par Aurore de Mahieu

Co-promoteurs :	Prof. Sébastien LAMBOT (UCL/ELI/ELIE) Prof. Quentin PONETTE (UCL/ELI/ELIE)
Lecteurs :	Prof. Bruno DELVAUX (UCL/ELI/ELIE) Prof. Fouad MOUNIR (ENFI)

Mémoire de fin d'études présenté en vue de l'obtention du diplôme de **Bioingénieur**:
Sciences et technologies de l'environnement

AGRO LOUVAIN
BIOINGÉNIEURS

Année académique 2017-2018

The journey undertaken as part of this present work was made possible thanks to the financial support of the Académie de recherche et d'enseignement supérieur de la Fédération Wallonie-Bruxelles, Belgium as part of its development cooperation policy.

Acknowledgment

I would first like to thank my supervisors Prof. Sébastien Lambot and Prof. Quentin Ponette of the Université catholique de Louvain (UCL). Prof. Lambot's office was always open whenever I had questions regarding my research or my writing. I would also like to thank him for accompanying me to Morocco for the ground-penetrating radar measurements campaign and for his precious time and help regarding the post-treatment of the radar data. Prof. Ponette was also available to provide good advice and help me throughout the writing of this thesis.

I would like to acknowledge Prof. Fouad Mounir of the National School of Forestry Engineers of Salé (ENFI). He supported me during my stay in Morocco and shared whatever information I needed regarding my thesis. Mr. Brahim Ahsissou and Mr. Arbi Elhakour, driver and technician of ENFI, respectively, deserve my acknowledgment as well for their help, enthusiasm and good spirit in the field. Thanks to Mr. Saïd Harati and Mr. Hafid Chafori, soil technicians of the National Institute of Agricultural Research of Rabat (INRA) for their assistance throughout the soil analyses. Thank you as well to Mrs. Anne Iserentant, laboratory assistant of the UCL for guiding me through the soil laboratories. I'd also like to thank M. Frédéric André, UCL technician for building the horn dipole antenna.

Finally, I'd like to express my profound gratitude to my friends and family: Amal, my roommate in Morocco who was great company during my stay at ENFI, my bioengineer mates who made these few years memorable and last but not least, my parents for providing me with unfailing support and continuous encouragement since the very beginning.

I have learned a lot during this Master thesis research and I hope you will find my work as interesting and knowledge earning as I have.

Contents

List of Figures

List of Tables

Introduction

Forests play an important role in our world's ecosystem. They provide shade and shelter for many animal species, regulate water flow, prevent soil erosion and mitigate climate change. Forests also guarantee food security of hundreds of millions of people for the different sources they provide such as food, energy and income (FAO, 2016). Thus, we depend on forests, yet we are allowing them to disappear.

The Kingdom of Morocco is composed of 5 814 000 ha of forests (FAO, 2016) which represent about 13 % of the country's total area. It is covered by 65 % of deciduous species such as cork oaks, holm oaks or Saharan acacias, 20 % of conifers (cedars, thujas, pines, cypress or firs) and 15 % of scrubs and secondary species. In the past several decades, Moroccan forests have been suffering from degradation, yet they play an important economic and social role. Nowadays, many strategic plans are established in order to plant forests and maintain the ecological and environmental balances. Hence, about 500 000 ha are planted forests in Morocco.

Many studies have focused on the case of the Maâmora forest, located in the North-West of Morocco, between Rabat and Kénitra. With a total area of 133 000 ha, it is known as one of the world's largest cork oak stand (Fennane, 2015). The forest consists of about 65 000 ha of cork oaks, while the rest of its area is covered by introduced species such as eucalyptus, acacia and maritime pine. The Maâmora forest plays important economic, environmental and social functions. Unfortunately, it is subject to anthropic pressure with abusive exploitation of forest products (cork, wood, acorns,...) and overgrazing. This leads to harmful consequences on the regeneration of the forest (Lahssini, 2015). Despite many efforts of conservation and management, cork oak regeneration remains erratic and huge efforts must be undertaken.

In addition, climate also plays a role in the regressive trends of this forest. The bioclimate is sub-humid in the western part of the forest but semi-arid in the central and eastern parts. A decreasing rainfall gradient from West to East is observable and is likely to amplify in the future. Hence climate change must also be taken into account in the future regeneration of cork oak plots. Moreover, studies identified that water balance (climate and soil factors) is one of the main factor that regulates the success of cork oak regeneration (Lahssini, 2015). In fact, Maâmora's soil is composed of a more or less deep sand layer (0.3 m - 6 m) laying above a clay layer. This seems to be crucial for the success of cork oak seedlings and tree growth (Lepoutre, 1965).

This introduces the topic of this present thesis. The overall aim is to study the relationship between the growth of cork oaks and soil factors using GPR techniques. The forest plot chosen for this study is located in the B canton and has a high variability in terms of tree growth and regeneration success. Artificially regenerated in 1999 using acorn seedlings, many cork oaks of this plot have suffered from different kinds of pressure as evidenced by their relatively low heights and circumferences and low survival rates in distinct areas.

More specifically, to achieve the aim of this thesis, we subdivided the topic into two main sub-objectives. The first one consists of setting up a lightweight frequency domain ground-penetrating radar (GPR). The second one consists of studying the vigor of cork oak trees and detecting the soil properties that can lead to successful cork oak regeneration. In order to analyze this relationship, soil surveys down to 2 meters deep were performed, soil moisture mapping was carried out, past historic GPR data were analyzed and dendrometric measurements were taken to study the vigor of the cork oaks.

GPR is a rising sensing tool used to characterize subsurface structures and properties in many kinds of applications. Electromagnetic energy is transmitted towards the ground through an antenna. The transmitted energy is reflected from different interfaces and an antenna receives the back-scattered signal. The analysis of this reflected signal enables the estimation of soil layer depths and different soil characteristics like water content. The Lambot *et al.* approach was chosen for this study: it relies on a stepped-frequency continuous-wave radar joined with an off-ground monostatic electromagnetic horn antenna developed in the Georadar Research Centre of the Université catholique de Louvain. Preliminary antenna calibration and laboratory tests were accomplished in order to use this new radar system in the Maâmora forest.

The present thesis is organized as follows. A first part describes the general context of the Maâmora forest and the ecology of the cork oak (e.g., Chapter 1). Then, in a second part, the general principles of GPR are explained. More detailed theory is presented as well as the Lambot *et al.* methodology. Later, the different phases in the elaboration of our radar system are presented (e.g., Chapter 2). The third chapter details the different field measurements we conducted and we deepen the material and methodologies sections for each kind of measurement (GPR, dendrometric and soil). Finally, the results are presented and analyzed in Chapter 4, followed by a discussion.

Chapter 1

The Maâmora forest

1.1 General context

The Maâmora forest is considered as one of the world's largest cork oak forest (Belghazi, 2011). Located in North-West Morocco, between Rabat-Salé and Kénitra, it stretches from the Atlantic Ocean up to 70 km inland. With a total area of 133 000 ha, it is divided into 5 cantons from West to East (Cantons A, B, C, D and E). Each canton is divided into a number of groups (total of 33 groups) which contain a total of 450 forest plots. Figure 1.1 illustrates the geographical location of the Maâmora forest.

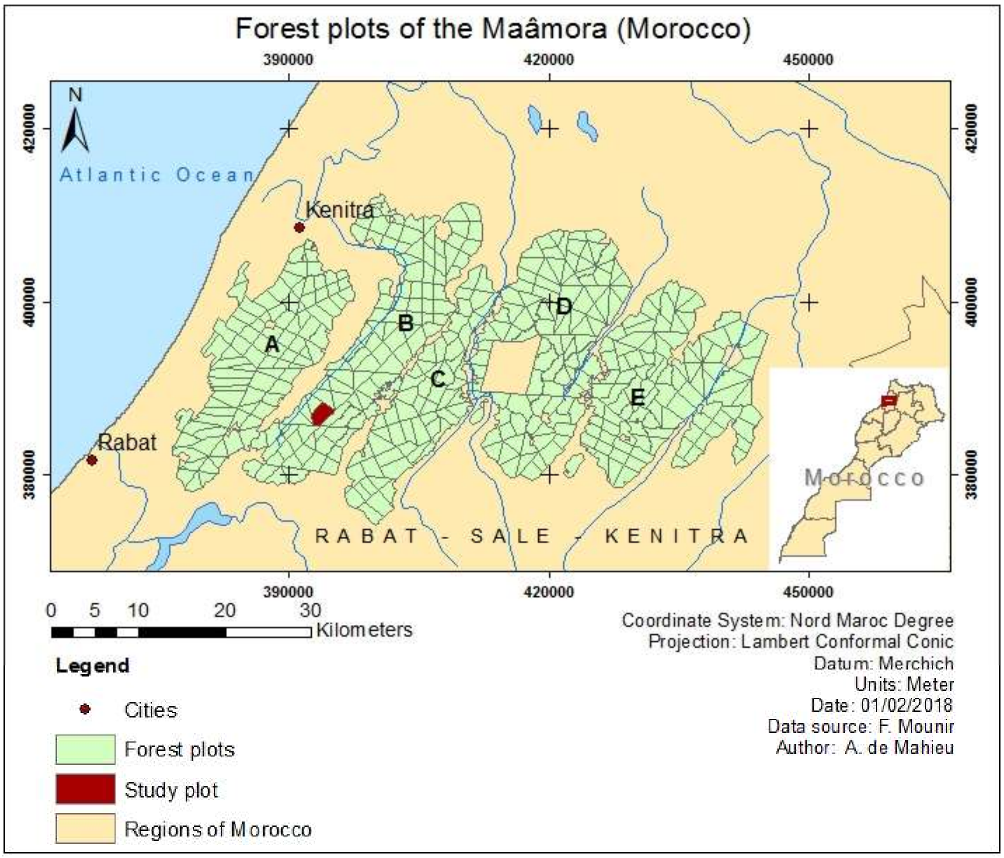

Figure 1.1: Geographical location of the Maâmora forest, subdivided into 5 cantons and into 450 forest plots.

1.2 Physical context

1.2.1 Climate

Bioclimate of Maâmora is sub-humid in the western part of the forest and semi-arid in its central and eastern parts. A decreasing rainfall gradient is observed from West to East. The isohyet map in Figure 1.2 illustrates this decreasing rainfall gradient. The rainy season occurs between November and March/April. December is the most humid month with 120 mm of cumulative rainfall while July is the driest month with less than 1 mm. The total annual rainfall ranges from 300 mm (driest) to 700 mm (most humid) according to the year and latitude (Mustapha, 2013). Finally, the maximum temperature fluctuates between 26°C and 35°C in summer and the minimum between 5°C and 8°C in winter. The mean monthly temperatures and cumulative rainfall are illustrated in Figure 1.3.

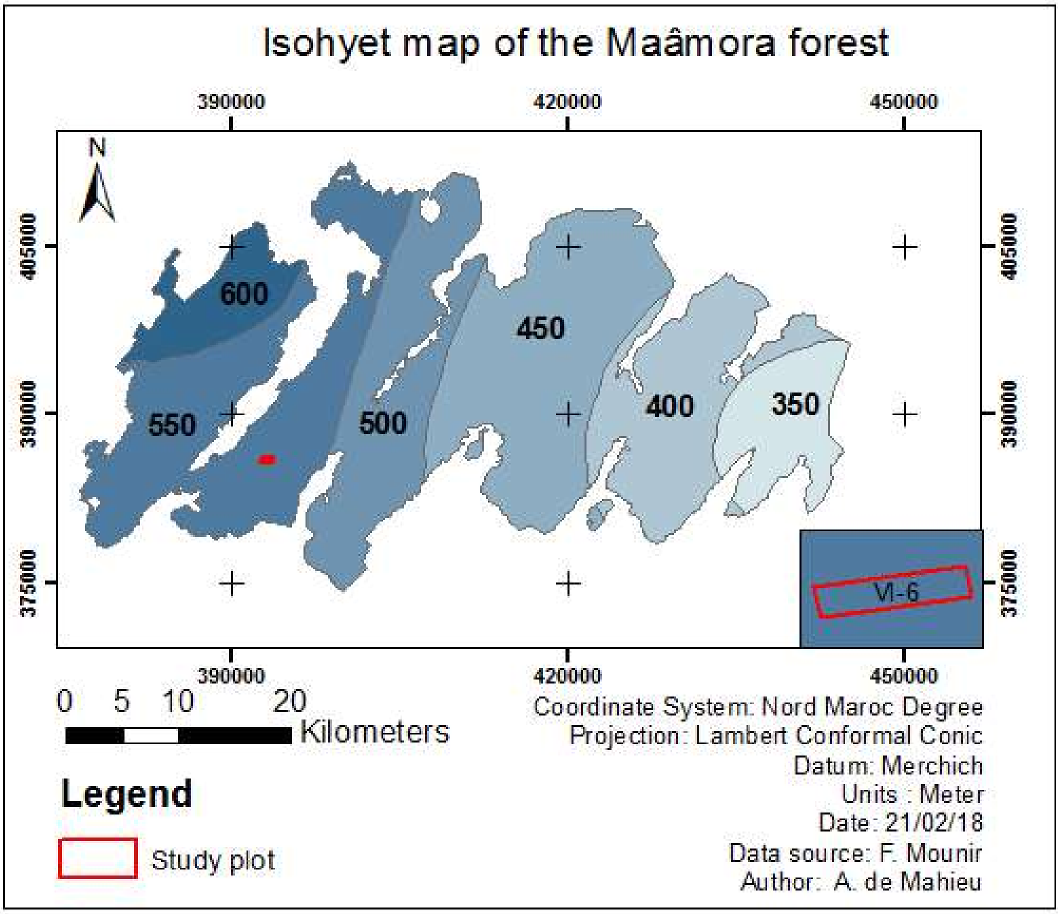

Figure 1.2: Isohyet map of the Maâmora forest representing the mean total annual rainfall [mm] distribution.

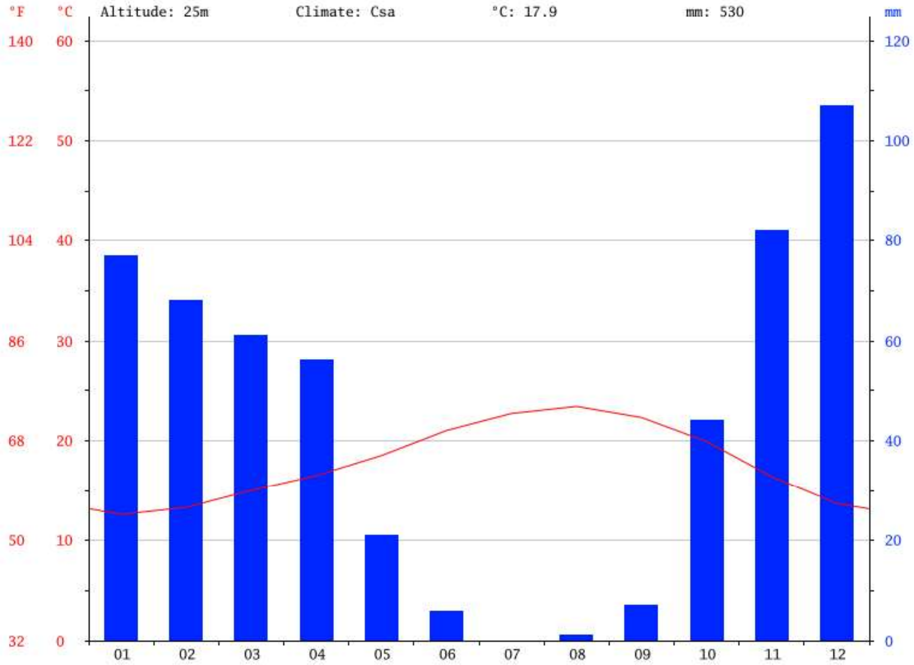

Figure 1.3: Mean temperatures and precipitations in Salé (1982-2012) [9].

1.2.2 Vegetation

Main tree species

Figure 1.4 shows the distribution of tree species in the Maâmora forest. As mentioned before, Maâmora covers about 133 000 ha. Essentially composed of cork oak (*Quercus suber*) by the middle of the 20th century, a net regression of 30 % has been estimated since then. This is due to problems in regeneration and successive periods of drought throughout the century. Overgrazing and human activity are also important factors that pressure the forest. To address these problems, the Forestry Administration implemented over the years various development and management plans. The decline in cork oak areas was offset with the plantation of more productive species such as eucalyptus, maritime pines or acacias. Table 1.1 illustrates the evolution of the forest area over the years.

Table 1.1: Evolution of the forest area according to tree species in Maâmora (Said, 2010).

Species	**Area [ha]**			
	1951	**1972**	**1992**	**2006**
Quercus suber	100 000	87 000	60 000	64 450
Eucalyptus	31 000	38 000	53 000	48 140
Acacia	500	1000	5500	5604
Pinus pinaster	1000	6000	12 500	13 806
Other species	1000	1000	2000	1500
Total	**133 500**	**133 500**	**133 500**	**133 500**

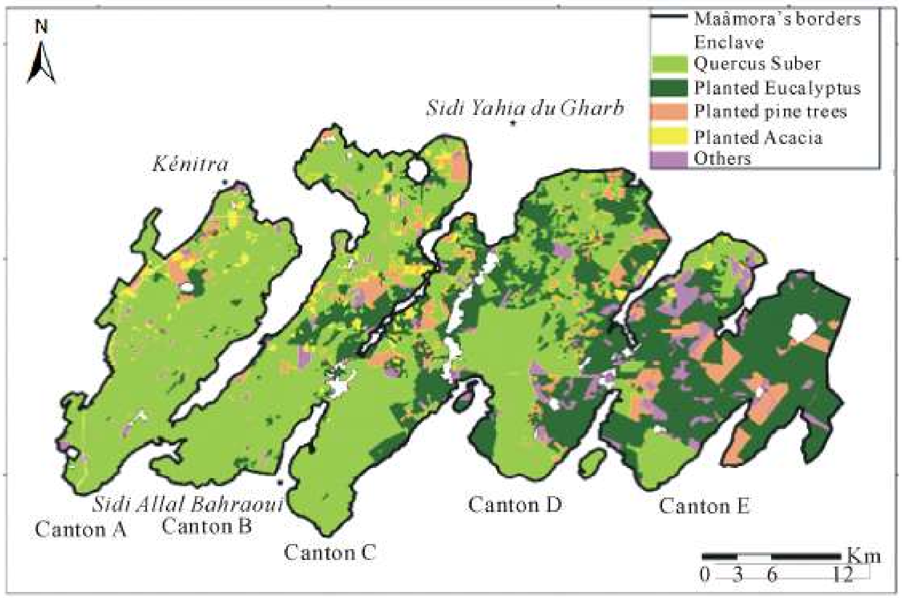

Figure 1.4: Distribution of the main tree species in the Maâmora forest: cork oak (*Quercus suber*), planted eucalyptus, planted pine trees and planted acacia (Lahssini, 2015).

Unlike cork oak, eucalyptus is unresponsive to sand depth because its rapid growth allows its roots to reach 4 m deep in the first winter. This species succeeds almost everywhere in the Maâmora. Pines also grow rapidly: maritime pine roots can reach 3 m deep and will adapt in areas where the sand reaches this depth (Lepoutre, 1965). Finally cork oak is very sensitive to sand depth; this will be discussed later in this chapter.

Many studies on the regeneration of cork oak have been undertaken in order to rehabilitate this species in the Maâmora (Artigues, [3], Bagaram, [4], Belghazi, [6], de Beaucorps, [11], El Boukhari, [17], Lahssini, [33], Lepoutre, [41],...). These studies revealed that climate and soil combined with human pressure are the principal factors that determine the success or failure of cork oak seedlings. This past decade, more than 20 000 ha of cork oaks have been planted (Lahssini, 2015).

Vegetative cover

The vegetative cover is characterized by psammophile[1] and acidophile species. Brooms (*Genista linifolia*), passerines (*Thymelaea lythroïdes*) and dwarf palms (*Chamaerops humilis*) are regularly found in the Maâmora and are resistant to cattle. Dwarf palm is a commonly used indicator of shallow sands. When this species is found in cork oak plots, this means that the clay layer is relatively close to the soil surface (de Beaucorps, 1956). Many cork oak seedlings are observed where the dwarf palm grows.

---

[1] that prefer or thrive in sandy areas.

1.2.3 Geology and pedology

The forest soils of Maâmora consist of a more or less deep sand layer that lies on top of a sandy-clay layer also called the "red clay of Maâmora". This clay is geologically dated from the Villafranchian period and the sands originate from a rearrangement by river [41] or wind [21] actions of the Quarternary sand spreading (Texier, 1992). The red clay of Maâmora contains a mixture of three clay minerals: kaolinite (45%), illite and montmorillonite. Small amounts of iron oxides are measured and free iron represent approximately 10% of the clay fraction. As kaolinite and illite are the main clay minerals, the cation exchange capacity is always low (10 - 30 meq/100 g) (Lepoutre, 1967).

The first soil layer is made of two types of sands: (i) red siliceous sands, rich in iron oxides that contain hematite and some clay, and (ii) pink to beige siliceous sands which are more recent then the first and do not contain any clay (Lepoutre, 1967). According to de Beaucorps (1956), the red sands contain 5 - 10 % of clay and 5 % of silt whereas the beige sands contain 0 - 2.5 % of clay and 5 % of silt. The red color is due to the hydration of the iron oxides which are subject to a more important water regime. The soil is completely deprived from limestone.

Hence, in the first sandy horizons, the percentages of clay are quite low but these percentages can increase up to 35 % in the red clay horizons. Moreover, the transition between the sand and clay layers can be abrupt but sometimes, a 10-cm transitional sandy-clay layer can be found between both horizons. Finally, the sand layer of the Maâmora has a variable thickness that ranges from 0.3 m to more than 6 m of depth. The map represented in Figure 1.5 shows the variation in sand depth. It was obtained using two digital elevation models (DEM): one of the natural elevation of the landscape and one of the elevation of the clay layer (Bagaram, 2014). Lepoutre (1965) discovered that sand depth and slope (i.e., depth and slope of the clay layer) are two parameters that influence cork oak seedling success. This is discussed in the next section of this chapter.

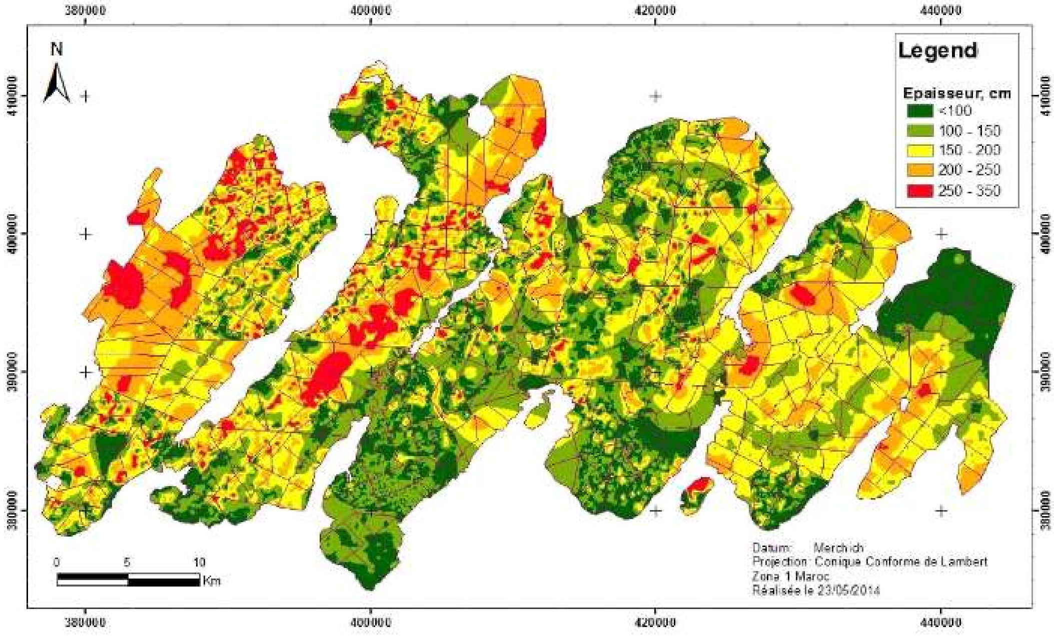

Figure 1.5: Variation in sand depths in the Maâmora forest (Bagaram, 2014).

Main soil types of Morocco are illustrated in the FAO74 map of Morocco in Figure A.1 (Appendix 1). According to this world soil classification, Maâmora forest is characterized by chromic luvisols. Luvisols have a surface horizon depleted of clay and an accumulation of clay in a subsurface "argic" horizon. This argic horizon starts within 1 m from the soil surface, or within 2 m if it is overlaid by loamy sand or coarser textures (FAO, 2001). Luvisols are commonly found in flat or gently sloping land in cool temperate regions and in warm (e.g., Mediterranean) regions with distinct dry and wet seasons. The main characteristic of luvisols is their argic illuviation horizon which is formed by translocation of clay from the surface horizon to the depth of accumulation (FAO, 2001).

More specifically, the main types of soils of the Maâmora forest are illustrated in Figure 1.6. Our study area is characterized by leached soils of deep pseudogley. Pseudogleys are hydromorphic soils which are characterized by a temporary perched water table due to insufficient drainage in rainy season (Duchaufour, 1992). This water table forms on top of a low-permeability horizon (i.e., clay layer). When the water table subsists, iron is reduced and complexed (FeO, anaerobic conditions); it migrates in the soil profile and precipitates when the water table disappears (Fe_2O_3, aerobic conditions). Iron presence is hence a good indicator of hydromorphy. The temporary water table and its anaerobic conditions can create asphyxiating conditions for tree roots during winter. Pseudogleys are generally acid soils as acidity enables iron reduction.

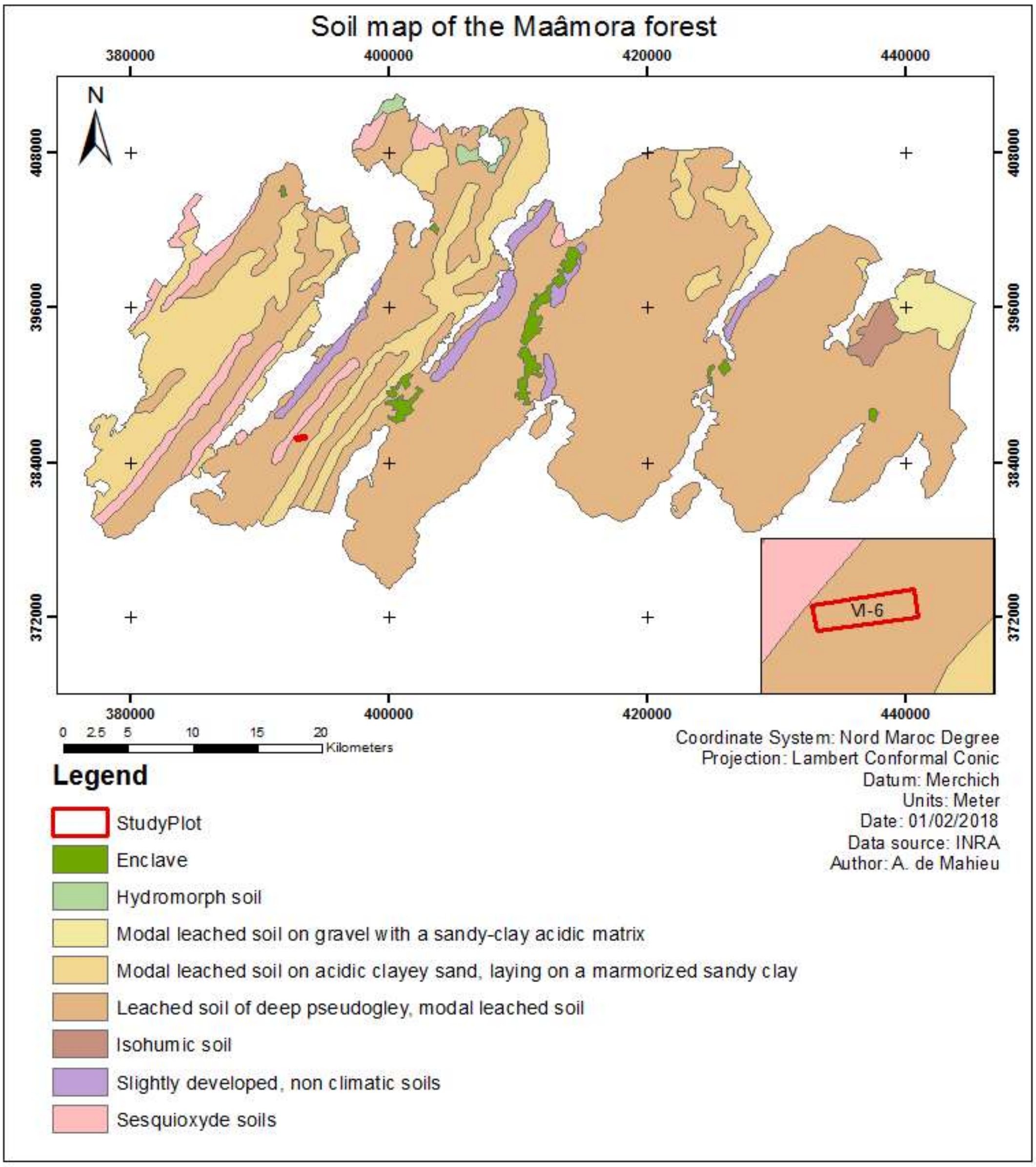

Figure 1.6: Main soil types of the Maâmora forest (INRA, 2015).

1.2.4 Relief and Hydrology

The Maâmora forest does not have a pronounced relief. The altitudes range from 30 m to 270 m from West to East (de Beaucorps, 1956). Cantons A and B are part of the western dunes which are characterized by an even relief and an important sand horizon with little erosion. C canton is part of the high central area with an uneven relief, abrupt valleys where erosion is more important. Finally the northern plots of cantons D and E belong to the low North-East area with low slopes and a sub-horizontal relief (Mustapha, 2013).

These five cantons are separated by five wadies. Wadies Fouarat, Smennto, Tiflèt, Touirza and Tarhereste (from West to East) drain the forest and flow towards the northern plain of Rharb and wadi Sebou. "Rharb" means West in Arabic and defines the Sebou plain which develops in North-West of Rabat (Monition, s.d.). These wadies have a low runoff because the sandy soils of the forest infiltrate most of the rainfall. Many dayas[2] can be found throughout the cantons. The groundwater table has an estimated area of 2120 km^2. Finally, small perched water tables can form on top of the red clay. Their shallow depth (1 m - 3 m) makes them to dry rapidly during summer (HCEF, 2015).

1.3 Cork oak, *Quercus suber*

1.3.1 Ecology

Cork oaks are found in southwestern Europe and northwestern Africa, including Portugal, Spain, France, Italy, Tunisia, Algeria and Morocco. A map of their natural distribution is found below in Figure 1.7. Portugal has the largest number of cork oaks and is the world leader of cork production. This evergreen species can reach heights of 20 meters and live up to 200 years (Aronson, 2009). Its particularity is its thick and dark grey cracked bark which can be harvested: cork. When the tree reaches 25 years, cork can be collected every 9-12 years without causing any damage. It is cut and peeled off and the tree will be able to regenerate its outer bark in the following years. The underlying trunk is coloured in red. This is illustrated in Figure 1.8.

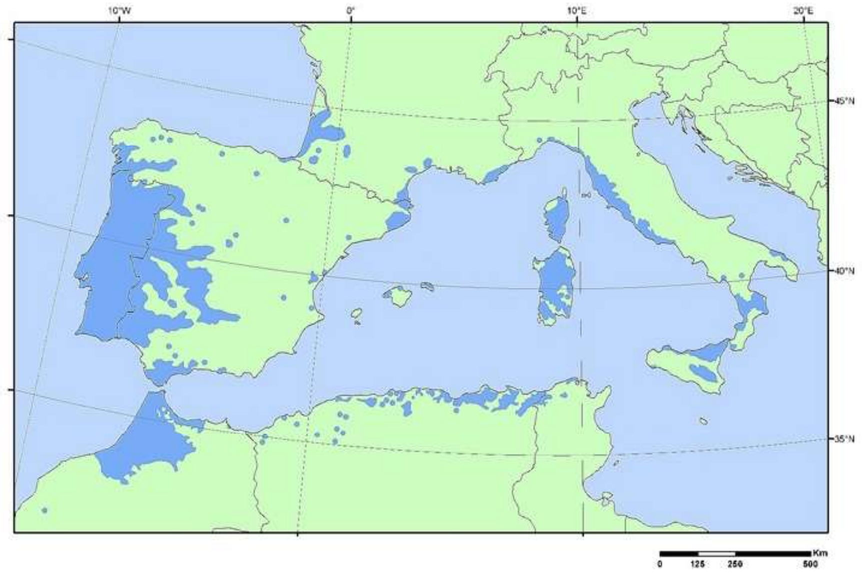

Figure 1.7: Natural cork oak distribution in the Mediterranean region: Portugal, Spain, France, Italy, Algeria, Tunisia and Morocco (Gil, 2008).

---

[2] shallow pits where rainfall temporarily accumulates.

Figure 1.8: Cork oaks of the Maâmora forest characterized by a thick and dark grey bark that can be harvested (Photo: A. de Mahieu, 2018).

Cork oak is a monoecious wind-pollinated species (Houston Durrant, 2016). The flowers appear during spring and can engender annual and biennial acorns. The production of acorns can vary from one year to another with extremely productive years followed by others with poor production. Leaves are sclerophyllous and oval shaped with a length of 4 cm -7 cm. Their colour is green on top and pale gray below.

The species requires an annual mean temperature of 15°C and does not tolerate temperatures below -10°C. It grows on non-calcareous substrates and prefers sandy and slightly structured soils. It can grow under various annual rainfalls: from 480 mm in Morocco up to 2400 mm in Portugal and Spain (Gil, 2008). It is a well adapted species to warm and dry climates: its vast and deep root system allows it to cope with droughts and it is also capable of closing the stomata of its leaves to control water loss (Houston Durant, 2016). Moreover, it is able to fight against fire thanks to its thick bark that protects its trunk.

Cork oak is an endemic species. Today it covers over 350 000 ha in Morocco: the principal forests are located in the occidental and central Rifs, in the Middle Atlas, the Maâmora and in the central Plain.

Root system

Cork oak has a tap root system: the main root travels deep into the soil giving the tree the support it needs. It also has secondary roots that are more shallow. The root system enables water and nutrient supply; it can pair with roots from neighboring trees (exchange of nutritive substances) or pair with fungi and form mycelia. Studies in Portugal have proven that this species has root activity in two soil layers: one at approximately 40 cm - 100 cm deep and the other that reaches the water table. The upper horizontal roots draw water and nutrients during the wet season and the deeper roots take this role over during the dry season after desiccation of the upper soil horizons (Aronson, 2009). In summer, leaf stomata close to limit transpiration. Finally, the deeper roots allow water distribution to the upper root system through hydraulic lift.

During the early stages of plant life, cork oak gives priority to root growth (Aronson, 2009). This will contribute to its survival in case of droughts during the first summers of growth. Seedling survival will in fact not occur if roots do not reach a soil depth that holds water in summer. Mycorrhizae are also an important aid for these seedlings to resist to drought. More precisely, the root system of young seedlings is composed of a main pivot that penetrates deep into the soil and a tracing root system that develops in the first 40 cm - 50 cm from the soil surface. According to the substrate conditions, the root system will vary. If the soil is well drained, the main pivot will be able to reach the clay layer (if it is not too deep) and it will then form ramifications. The tracing system is then well developed. On the contrary, if the soil is poorly drained and a temporary water table is found on top of the clay layer, the pivot will atrophy in the sandy layer (Lepoutre, 1965). When this water table disappears, the roots will remain in a dry sand and the seedlings will not be able to resist the dry conditions that follow winter.

1.3.2 Cork oak in the Maâmora forest

Economic and social role

Maâmora plays important ecological and socio-economic roles in Morocco. It also provides a recreational area for populations of neighboring agglomerations (Rabat, Salé, Kénitra) and is the main source of income for more than 300 000 inhabitants (Said, 2010). According to this author, the socio-economic importance emerges through a series of factors as presented in Table 1.2.

Table 1.2: Factors in connection with the economic and social development of the Maâmora forest (Said, 2010).

Cork	6000 t/yr
Firewood	600 000 m^3/yr
Wood industry	300 000 m^3/yr
Forage production	24.10^6 FU/yr (250 000 heads of sheep and cattle)
Non-wood products	Mushrooms, lichens (30 t/yr), medicinal plants and tannins (5000 t/yr), honey (1000 t/yr)
Total profit	**60.10^6 Dh ($\approx 660.10^6$ €)**

Unfortunately, as the needs of rural population have increased, the Maâmora is now under intense pressure. Degradation of the forest results from human activity among other factors. Illegal harvesting of wood, overgrazing, topping and pruning, collection of acorns or urbanization are some of the reasons that partly explain the regression of the forest this past century.

To remedy this situation, Maâmora has been subject to different management plans (1951-1971, 1972-1992, 1992-2012, 2005-2014,...) with clear objectives of regeneration and protection of cork oak and artificial reforestation. The main goal for 2014 was to reach 20 000 ha of cork oak reforestation. Moreover, a management plan for the next decade has been set (2015-2024) (Fennane, 2015).

Natural and artificial regeneration

As explained in the previous section, artificial regeneration is part of the management plans of the Maâmora forest. In fact, natural regeneration has been proven insufficient to guarantee the sustainability. El Boukhari (2015) - in agreement with other authors such as Marion (1951) or Lepoutre (1965) - justifies that adult cork oaks will disable natural regeneration because their is a strong competition for water supply. The implementation of artificial seedlings in plots where adult trees were not eliminated failed consistently for this reason (Lepoutre, 1965). Metro *et al.* (1957) showed that the root tracing system of cork oaks could reach a 20 m diameter and thus, natural regeneration can not occur easily. Hence, to have a successive regeneration, previous vegetation must be eliminated so that there is no competition for water, light and nutrition.

Artificial regeneration seems to be the solution; many researchers have been looking into the subject for the past decades. Different factors must be taken into account in order to guarantee the survival of the planted seedlings. We will briefly discuss the positive (and negative) impacts of these factors.

Lepoutre (1965) extensively studied the Maâmora forest in the 1960s. He was among the first to discuss regeneration of cork oak with de Beaucorps, Marion and Sauvage (1956). In the occidental Maâmora, he proved that the growth of cork oak seedlings is influenced by soil nature. Sand depth has a strong positive influence: if it is less than 2 m, seedlings grow unless excess water in winter drowns the root system (shallow sands) or, on the contrary, an excessive drainage occurs. Moreover, the roots must reach the clay layer in the first winter to have water supply for the following summer. Root growth can reach 2 meters on shallow slopes but can be limited to approximately 1 m if the slope exceeds 9-10 %. The existence of a perched water table prevents the pivot to go deeper and reach the clay whereas if the sand layer is too deep, the roots are not able to reach it during the first winter. The following summer, under dry conditions, the seedlings will not survive. In addition, red sands that contain more clay (7-10 %) ensure better water retention than beige sands and thus helps the seedling to grow. Finally, he confirmed that climate is a constraint for the success of cork oak regeneration. From West to East, lower rainfalls, drier conditions and a semi-arid bioclimate explain why the forest density is lower in the eastern cantons than in the western cantons.

Belghazi *et al.* (2011) studied ten strata of the forest located in all five cantons. They discovered that acorn seedlings survive better their first three years than planted seedlings. The nature of sands also has an impact: red sands are more fertile than beige sands because they contain clay that have a better water retention than beige sands which are leached out and retain no water for the vegetation. According to Belghazi, the sand depth does not have an impact on acorn seedlings if they are watered twice during their first summer. By adding water, the pivot of young seedlings will be able to grow rapidly and reach the clay layer thus preventing the plant to dry out the following summer. On the contrary, sand depth has a significant impact on planted seedlings. If they are watered twice, it is insufficient in this kind of environment and the root system will not be able to develop sufficiently. Finally, the continental character of the forest influences the survival rates. As seen above, survival rates will be higher in sub-humid cantons A and B.

Many authors have reached essentially similar conclusions to the ones presented in this section. Others tried to predict cork oak suitability in the forest (Lahssini, 2015; Bagaram, 2016) by offering tools to predict the priority areas in which cork oak regeneration should be considered. An example of a suitability map is illustrated in Figure 1.9.

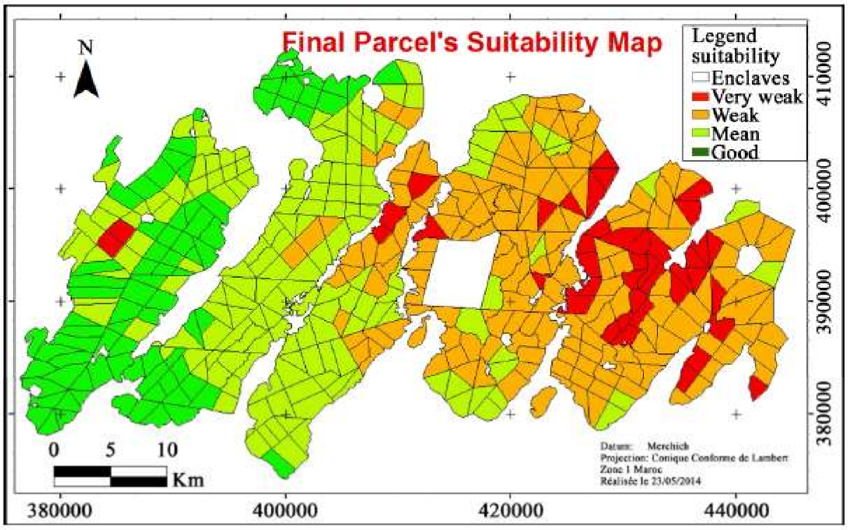

Figure 1.9: Map of the average regeneration suitability of cork oak in the Maâmora forest (Bagaram, 2016).

Chapter 2

Ground-penetrating radar: Theory and methodology

In this chapter, GPR theory is discussed so that an uninformed reader can understand the functioning of the radar. The basic principles of GPR are first presented, then, a few theoretical aspects of GPR and the Lambot *et al.* methodology are detailed. Finally, this chapter describes the setup of the specific radar system dedicated to our application.

2.1 Theory

2.1.1 GPR as a soil subsurface properties characterization method

A ground-penetrating radar (GPR) is a near-surface remote sensing tool used to detect buried objects and to characterize subsurface structures and properties in a wide variety of applications (Lambot, 2004).

GPR consists of an emitting antenna (Tx), a receiving antenna (Rx) and an electronic system that allows the generation and recording of the emitted and received signals. The basic principle is illustrated in Figure 2.1. GPR operates by transmitting microwave electromagnetic energy down into the ground through an antenna. The transmitted energy is reflected by various electromagnetic interfaces. The antenna then receives the reflected signal. Note that the GPR can consist of one unique antenna (that plays both roles of emitting and receiving the signal) or two distinct antennas. The analysis of the reflected signals enables the detection of different soil structures, the estimation of soil depth and the determination of different soil characteristics such as water content.

Dielectric permittivity (ε), electric conductivity (σ) and magnetic permeability (μ) are the three fundamental variables that govern wave propagation. Electromagnetic contrasts originating from soil interfaces create partial wave reflections that are detected by the system. The three variables are described as follows:

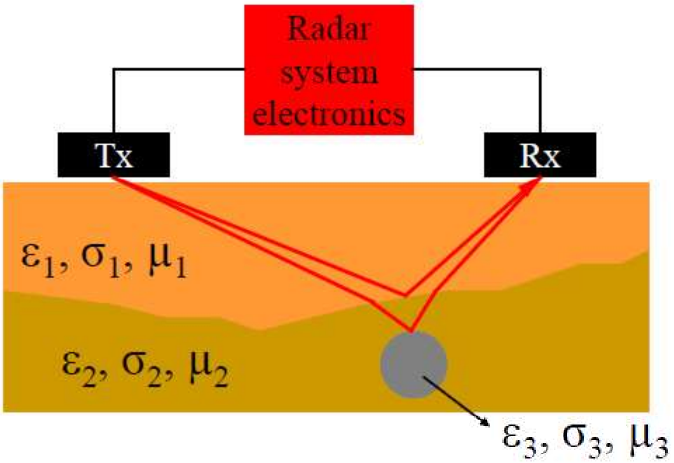

Figure 2.1: GPR consists of an emitting antenna (Tx), a receiving antenna (Rx) and an electronic system. EM energy is transmitted down into the ground and reflected by EM interfaces. ε_i, σ_i and μ_i are EM properties of materials (Lambot, 2018).

(i) Dielectric permittivity ε (F/m) characterizes the degree of electrical polarization a material experiences under the influence of an external electric field. It is defined as the ratio between the electric field ($\overrightarrow{E}$) within a material and the corresponding electric displacement ($\overrightarrow{D}$): $\overrightarrow{D} = \varepsilon.\overrightarrow{E}$. The dielectric properties of materials are generally expressed using the relative permittivity ε_r ($\varepsilon_r = \varepsilon/\ \varepsilon_0$ with ε the permittivity of the material and ε_0 the permittivity of free space). (ii) Electric conductivity σ (S/m) describes the ability of a material to pass free electrical charges under the influence of an applied field (Jol, 2010). Finally, (iii) magnetic permeability μ (H/m) is a measure of the ability of a substance to sustain a magnetic field.

Figure 2.2 shows how a recorded GPR signal is represented on a radar image. $A1$, $A2$ and $A3$ are three reflected waves coming from three electromagnetic interfaces (surface, base and subgrade reflections). The y-axis on the central image represents the wave propagation time (t), which corresponds to a wave round-trip from the electronic system. Each wave reflection is characterized by a more or less high variation in signal amplitude (which varies between -1 and +1). The propagation time is influenced by the depth of the interface and by the electromagnetic properties of the crossed medium (i.e., relative dielectric permittivity, ε_r).

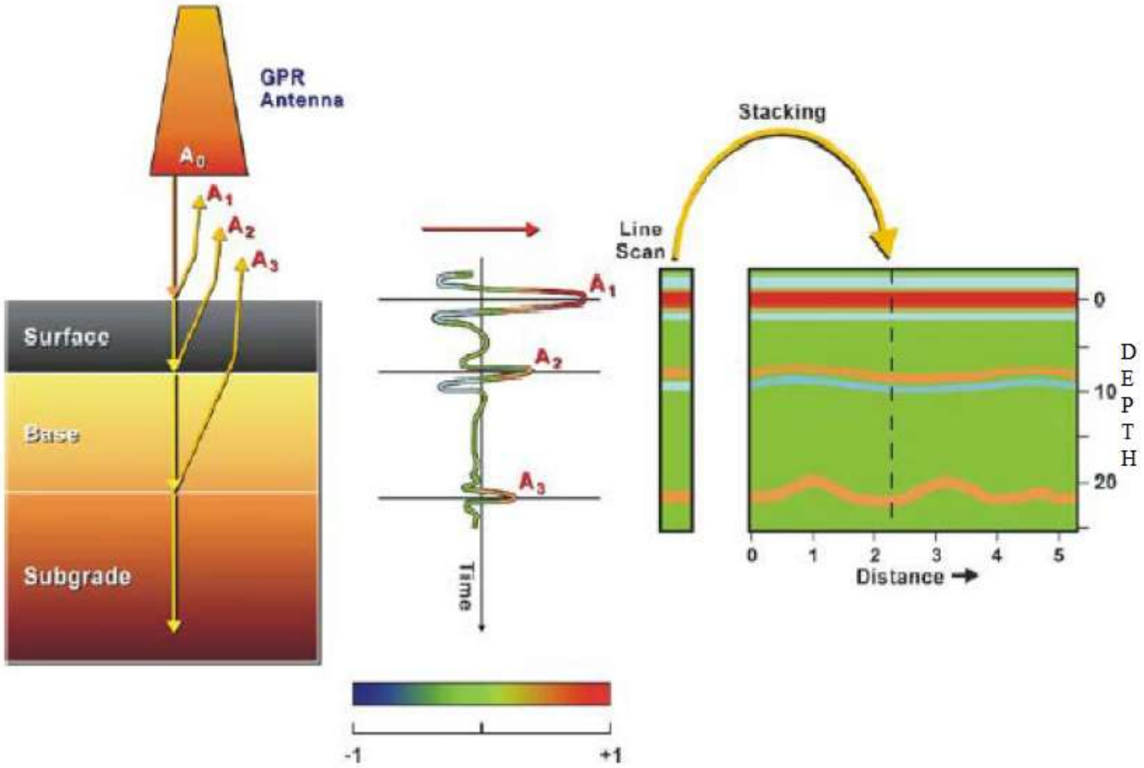

Figure 2.2: Subsurface imaging using a GPR. $A1$, $A2$ and $A3$ are three reflected waves coming from three EM interfaces (Lambot, 2018).

Knowing ε_r, propagation time (t) is converted into depth (z) as represented on the y-axis on the right image by applying Equation (2.1):

$$z = \frac{t}{2}.\nu \tag{2.1}$$

with z the depth [m], t the wave propagation time [s] and ν the wave propagation speed [m/s] approximated by the following equation:

$$\nu \approx \frac{c}{\sqrt{\varepsilon_r}} \tag{2.2}$$

with ν the wave propagation speed [m/s], c the wave speed in free space ($c = 3.10^8$ m/s) and ε_r the relative dielectric permittivity [-].

Finally, each individual GPR waveform is stacked along the defined transect and forms the final radar image. The x-axis of the radar image hence describes the distance of the recorded GPR data along the transect.

2.1.2 Time and frequency domain GPR systems

Time domain GPR (or impulse GPR) are the most commonly used GPR and are prevalent on the commercial market. A time domain pulse is transmitted and the reflected energy is received as a function of time. To have a good depth resolution, the time domain pulse duration must be as short as possible. In contrast, frequency domain GPR are continuous-wave systems in which the carrier frequency is changed either continuously or with a fixed step (Lambot, 2004). At each frequency, a continuous wave is transmitted. The amplitude and phase of the signal are then compared with the transmitted signal. The result is known as a "synthesized" pulse. Frequency data can be transformed in the time domain using the inverse Fourier transformation.

Figure 2.3 shows both block diagrams of time and frequency domain GPR systems. The radar system used in the field work of this study is a frequency domain GPR. It is described in Section 2.2.

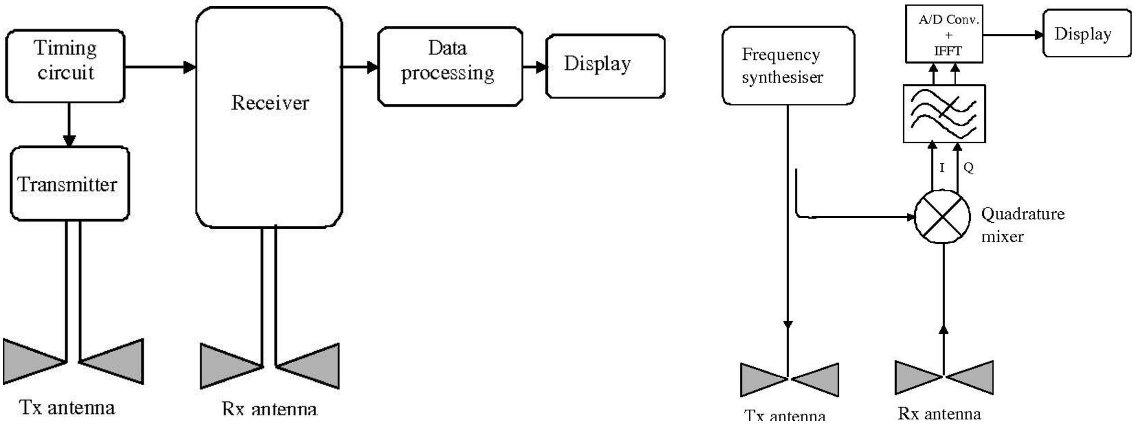

(a) (b)

Figure 2.3: Block diagrams of GPR systems. (a) Time domain GPR system. (b) Frequency domain GPR system (Daniels, 2004).

2.1.3 Propagation of electromagnetic waves in materials

Maxwell's equations

The foundations of GPR lie in electromagnetic principles. We must first remind that Maxwell's equations mathematically describe the physics of electromagnetic (EM) fields. They describe how electric and magnetic fields propagate, interact, and how they are influenced by objects. These equations are presented as follows in the frequency domain:

$$-\nabla \times \mathbf{H} + (\sigma + j\omega\varepsilon)\mathbf{E} = -\mathbf{J} \tag{2.3}$$

$$\nabla \times \mathbf{E} + j\omega\mu\mathbf{H} = -\mathbf{K} \tag{2.4}$$

where $\mathbf{H}$ is the magnetic field intensity [A/m], σ is the electric conductivity [S/m], ω is the angular frequency ($\omega = 2\pi f$ with f the frequency in Hertz), ε is the dielectric permittivity [F/m], $\mathbf{E}$ is the electric field intensity [V/m], $\mathbf{J}$ is the electric current density [A/m^2] and μ is the magnetic permeability [H/m].

Electromagnetic properties of materials

In most GPR applications, variations in the electric conductivity σ and dielectric permittivity ε are most influential while variations in the magnetic permeability μ are rarely of concern (Jol, 2010).

GPR is more commonly used in low-electrical-loss materials. In fact, the lower the electrical conductivity, the deeper the wave propagation. Earth materials are seldom composed of a single component (apart from water and ice) but are composites of different kinds of materials. For example, a sandy soil is essentially composed of soil grains but it is also made up of water, air and dissolved ions. This mixture will have electrical properties that are mostly proportional to the volume fraction of each of its components. In this way, the physical properties of soil mixtures must be taken into account in the interpretation of the GPR signal (Jol, 2010).

Although this topic is complex, the presence or absence of water in the material is the principal factor determining the soil electrical conductivity (σ) and dielectric permittivity (ε). The other soil variables that affect the electromagnetic properties are soil texture (mainly clay content), structure, soluble salts, temperature and density.

Propagation speed and attenuation of electromagnetic waves

Velocity (ν) and attenuation (α) are both important wave field properties (Jol, 2010). The propagation constant (γ) of electromagnetic waves depends on the dielectric permittivity (ε), the electrical conductivity (σ) and the magnetic permeability (μ) and it is expressed as follows (Minet, 2010):

$$\gamma(\omega) = \sqrt{-\omega^2\mu(\varepsilon - \frac{j\sigma}{\omega})} \tag{2.5}$$

with ω the angular frequency ($\omega = 2\pi f$ with f the frequency in Hertz).
The propagation constant can be expressed as a complex number:

$$\gamma = \alpha + j\beta \tag{2.6}$$

where the real part α is called the attenuation constant (Equation (2.7)) and the imaginary part β is the phase constant (Equation (2.8)).

$$\alpha = \sqrt{\frac{\omega^2\mu\varepsilon}{2}(\sqrt{1+\tan^2\delta} - 1)} \tag{2.7}$$

$$\beta = \sqrt{\frac{\omega^2\mu\varepsilon}{2}(\sqrt{1+\tan^2\delta} + 1)} \tag{2.8}$$

where

$$\tan\delta = \frac{\sigma}{\omega\varepsilon} \tag{2.9}$$

Wave attenuation is an important factor for GPR applications. It determines the possible investigation depths according to the frequency range and the electromagnetic properties of the materials which are probed. Therefore, the attenuation of electromagnetic waves can be described with Equation (2.7); it defines the rate with which the EM waves are attenuated as they propagate throughout a material. According to this relation, if the frequency is high as well as the electrical conductivity, the waves will be rapidly attenuated.

The imaginary part β (Equation (2.8)) is called the phase constant and it determines the wave propagation speed (ν):

$$\nu = \frac{\omega}{\beta} = \frac{1}{\sqrt{(\mu\varepsilon/2)(\sqrt{1+\tan^2\delta} + 1)}} \tag{2.10}$$

The wave propagation speed is commonly approximated by the following equation:

$$\nu \approx \frac{1}{\sqrt{\mu\varepsilon}} = \frac{c}{\sqrt{\varepsilon_r}} \tag{2.11}$$

where ν is the wave propagation speed [m/s], c is the wave speed in free space ($c = 3.10^8$ m/s) and ε_r is the relative dielectric permittivity [-]. The wave propagation velocity is in this case, only dependent on the ε_r of the material. This relation is mostly used with materials that have a relatively low σ and considering high frequencies. It is applicable for most soils prevalent in the environment (Minet, 2010).

2.1.4 Lambot *et al.* methodology

In order to understand the functioning of the radar system, it is necessary to briefly describe the Lambot *et al.* methodology. This methodology proposes an integrated approach that can enable real-time mapping of the soil electric properties using GPR (Lambot, 2004). The GPR system described in this methodology consists of an ultrawideband (UWB) stepped-frequency continuous-wave (SFCW) radar associated with an off-ground transverse electromagnetic (TEM) horn antenna.

Forward modeling of the GPR signal and radar equation

The GPR signal consists of a frequency-dependent complex ratio $S11(\omega)$, between the returned signal ($Y(\omega)$) and the emitted signal ($X(\omega)$), ω being the angular frequency (Lambot, 2004).

$$S11(\omega) = \frac{Y(\omega)}{X(\omega)} \tag{2.12}$$

$S11(\omega)$ is measured at the connection between the antenna feed point and the vector network analyzer[1](VNA) cable. The antenna can be modeled as a simple linear system composed of elementary model components in series and parallel. These components are illustrated in the block diagram shown in Figure 2.4.

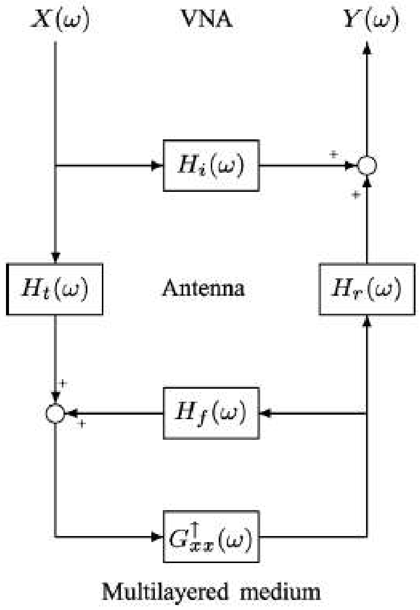

Figure 2.4: Block diagram representing the VNA-antenna-multilayered medium system modeled as linear components in series and parallel (Lambot, 2004).

---

[1] network analyzer that measures both amplitude and phase properties.

In this block diagram, $G_{xx}^{\uparrow}(\omega)$ is the Green's function describing 3-D wave propagation in the air-subsurface system modeled as a multilayered medium (see below). $H_i(\omega)$ represents the complex return loss transfer function of the antenna. It represents the part of the various reflections that occur between the antenna feed point and the antenna aperture due to its inner variations of impedance. It can be measured by performing $S11(\omega)$ measurements in free space (where $G_{xx}^{\uparrow} = 0$). $H_t(\omega)$ and $H_r(\omega)$ are the transmitting and receiving transfer functions. They describe the antenna gain respectively the phase delay between the measurement point and the source/receiver virtual point. $H_t(\omega)$ and $H_r(\omega)$ can be combined in the following equation : $H(\omega) = H_t(\omega)H_r(\omega)$. Finally, $H_f(\omega)$ is the feedback loss transfer function of the antenna.

Therefore, all of these components are included in the resulting radar equation, expressed in the frequency domain as:

$$S11(\omega) = \frac{Y(\omega)}{X(\omega)} = H_i(\omega) + \frac{H_t(\omega).G_{xx}^{\uparrow}(\omega).H_r(\omega)}{1 - H_f(\omega).G_{xx}^{\uparrow}(\omega)} \tag{2.13}$$

In this antenna equation, $S11(\omega)$ is the quantity measured by the GPR. To calculate the response of the soil $G_{xx}^{\uparrow}(\omega)$ from the raw radar measurements, we must first characterize the three unknowns ($H_i(\omega)$, $H(\omega)$ and $H_f(\omega)$). The three transfer functions $H_i(\omega)$, $H(\omega)$ and $H_f(\omega)$ can be determined by solving a system of three equations as pertaining to three different model configurations, to three unknowns (Lambot, 2004). In order to solve this system, we must carry out measurements at different heights above a copper sheet for which we know the response $G_{xx}^{\uparrow}(\omega)$. The EM waves will be totally reflected on this copper sheet. Moreover, the propagation of the waves in air is also controlled and we can precisely measure the distances between the antenna and the copper sheet. The model consists of simulating the medium response using a Green's function for different antenna heights. In this way, $S11(\omega)$ and $G_{xx}^{\uparrow}(\omega)$ are known for a series of configurations. These equations will enable to determine the characteristic antenna transfer functions.

Wave behavior with electromagnetic interfaces

As explained above, the model is based on linear system transfer functions and on the exact solution of the 3-D Maxwell's equations (Section 2.1.3) for wave propagation in a horizontally multilayered medium representing the subsurface (Lambot, 2004). This air-subsurface system is modeled as a 3-D multilayered medium consisting of N-horizontal layers separated by N-1 interfaces. This is illustrated in Figure 2.5.

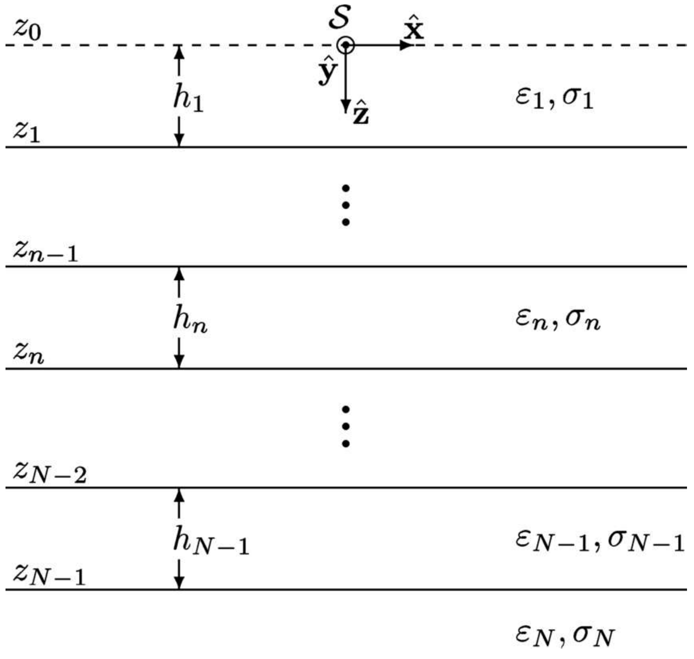

Figure 2.5: Model configuration as a 3-D multilayered medium characterized by ε_n, σ_n and h_n. S is the source and receiver point (Lambot, 2004).

Each layer is characterized by a dielectric permittivity (ε_n), electric conductivity (σ_n) and thickness (h_n) ($\mu = \mu_0$). S represents the source and receiver point, and is located at the origin of the coordinate system. The emitting part of the TEM antenna is approximated by an infinitesimal horizontal x-directed electric dipole (2^{nd} subscript x in $G^{\uparrow}_{x\underline{x}}$) whereas the receiving part of the antenna is emulated by recording the horizontal x-directed component (1^{st} subscript x in $G^{\uparrow}_{\underline{x}x}$) of the backscattered electric field (arrow in $G^{\uparrow}_{xx}$). The spatial domain Green's function at the source point S ((x,y,z) = 0) is obtained from the spectral domain Green's function as $\tilde{G}^{\uparrow}_{xx}$ (Equation (2.14)) in view of the monostatic mode (Lambot, 2004):

$$G^{\uparrow}_{xx} = \frac{1}{8\pi} \int_0^{+\infty} \tilde{G}_{xx}(k_\rho) k_\rho d k_\rho \tag{2.14}$$

where k_ρ is a spectral domain parameter.

Filtering of the antenna effects

It is important to define the transfer functions because they represent the antenna effects on the measured signal. Subsequently, the antenna effects are filtered out from the signal $S11(\omega)$ to have a direct access to the medium response $G^{\uparrow}_{xx}$. The following equation (Equation (2.15)) describes this process:

$$G^{\uparrow}_{xx}(\omega) = \frac{-S11(\omega) + H_i(\omega)}{H_i(\omega).H_f(\omega) - S11(\omega).H_f(\omega) - H_t(\omega).H_r(\omega)} \tag{2.15}$$

The filtering of the antenna effects plays an important role in the analysis of the radar image. It improves the vertical resolution of the radar image and allows to resort to full-wave inverse modeling to have access to more information on the medium of interest. This is illustrated in the next section on the antenna calibration (Section 2.2.1).

Model inversion

In order to identify subsurface parameters, inverse modeling is applied. This method, also developed by Lambot *et al.* is a nonlinear optimization method which consists of finding a parameter vector $\mathbf{b}$, $\mathbf{b} = [\varepsilon_r, h]$, so that an objective function $\phi(\mathbf{b})$ is minimized (Lambot, 2014). This inverse method is developed in the least squares sense. ε_r is the relative dielectric permittivity [-] and h is the distance between the medium and the antenna phase center [m]. The objective function $\phi(\mathbf{b})$ is described by the following equation:

$$\phi(\mathbf{b}) = |G^{\uparrow}_{xx}{}^{*} - G^{\uparrow}_{xx}|^T C^{-1} |G^{\uparrow}_{xx}{}^{*} - G^{\uparrow}_{xx}| \tag{2.16}$$

where $G^{\uparrow}_{xx}{}^{*} = G^{\uparrow}_{xx}{}^{*}(\omega)$ contains the observed response function whereas $G^{\uparrow}_{xx} = G^{\uparrow}_{xx}(\omega, \mathbf{b})$ contains the simulated response function (Lambot, 2004). The global reflection coefficients contained in these functions are complex vectors, therefore the objective function $\phi(\mathbf{b})$ is defined by the amplitude of the errors in the complex plane (Lambot, 2014). Because this function is characterized by an oscillatory behavior with many local minima and moreover is a nonlinear function, we must use a global optimization algorithm to minimize the function. The Lambot *et al.* methodology uses the global multilevel coordinate search algorithm or GMCS (Huyer and Neumaier, 1999) combined with the Nelder-Mead simplex algorithm or NMS (Lagarias *et al.*, 1998).

Soil moisture sensing by GPR

Soil moisture sensing relies on the electromagnetic properties of the subsurface which are the relative dielectric permittivity (ε_r) and the electrical conductivity (σ) (Minet, 2012). These properties govern the propagation of the electromagnetic waves. The dielectric permittivity of water is much higher than the one of soil particles, therefore, GPR is essentially sensitive to soil moisture ($\varepsilon_{r,water} = 80$, $\varepsilon_{r,soil} \approx 5$). The surface soil moisture is estimated using the inversion method described above which focuses on the surface reflections. Two parameters will be optimized: the dielectric permittivity and the GPR antenna height.

Now that GPR principles and its methodologies are understood, we can describe the two different radar systems (frequency and time domain) that were used for the purpose of this study.

2.2 Frequency domain radar system setup

This section describes the setup of the specific frequency domain radar system used during our field work. The first subsection describes the antenna calibration, then, the different numerical simulations that were carried out are explained. Finally, laboratory tests are presented. Results are exposed in Chapter 4.

2.2.1 Antenna calibration

Objective

As explained previously, to filter out the antenna effects, we must proceed to antenna calibration.

Materials and methods

The ground-penetrating radar system consists of a handheld vector network analyzer (VNA, Planar R54, Copper Mountain Technologies, Indianapolis, USA) that uses a stepped-frequency continuous-wave system. The VNA is capable of measuring the reflection coefficient $S11$ from 85 MHz to 5.4 GHz. Its program is launched from a remote computer or smart phone connected to the computer through a local Wi-Fi network.

The radar also consists of a horn dipole antenna made of copper. It is used simultaneously as transmitter and receiver (monostatic mode). Its dimensions are 65 cm long and it weighs about 1 kg. It was designed at the Georadar Research Centre (UCL) to adapt its frequency range to the requirements of the project (i.e., low frequencies). Its design is based on a aluminum antenna that was built last year by another student as part of his Master thesis. The radar system is illustrated below in Figure 2.6.

To calibrate the antenna, we used the far-field model developed by Lambot *et al.* (2004, 2014). This model was described in the previous section (Section 2.1.4). The antenna calibration was done in two steps. The first calibration was done without the handle and was necessary to filter out the antenna effects for the laboratory tests (Section 2.2.2) and for the numerical simulations (Section 2.2.3). The second calibration was done with the handle and was used for the field measurements. Indeed, the presence of the handle is expected to change the antenna properties.

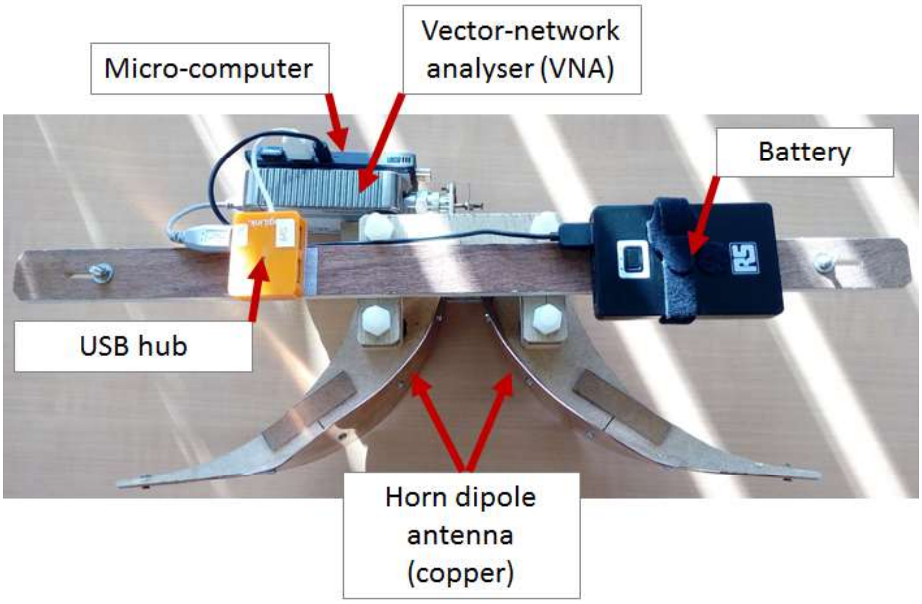

Figure 2.6: Radar system composed of a horn dipole antenna, a VNA, a micro-computer, a USB-hub and a battery.

We performed the measurements on top of a copper sheet (known electromagnetic properties) at seven different heights (60 cm, 65 cm, 70 cm, 75 cm, 80 cm, 85 cm and 90 cm). For each height, 10 to 15 measurements were recorded by the radar. Note that we used the far-field model for both calibrations.

2.2.2 Laboratory tests

Objective

To test the ground penetrating radar and more specifically the horn dipole antenna, a laboratory test was carried out on a perfectly dried sand. This test took place in the Georadar Research Centre (UCL). The measurements were taken over a sandbox (dimensions: 3 x 3 x 1 m) which contained a homogeneous dry sand. The sand layer was about 80 cm deep and lied on top of a copper sheet that acted as a perfect electrical conductor in order to avoid unidentified reflections from lower materials. When we performed this series of tests, a water-filled leaking PVC pipe was buried in the sand.

The objective of this test was to confirm the proper functioning of the radar system, to see until which depth waves penetrate the sand and to define at what level we can filter out antenna effects, i.e., define the minimum height of the radar system over the sand surface. We were also able to compare radar images with or without antenna filtering.

Materials and methods

We performed a transect of 2 m long perpendicular to the PVC pipe with the antenna positioned at different heights above the dry sand (1.5 cm, 10 cm, 20 cm, 30 cm and 40 cm). The GPR was fixed on an automated positioning arm. A *Matlab* script controlled the position of the radar and moved it along the transect. The radar recorded about 40 measurements along the transect for the five different heights. This corresponds to 1 measurement every 5 cm. The following figure (Fig. 2.7) shows the radar system fixed on the automated arm on top of the sandbox.

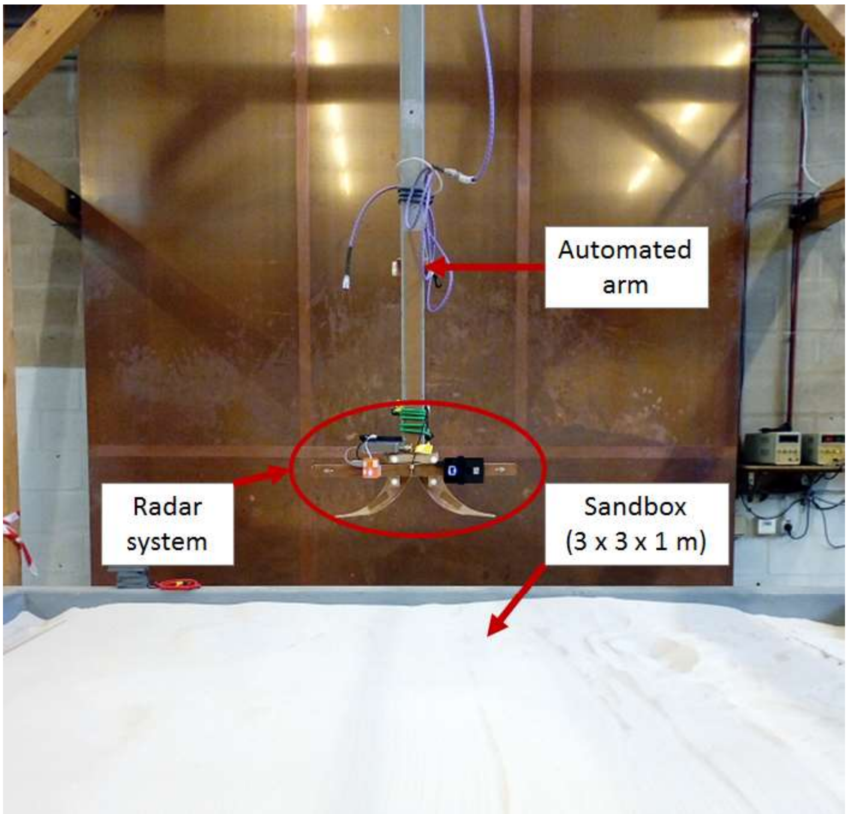

Figure 2.7: Radar system on top of the sandbox of dimensions 3 x 3 x 1 m composed of perfectly dry sand. A water leaking pipe and a copper sheet are buried.

2.2.3 Numerical simulations

Objective

To ensure the proper functioning of the ground penetrating radar in similar conditions to those expected in the Maâmora forest, numerical simulations were performed thanks to another *Matlab* script. In addition, these simulations provided more information on the maximum sandy soil depths where the GPR is effective.

Materials and methods

A *Matlab* script computed the radar data in the frequency domain using the far-field antenna model developed by Lambot *et al.* (2004) which was previously explained. Three-dimensional Green functions were used to describe the wave propagation in a planar layered media.

Radar simulations were conducted assuming a perfect electrical conductor buried at an increasing depth, ranging from 0.5 m to 10 m with a step of 0.1 m. We also assumed three different values for the antenna height above the ground, namely, 0.1 m, 0.2 m and 0.3 m. The medium properties were chosen to be representative of the sand in the Maâmora forest. The magnetic permeability was fixed to 1 H/m while the values of relative dielectric permittivity ranged between 2 and 8 and the values of the electrical conductivity ranged between 1.10^{-4} S/m and 10.10^{-3} S/m.

2.2.4 Field tests

Objective

Before traveling to Morocco, it was necessary to test this prototype ground-penetrating radar in the field. Our first idea was to go to the Belgian coast and test the GPR in comparable conditions, on dry sandy beaches. Unfortunately, antenna calibration took more time than anticipated and rainy weather in December prevented us from finding dry sands. We considered it was not valuable to perform GPR measurements on humid sands. However, we tested the GPR system on a parking lot near the laboratory in order to ensure that the whole system worked correctly.

Materials and methods

We added the handle and a GPS to our radar system in order to have georeferenced data. The GPS data is linked to the GPR data by interpolation. The measurements took place in a parking lot. Therefore, the radar data was collected on top of a bitumen surface. The transect defined was about 30 m long and the data was acquired at a mean velocity of about 4 km/h. An additional test was carried out on the exterior wall of a building. The GPR was held perpendicularly to the wall, the antenna facing the wall. Data was collected along a transect of about 20 meters.

2.3 Time domain radar system

Data gathered by a second radar system in December 2015 was also used in this study. This radar is a low-frequency time domain commercial GPR (SIR-20, GSSI). The antenna of this radar system has a central frequency of 400 MHz. It operates in the time domain and records measurements with a high spatial resolution (1 measurement every 2 cm). A GSSI positioning wheel was used with the radar system.

Chapter 3

Material and methods: Field measurements and data processing

In January 2018, I traveled to Rabat-Salé (Morocco) for a one-month residence at the National School of Forestry Engineers of Salé (ENFI). During my stay, I carried out the entirety of the field measurements necessary for this study. After a brief description of the study area, this present chapter specifies the different measurements that were carried out and the protocols that were followed. Then, it summarizes the data processing.

3.1 Study area

The study area is located in B canton, between plots VI-6 and VI-7 (see Fig. 1.1). It is delimited by the 14 radar transects that were performed (see Section 3.2). With a South-West to North-East orientation, it is about 700 m long and 150 m wide and covers an area of 1.05 ha. The plot is covered by cork oaks of 18 years of age. This plot was chosen for a few reasons. First of all, it has a high variability in terms of survival rates, circumferences and heights. This can be observed on the satellite image shown in Figure 3.1 and on the pictures of the study plot which are shown in Appendix 2. The nearby areas also show survival rate issues. Moreover, previous studies of this particular plot have shown that there is variability in the sand and clay layer depths (Himpens, 2016). Finally, this forest plot is near a paved road which makes it easily accessible by car.

Plot B-VI-6 was artificially regenerated in 1999 with acorn seedlings. The plot was cleaned and ploughed deeply before planting. Four acorns were planted in cubic holes of 20-30 cm deep and then were refilled with soil. During the first year, the plantation was watered twice (10 l/seedling). Until the third year, weeding and harrowing took place, then, in 2007, individualization occurred to select one tree per seedling. Finally, pruning and thinning took place in 2014.

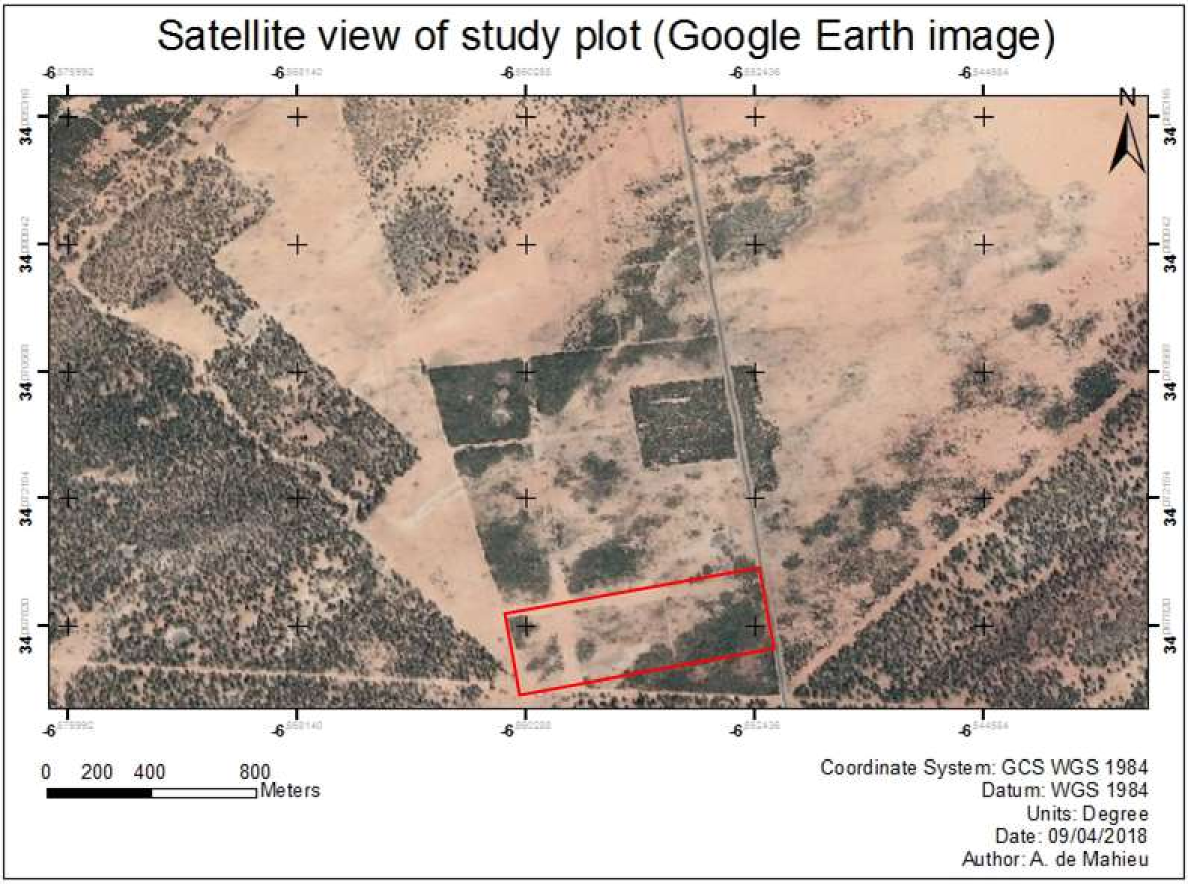

Figure 3.1: Google Earth view (2017) of cork oak plots and main road. Study plot is shown in the red frame.

3.2 GPR data

To cover a significant portion of the forest plot, we gathered 14 GPR transects. Each transect is composed of about 2500 measurements and positioned by interpolation with geographical coordinates. The transects are located between two rows of trees and two transects are separated by three rows of trees (distance of about 9 m between each transect). Therefore, 42 rows of cork oak trees were covered by the radar measurements. Unfortunately the antenna calibration that took place in Belgium was not applicable in Morocco. We assume this is due to the fact that the VNA was disconnected from the antenna during the plane trip. Without access to a perfect electrical conductor (such as a large copper plate) to carry out a new calibration *in situ*, we executed a calibration on top of a daya that was located near our forest plot. This calibration enabled us to filter out antenna effects during post-processing of the raw data. In addition to these radar transects, free-space measurements were taken before each transect to correct the H_i specific of each radar transect.

The radar images were immediately analyzed after the survey in order to provide key information for defining the soil coring locations as well as the dendrometric research plots. In particular, a preliminary map of the variation in signal amplitude for all 14 transects was drawn (available in Appendix A.3). Figure 3.2 shows the 14 GPR transects (red and blue) of the forest plot.

3.3 Dendrometric data

With the help of the preliminary GPR signal map presented above and the satellite image of the study area (i.e., vigor of trees), 36 dendrometric research plots were defined. They are crossed by six out of fourteen GPR transects that were selected based on observations (red coloured transects in Figure 3.2). Research plots are rectangles 12 m wide and 24 m long covering a total area of 288 m^2. 32 tree locations (4 x 8) are included in each plot. Their location is depicted in Figure 3.2.

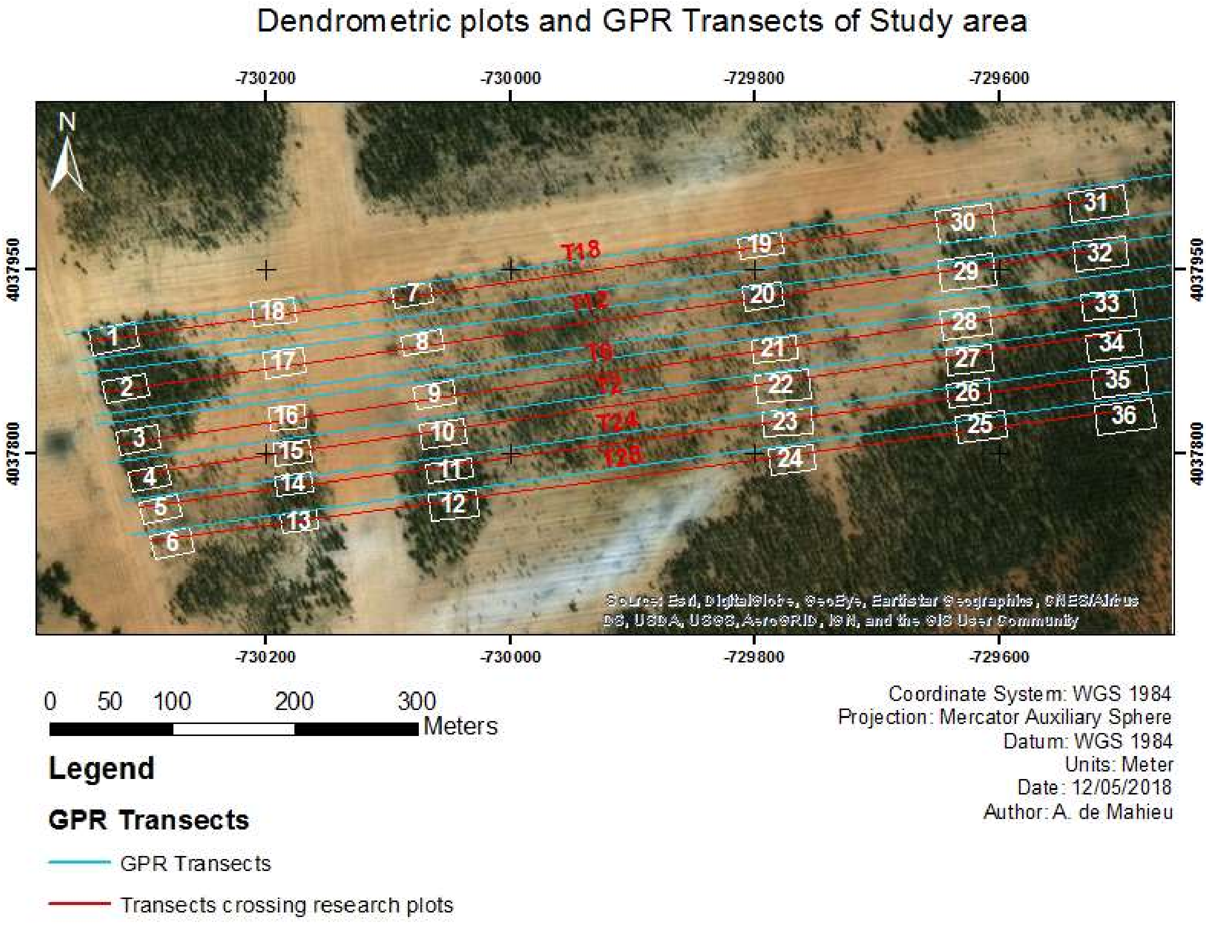

Figure 3.2: Geographical location of the 36 dendrometric plots and GPR transects. Dendrometric plots are crossed by the six red GPR transects (T2, T6, T12, T18, T24 and T28).

The research plots were referenced by four markers on each corner and GPS coordinates were measured with a handheld *Trimble Juno 3D* GPS system. Within each plot, survival rate, circumference and height were measured.

To calculate survival rate (S_r), the number of living and dead trees (N_{living} N_{dead}), tree stumps (N_{stumps}) and empty locations (N_{empty}) were counted. Equations (3.1) and (3.2) provide relevant calculations:

$$N_{pot} = N_{living} + N_{dead} + N_{stumps} + N_{empty} \tag{3.1}$$

$$S_r = \frac{N_{living}}{N_{pot}} \tag{3.2}$$

with N_{pot} the potential number of trees on a dendrometric plot, N_{living} the number of living trees, N_{dead} the number of dead trees, N_{stumps} the number of tree stumps, N_{empty} the number of empty locations (based on the initial distance separating two seedlings) and S_r the survival rate [%].

Trunk circumference (C) was measured at a height of 1.30 m with a measuring tape. Mean circumference was then calculated for each plot using the following equation:

$$C_{mean} = \frac{\sum\limits_{i=1}^{n} C_i}{n} \tag{3.3}$$

where C_{mean} is the mean circumference per plot [cm], C is the circumference of a tree [cm] and n is the number of living trees per plot.

Finally, tree height (H) was measured using a *VERTEX III*, composed of a dendrometer and a transponder. The transponder is fixed on the tree trunk at a height of 1.30 m (TRP Height). The dendrometer measures the distance between the transponder and the receptor (on the dendrometer) and the angle to the tree top. The device then estimates the tree height using trigonometric principles (Pauwels, 2001). Mean height was then calculated for each plot as:

$$H_{mean} = \frac{\sum\limits_{i=1}^{n} H_i}{n} \tag{3.4}$$

where H_{mean} is the mean height per plot [m], H is the height of a tree [m] and n is the number of living trees per plot.

Moreover, basal area (G) and dominant height (H_{dom}) were calculated. Basal area is an excellent measurement of forest density. It allows to compare density between forest plots, to verify the relation between the measured density and natural regeneration, to measure competition between species, ... (de Potter, 2011). It is generally measured in square meters per hectare [m^2/ha]. Tools like relascopic prisms or notched relascopes can be used to estimate basal area on the field but we calculated it using the measured circumferences (C). The basal area of a tree is equal to the area of its cross section at a height of 1.30 m. The basal area of a forest stand (or of a given group of trees) is equal to the sum of the individual basal areas of all trees in the forest stand (or group of trees) (Cordonnier *et al*, 2007). The cross section area of each tree (g_i) was estimated using:

$$g_i = \frac{C_i^2}{4\pi} \tag{3.5}$$

with g the cross section of a tree [m^2] and C the tree circumference at a height of 1.30 m [m].

For a forest plot of 288 m^2, the basal area of an individual forest plot (G_{plot}) equals to:

$$G_{plot} = \sum_{i=1}^{n} g_i \tag{3.6}$$

with G_{plot} the basal area of an individual plot [m^2] and g the cross section of a tree [m^2].

We can then calculate the basal area [m^2/ha] using:

$$G = \frac{G_{plot}}{288} * 10^4 \tag{3.7}$$

where G is the basal area [m^2/ha] and G_{plot} is the basal area [m^2].

The dominant height of a forest stand is the mean height of a determined number of trees among the highest or the largest (Rondeux, 1993). It varies more or less continuously in time and thus is a proper expression of the stand growth. It corresponds to the arithmetic mean height of the 100 largest trees per hectare. Hence, for each of our research plots, it can be calculated by applying a simple rule of three. In our case, it equals to the mean height of the three largest trees (in terms of circumference) of each research plot.

3.4 Soil data

Soil surveys were carried out systematically on each research plot crossing a GPR transect using a soil auger of 2 m long. Geographical coordinates of each survey were taken using the same *Trimble Juno 3D* GPS in order to associate them with the GPR data. Soil cores of 20 cm or 40 cm long were extracted from the ground and laid down in order to reassemble the soil horizons. Pictures were taken, observations were made and 3 to 6 samples from different horizons of each profile were collected for further analyses.

3.4.1 Soil water content

First, soil water content of three horizons for every profile was estimated by weighing approximately 100 grams of fresh soil (m_{fresh}), then drying it for 24h in a vacuum oven at 105°C and weighing the dried soil (m_{dry}). The gravimetric water content (θ_m) equals to:

$$\theta_m = \frac{(m_{fresh} - m_{dry})}{m_{dry}} \tag{3.8}$$

with θ_m the gravimetric water content [-], m_{fresh} the mass of fresh soil [g] and m_{dry} the mass of dry soil [g].

3.4.2 Soil texture

Soil texture was first estimated for all 36 depth soil samples using the "hand-touch sensation method" (Hassan, 1988). The protocol is available in Appendix A.4. It consists of kneading a small quantity of soil into a thin ribbon. The operator must be able to form a ribbon of at least 5 cm long to characterize the sample as a clayey horizon. According to the touch of the sample, soil texture can hence be predicted.

To determine more precisely soil sample texture, sieve analyses were performed. The percentage of each constituent (clay, silt and sand) was therefore determined. Then soil texture can be defined using the soil texture diagram (or triangle). This diagram shows how the 12 referenced textures are classified based on the percentages of sand, silt and clay. It is illustrated in Figure 3.3.

Sieve analyses were performed in two phases. First, 39 granulometric (3 x 13 profiles) analyses were performed at the National Institute of Agricultural Research of Rabat (INRA). Because I had limited time on site, 3 additional profiles (16 samples) were brought back to Belgium to carry out additional analyses.

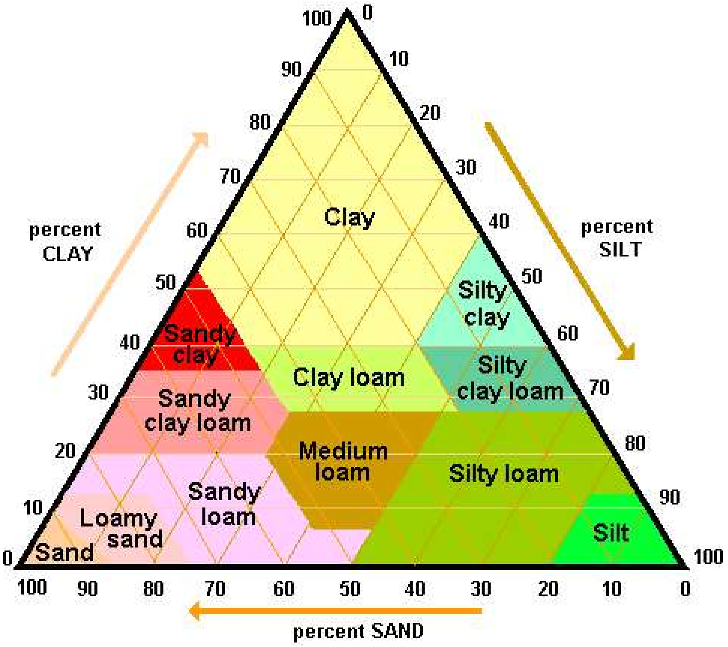

Figure 3.3: Classification of the 12 reference soil textures using the soil texture diagram (USDA, 1987).

In Morocco, three samples per profile were chosen to carry out sieve analyses: the first soil surface sample (0-20 cm or 0-40 cm), a deeper soil sample and a third sample located in the middle of the soil profile. In Belgium, more samples per profile (up to 6) were analyzed to reconstruct a more complete textural profile.

At INRA laboratory, the densimeter method was applied. The first step of the operating method is dispersion. It consists of first attacking organic matter, then attacking limestone and finally eliminating the adsorbing cations of the soil samples. The organic matter attack was carried out for only 4 out of 13 surface horizon samples which had higher proportions of organic matter. 40 ml of oxygenated water (H_2O_2, 30%) were added to 20 g of soil mixed with 100 ml of distilled water. The solutions were then placed on a hot-plate taking care not to bring the solutions to a boil. H_2O_2 was added until the reaction ended (the supernatant was clear). The second step was not applied because Maâmora is not characterized by calcareous soils. Finally, the third step consisted of filtering the soil solutions under vacuum. Because of missing equipment, this step was not feasible. Instead, we waited for the solutions to decant. To eliminate the exceeding salts, the supernatants were siphoned. Then, water was added and the process was repeated as long as decantation did occur within 1h.

The second step of the operating method is sedimentation. 12.5 ml of sodium pyrophosphate ($Na_4P_2O_7$) were added in each flask containing the remaining soil. After transferring the new solutions in 500 ml test tubes (Fig. 3.4), distilled water was added to obtain a total volume of 500 ml. The densimeter method consists of placing a densimeter in the thoroughly mixed soil solutions at t = 30 s, 1 min, 6 min, 12 min and 3 h. The indicated values by the densimeter are recorded. Then the solutions were sifted (0.05 mm) to separate sands from clay and silt constituents. These sands were weighed. Finally, calculations were performed to find the percentages of each constituent.

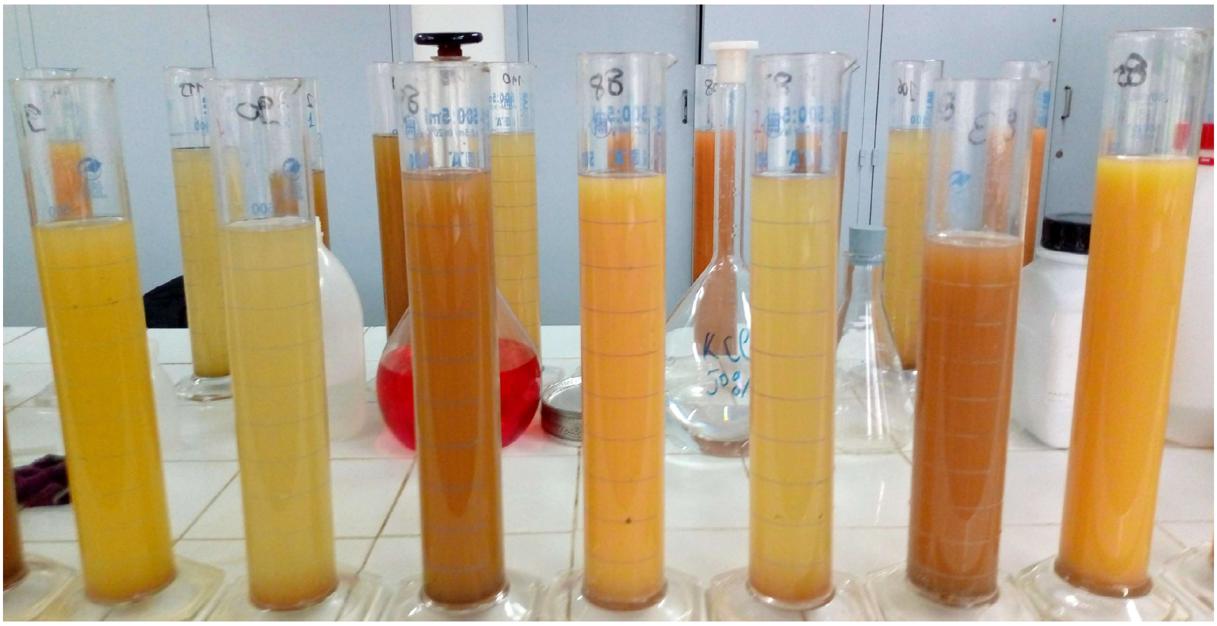

Figure 3.4: Test tubes containing soil solutions before sedimentation at INRA laboratory (Rabat, Morocco).

At the UCL soil laboratory, the pipette method was carried out to characterize soil texture. First organic matter attack was carried out on 5 samples by adding 20 ml of H_2O_2 (6%) to the soil solutions and by placing them on a hot-plate (40°C). Then, all soil solutions were placed under ultrasounds to separate clays and silts from sands. Ultrasounds break the links of silt and clay particles to the minerals in sands. The solutions were then sifted (0.05 mm) and the extracted sands were placed in a vacuum oven at 105°C for 24h. The remaining soil solutions were placed into 500 ml test tubes. 5 ml of hexametaphosphate (HMP) were added and the pH was adjusted to 8.5-9 by adding sodium carbonate (Na_2CO_3). Distilled water was then added to obtain a total volume of 500 ml.

After mixing thoroughly each test tube, 10 ml of each soil solution were pipetted at t = 0 s, 4 min 48 s and 24 h using a Robinson pipette. At t = 0 s, the solutions were pipetted in the middle of the test tube, at t = 4 min 48 s, they were pipetted at 10 cm from the top of the test tube and at t = 24 h, they were pipetted at 30 cm from the top.

All of these extracted solutions were placed as well in a vacuum oven at 105°C. After 24 h, the resulting constituents were weighed and calculations were then performed to find the percentages of the three constituents.

3.4.3 Further analyses

At INRA, total carbon content was measured using the *Walkley-Black* method for all 13 surface samples. The operating method is illustrated in Appendix A.5. By multiplying the total carbon content obtained by titration by 1.724, we can estimate the total organic matter content in all 13 surface samples.

At UCL, acidity (pH_{H_2O}) of all 16 samples was measured using a pH-meter. 5 g of soil were mixed with 25 ml of distilled water. The solutions were mixed every 20 min. After one hour, the pH was measured.

Table 3.1 sums up which soil analyses were carried out for all 36 soil profiles (1 per dendrometric plot). Mass water content (θ_m) was measured for a total of 108 soil samples (36 x 3), pH was measured for 17 samples, surface organic matter content was measured for 13 samples and, finally, texture was determined for 56 samples.

Table 3.1: Overview of soil analyses carried out for each dendrometric plot.

Soil analysis	Soil profile/dendrometric plot
θ_m [%]	1 - 36
pH [-]	2, 7, 11
OM [%]	1, 4, 9, 12, 14, 16 19, 22, 25, 26, 29, 32, 34
Texture	1, 2, 4, 7, 9, 11, 12, 14, 16 19, 22, 25, 26, 29, 32, 34

3.5 GPR data processing

3.5.1 Soil surface water content

Each GPR transect as presented in Section 3.2 was analyzed using a *Matlab* script. Unfortunately, the radar system did not work as planned. The initial idea was to map the clay layer depth of the forest plot. However, this clay layer was not observable on the radar images. This is probably due to the fact that the shallow soil was rather humid and the electromagnetic waves were attenuated in the top first 10 cm - 20 cm. As the clay layer is located at minimum 1.50 m, the waves were not able to penetrate as required.

To address this issue, post-processing of the radar data allowed us to map the relative dielectric permittivity. Using the inversion method explained in Chapter 2, the relative dielectric permittivity was first estimated for each GPR data acquisition point. Then, using the kriging method on *ArcGis* program, dielectric permittivity of neighboring points was estimated by interpolation.

Kriging is a geostatistical technique that produces a prediction surface and provides measures of certainty or accuracy of the predictions (ESRI, 2016). The method fits a mathematical function to a specified number of points to determine the output values for each location. Kriging proceeds in two steps. First, an exploratory statistical analysis of the data must be carried out, then variogram modeling must be executed. Variogram functions (circular, spherical, exponential, gaussian, ...) are created to estimate the dependence/spatial autocorrelation values that depend on the fitted model. It then predicts the unknown values. The choice of the model is important because it influences the prediction of the unknown values. Each model is designed to fit different types of phenomena (ESRI, 2016). For more information on this topic, please refer to the ESRI URL page ([20]) which thoroughly explains the method.

The ordinary kriging method was chosen and the searching neighborhood was specified (25 neighbors including at least 5 points). An exponential semi-variogram model was chosen with no anisotropy. More properties on the kriging method are available in Appendix A.8 (Fig. A.18). Then, using Topp's equation (Equation (3.9)) (Topp *et al*, 1980) which describes the relationship between soil moisture and relative dielectric permittivity, we were able to estimate the volumetric soil surface water content (θ_v).

$$\theta_v = -0.053 + 0.0293\varepsilon_r - 0.00055\varepsilon_r^2 + 0.0000043\varepsilon_r^3 \tag{3.9}$$

where θ_v is the volumetric soil water content [m^3/m^3] and ε_r is the relative dielectric permittivity [-]. Using the same kriging method previously described, the volumetric soil surface water content was mapped.

It is important to mention that the mean dielectric permittivity obtained using the inversion method (and thus the volumetric water content) only corresponds to the first 10 cm - 15 cm of the soil profile. The inversion method is based on the surface reflections of the electromagnetic waves of our radar system. The frequencies (f) selected to apply the inversion method range between 560 and 700 MHz (f_{mean} = 630 MHz). The corresponding wavelength (λ) equals to approximately 24 cm. This was calculated using the following equation:

$$\lambda = \frac{v}{f} = \frac{c}{\sqrt{\epsilon_r} f} = \frac{3.10^8}{\sqrt{4}.630.10^6} = 0.238 \tag{3.10}$$

with λ the wavelenght [m], v the wave speed in the ground [m/s], f the wave frequency [Hz], c the wave speed in free space ($c = 3.10^8$ m/s) and ε_r the mean dielectric permittivity [-]. Therefore we can estimate the characterization depth of permittivity to be equal to approximately 10 cm to 15 cm (half wavelength).

3.5.2 Depths of textural transitions

Additionally, GPR data acquired previously as part of a Master thesis were retrieved (Himpens, 2016). This data was recorded in December 2015 by Dr Frédéric André using a time domain GPR as described in Chapter 2. Unlike our radar system, this GPR was able to detect electromagnetic interfaces in depths. Two of his transects covered our study area. Their location is shown in Figure 3.5. Data acquisition was interrupted a few times on each transect due to problems during measurements. Therefore, each transect is composed of three to four radar images (each image consists of a portion of a transect).

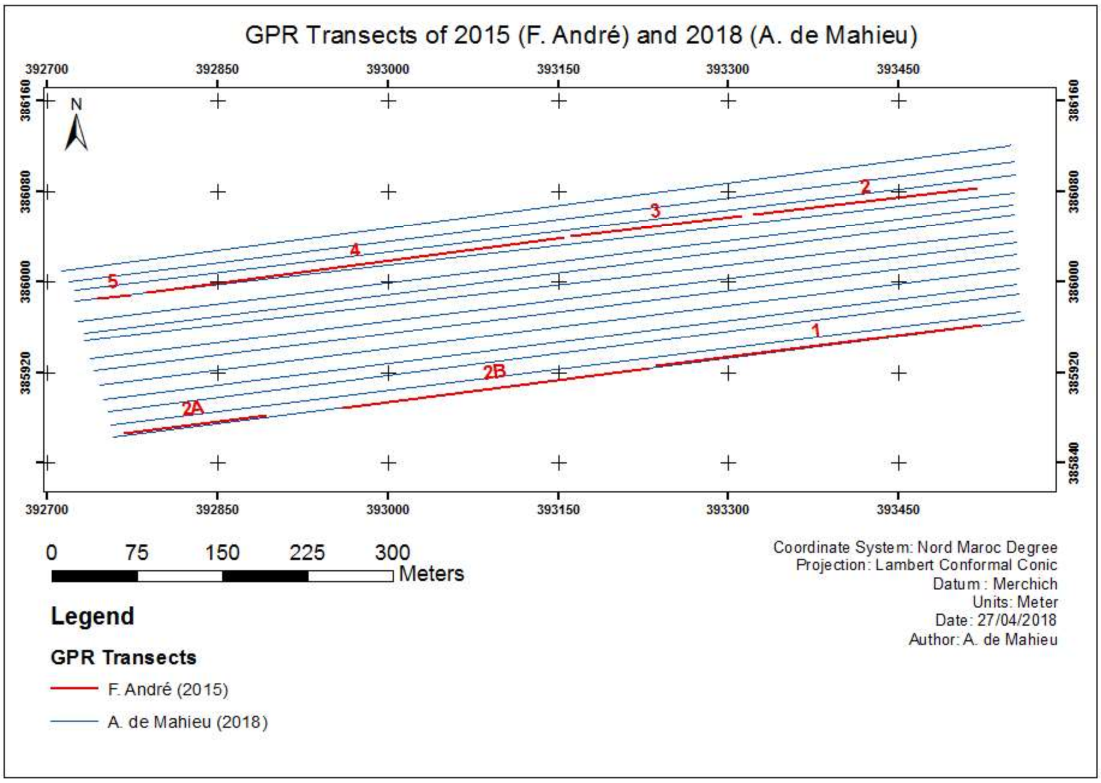

Figure 3.5: Position of the 2015 GPR transects (in red) in the study area among the 14 GPR transects of 2018 (in blue).

The GSSI positioning wheel was used for sub-transects 2A and 2B. For the other sub-transects, the wheel broke down and the measurements were carried out in "free run" (data was collected according to time instead of distance assuming a constant forward speed). The x-axis of these radar images must therefore be converted from time [s] into distance [m] using GPS coordinates at the beginning and ending points of each transect to determine its total length. Sub-transects 2A, 2B and 1 correspond to transect 28 of the GPR data acquired in January 2018 whereas sub-transects 2, 3, 4 and 5 fall between our transects 14 and 16.

To convert the wave propagation time (t) of the y-axis of the radar image into depth (z) as explained in Section 2.1.1, Equation (3.11) was applied :

$$z = \frac{t}{2} . \frac{c}{\sqrt{\varepsilon_r}} \tag{3.11}$$

where z is the depth [m], t the wave propagation time [s], $c = 3.10^8$ m/s and $\varepsilon_r = 5$ which defines a slightly humid sand ($\varepsilon_{r,drysand} \approx 3$). Note that the y-axis scale changes if the value of ε_r is changed in the script. The depth indicated by these images are therefore estimated depths. In addition, the first reflection which corresponds to the soil surface was positioned in $z = 0$ m (offset of 0.75 m).

Chapter 4

Results and discussion: GPR setup and relation between cork oak growth and soil properties

This chapter first presents the different GPR results derived from the frequency domain radar setup explained in Chapter 2. Then, field results obtained in Morocco are exposed: dendrometric results derived from tree measurements, GPR data originating from 2018 radar acquisition points and from radar images of 2015 and, finally, soil analyses results (field and laboratory). Lastly, an integration of the research results is presented and discussed.

4.1 Frequency domain radar system setup

4.1.1 Antenna calibration

The following figures (Fig. 4.1, 4.2 and 4.3) show the three transfer functions that result from the first antenna calibration of the frequency domain radar system (without the handle).

The antenna is considered efficient when H_i (Fig. 4.1) is lower than 0.5. As you can see on this graph, the frequencies where the antenna is efficient range from about 250 MHz up to 2800 MHz. Thus, this homemade antenna is efficient in low frequencies which are necessary to probe the more or less deep sand layers of the Maâmora forest (0.3 m - 6 m). A second calibration with the handle was also performed. The figures illustrating these three transfer functions can be found in Appendix A.6. The handle is made of fiberglass and should therefore not interfere with the antenna.

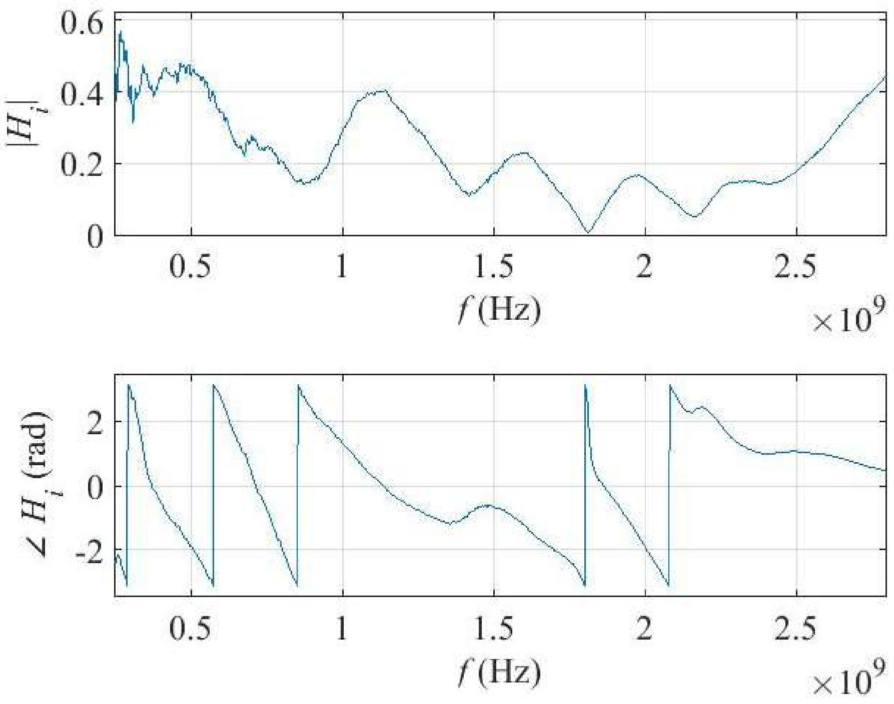

Figure 4.1: Complex return loss transfer function, H_i.

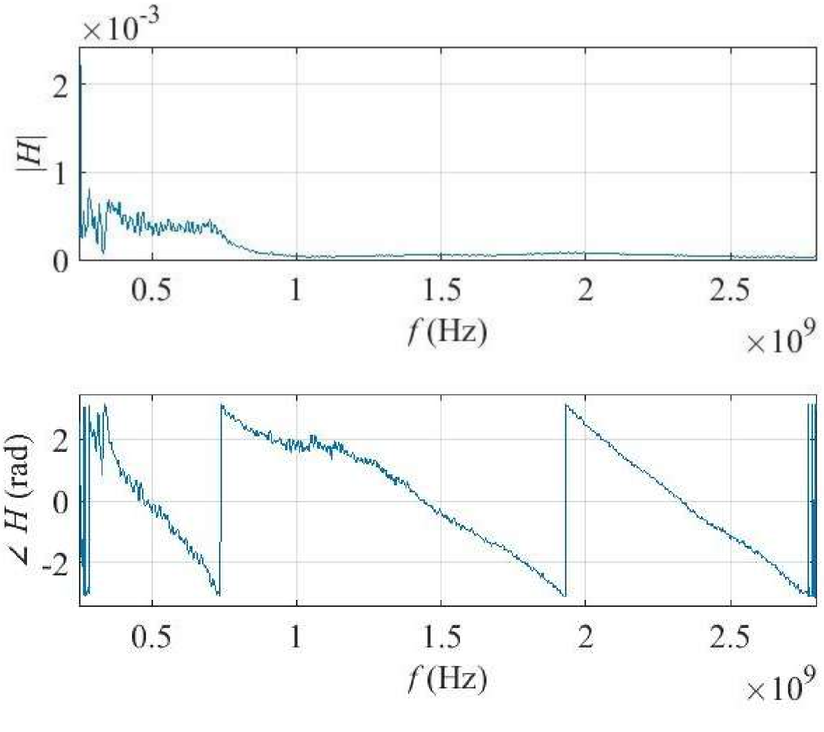

Figure 4.2: Combination of the transmitting (H_t) and receiving (H_r) transfer functions, H.

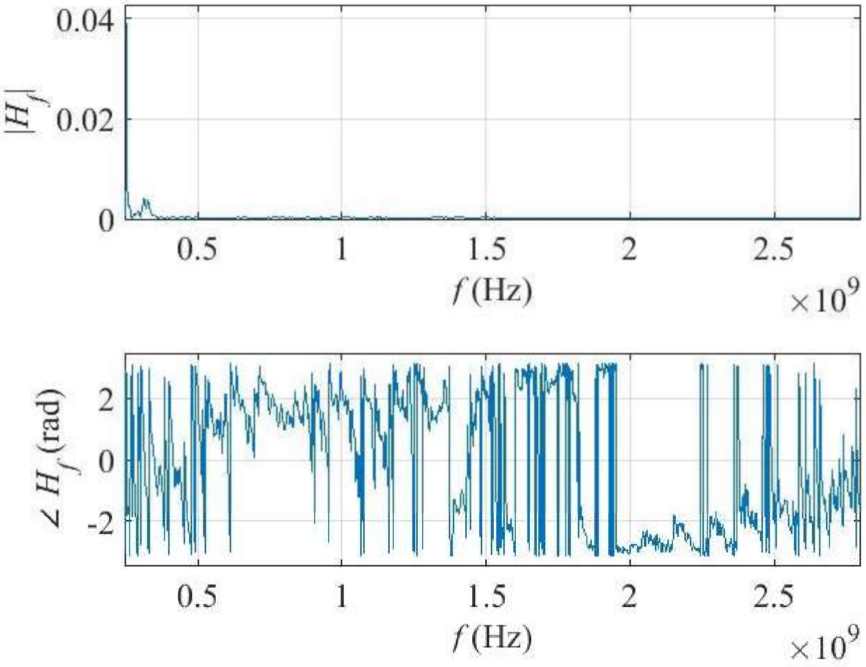

Figure 4.3: Feedback loss transfer function, H_f.

Figure 4.4 illustrates the complex return loss transfer functions, H_i for both calibrations. The blue and red curves represent H_i resulting from the calibration of the radar system without and with the handle respectively. The small variations indicate that the handle does not effect much the antenna performances but the differences are significant enough to affect the inversions.

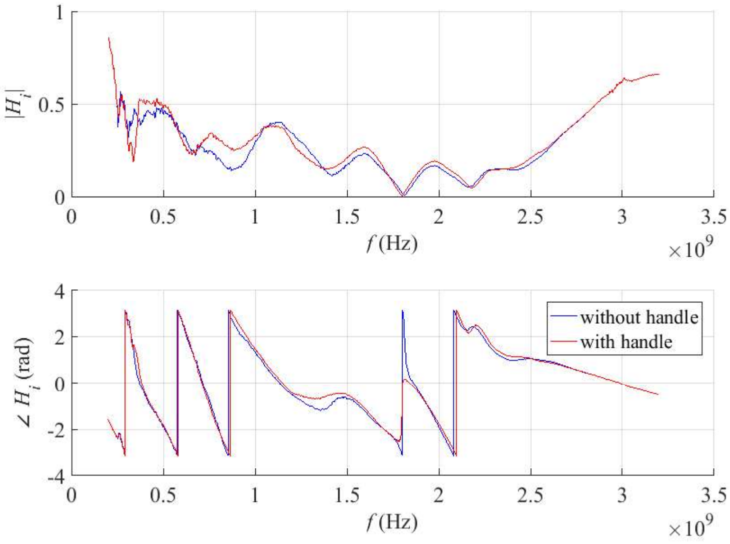

Figure 4.4: Complex return loss transfer functions, H_i for both calibrations.

4.1.2 Laboratory tests

The radar images shown in this section represent the amplitude of the signal which is function of the traveling time t [s] and the position on the transect *Measurement index.* The amplitude is characterized by a colour bar (Fig. 4.5). The reflection at an interface is in fact characterized by an oscillation between a positive maximum and a negative minimum.

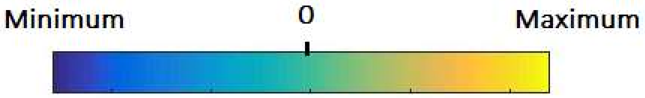

Figure 4.5: Colour bar representing the signal amplitude.

Figure 4.6 illustrates the radar image for an antenna height of 1.5 cm over the sand surface. The antenna filter has not yet been applied on these measurements.

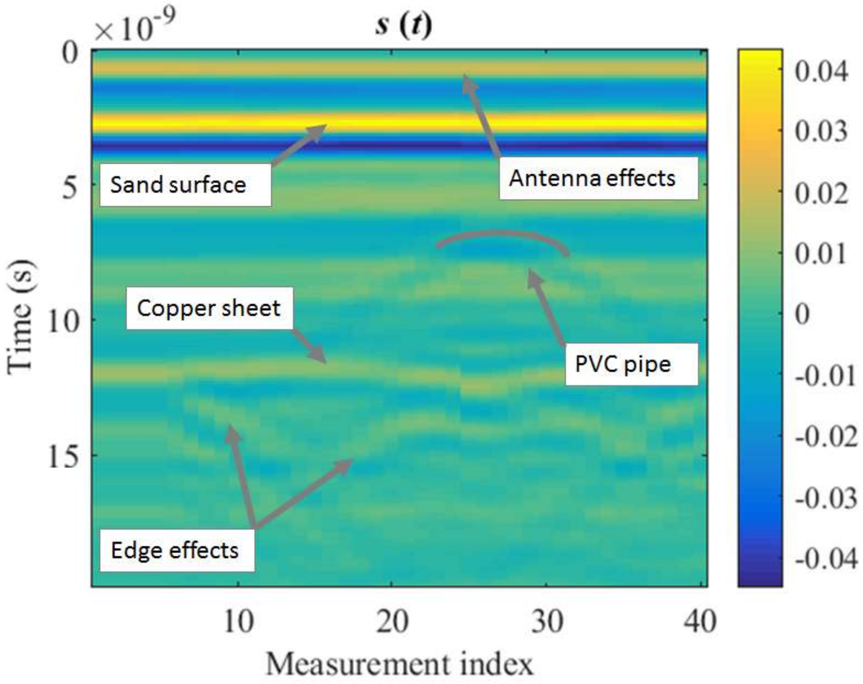

Figure 4.6: Radar image without antenna filtering at a height of 1.5 cm over the sandbox.

The first two colored stripes (yellow and blue) located on top of the image correspond to reflections that occur between the antenna feed point and antenna aperture (antenna internal reflections). The reflection occurring at about 3 ns corresponds to the sand surface and the reflection occurring at about 12 ns corresponds to the copper sheet at the bottom of the sandbox. Between measurements 25 and 30, we can distinguish the PVC pipe with a hyperbolic shape on the radar image. Underneath it, we can see that the stripe that corresponds to the copper sheet is not perfectly horizontal. This is due to the presence of water under the PVC pipe (former experiment with a water leak). Finally, under the "copper sheet" stripe, we can observe different diagonal stripes that must result from the edge effects of the sandbox.

The three following figures (Fig. 4.7(a), 4.7(b) and 4.7(c)) illustrate the radar images (with and without filtering) for an antenna height of 30 cm above the sandbox. The first figure has not been filtered for the antenna effects while the second has been filtered for H_i and the third one has been filtered for H_i, H and H_f. The other radar images for antenna heights 1.5 cm, 10 cm, 20 cm and 40 cm are illustrated in Appendix A.7.

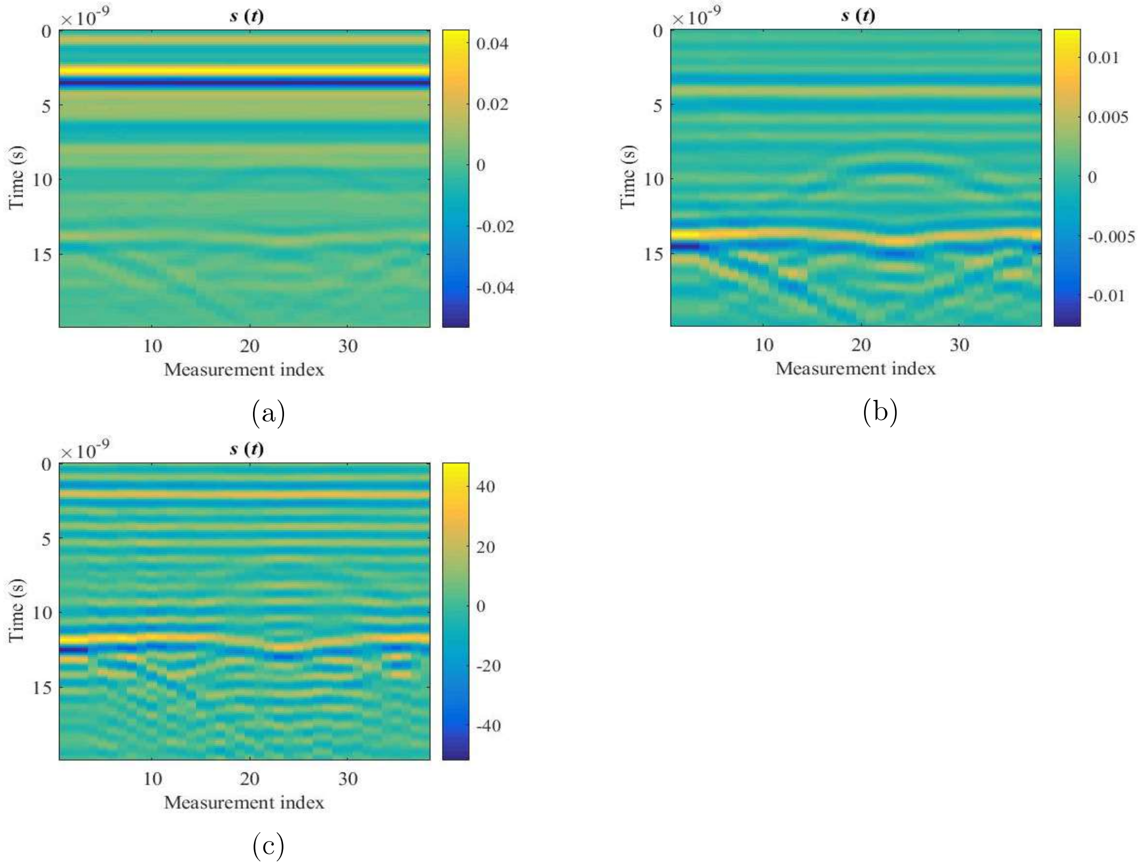

(a)

(b)

(c)

Figure 4.7: Radar images over the sandbox with the antenna situated at 30 cm from the sand surface. (a) Raw radar data. (b) Radar data from which H_i has been subtracted. (c) Radar data from which antenna effects have been filtered out using the radar equation.

By applying filtering, we can see that reflections previously observed on top of the sand surface have disappeared. In Figure 4.7(c), the first yellow stripe now corresponds to the sand surface. The hyperbola (PVC pipe) and the lower planar reflection (copper sheet) are both brought to light with the help of filtering. We can also observe on this figure that the signal is offset in time. The stripes are a bit higher on the vertical axis. This means that the $t = 0$ s now matches with the phase center of the antenna while it corresponds to the antenna connector in the raw radar data (Fig. 4.7(a)).

As a conclusion, applying the antenna filters on the radar signals enables to:

- remove the reflections that occur within the antenna,
- remove the reflections between the antenna and the sand surface,
- offset the signal along the vertical axis.

We also concluded that the best antenna height to carry out measurements above the soil surface is between 20 cm and 30 cm. The handle added to the radar system was adjusted to this height.

4.1.3 Numerical simulations

Figures 4.8 and 4.9 show examples of radar simulations in the frequency domain. For each simulation, different values were specified for each property (h, ε_r, σ and μ) . The first simulation (Fig. 4.8) is characterized by the following properties:

- thickness of the 1^{st} layer (h) = 0.20 m,
- $\varepsilon_r = 3$,
- $\sigma = 5.10^{-4}$ S/m,
- $\mu_r = 1$.

Whereas the second simulation (Fig. 4.9) has the following properties:

- thickness of the 1^{st} layer (h) = 0.30 m,
- $\varepsilon_r = 6$,
- $\sigma = 8.10^{-3}$ S/m,
- $\mu_r = 1$.

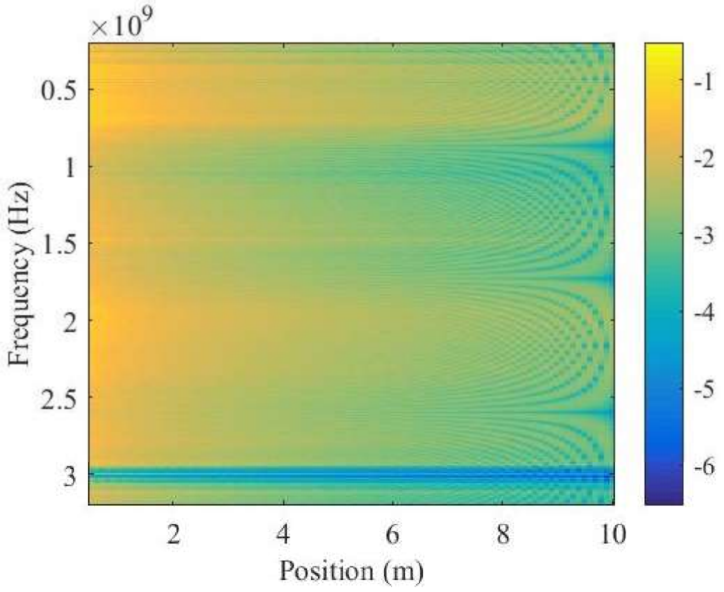

Figure 4.8: First numerical simulation characterized by: $h = 0.2$ m, $\varepsilon_r = 3$, $\sigma = 5.10^{-4}$ S/m, $\mu_r = 1$.

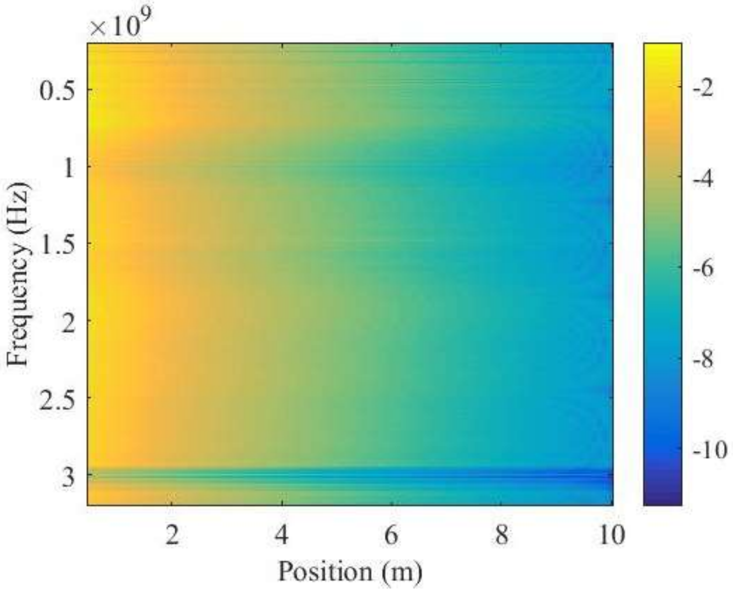

Figure 4.9: Second numerical simulation characterized by: $h = 0.3$ m, $\varepsilon_r = 6$, $\sigma = 8.10^{-3}$ S/m, $\mu_r = 1$.

The values given to the dielectric permittivity and the electrical conductivity in Figure 4.8 conform to typical dry sandy soil properties. In fact, the dielectric permittivity of a sandy soil ranges from 2 to 20 and the electrical conductivity from 0 S/m up to 1.10^{-2} S/m depending on soil moisture and salinity (Jol, 2010).

In contrast to the radar images showed in the previous section, the y-axis represents the frequencies [Hz] and the x-axis indicates the soil depth [m]. The colour bar does not represent the signal amplitude $S(f)$ but it is defined as S_d, the difference between the signal amplitude at the kth depth and the signal at the maximum depth (10 m). The signal was then plotted as the logarithmic of the absolute value of (S_d) in the frequency domain. The radar system's dynamic range or sensitivity permits to detect differences as low as 10^{-3} (yellow to green on the colour bar). This value corresponds to a signal amplitude ($S(f)$) of + 0.001 or - 0.001 which defines the sensitivity of the radar system.

According to Figure 4.8, the ground penetrating radar is able to record signals down to approximately 6 meters (yellow and orange colours). We can also observe at which frequencies the radar system works efficiently. It is quite efficient for low frequencies (200 MHz to 700 MHz). The advantage of low frequencies is that the signal is able to penetrate deeper in the soil but in return, the resolution is weaker. In contrast, higher frequencies lead to a better resolution but do not penetrate as deep. The radar is also efficient for higher frequencies that range between 1800 MHz and 2300 MHz.

Figure 4.9 shows the case with a higher dielectric permittivity ($\varepsilon_r = 6$) and a higher electrical conductivity ($\sigma = 8.10^{-3}$ S/m) than the previous one. In addition, the GPR height is set to 0.3 m over the sand surface. With these soil properties, the propagation of the signal is limited in depth to approximately 2.5 meters. This is due to the values given to the dielectric permittivity and electrical conductivity. Larger is the surface dielectric permittivity, larger is the surface reflection and hence, less energy is transmitted into the ground. In addition, larger is the electrical conductivity, more rapidly the waves are attenuated into the ground. Both permittivity and conductivity increase with water content.

4.1.4 Field tests

Figure 4.10 shows the recorded GPS data. Each point is represented by x and y values in the UTM (Universe Transverse Mercator) projection system. The datum has been translated to the origin (0,0). Figure 4.11 shows the radar image with the antenna filtering.

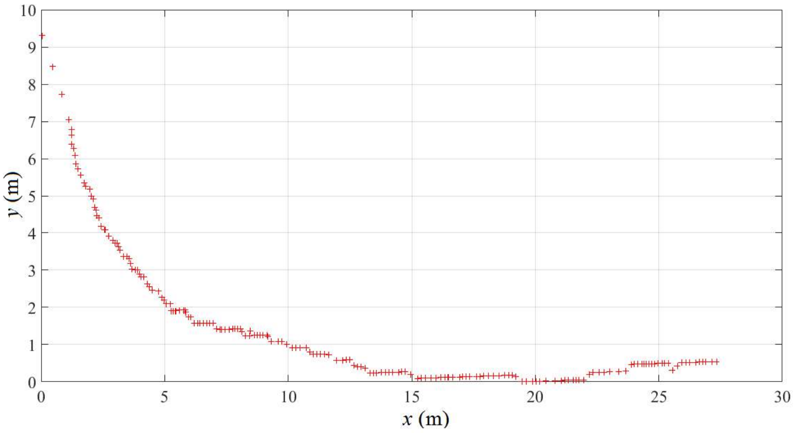

Figure 4.10: Parking lot field test: georeferenced data points of the GPR acquisition points.

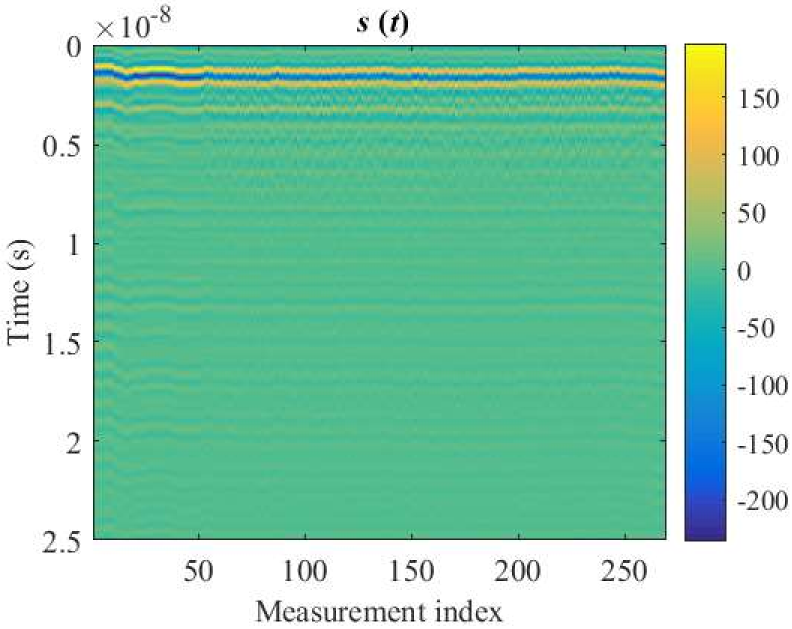

Figure 4.11: Parking lot field test : GPR image with filtering.

A second field test took place along the exterior wall of the *Génie Rural* building. Figure 4.12 shows the radar image of the wall composed of different layers of materials.

On this radar image, we observe two major reflections which correspond to the wall surface and wall blocks, respectively. The distance separating both interfaces is estimated to be approximately 10 cm.

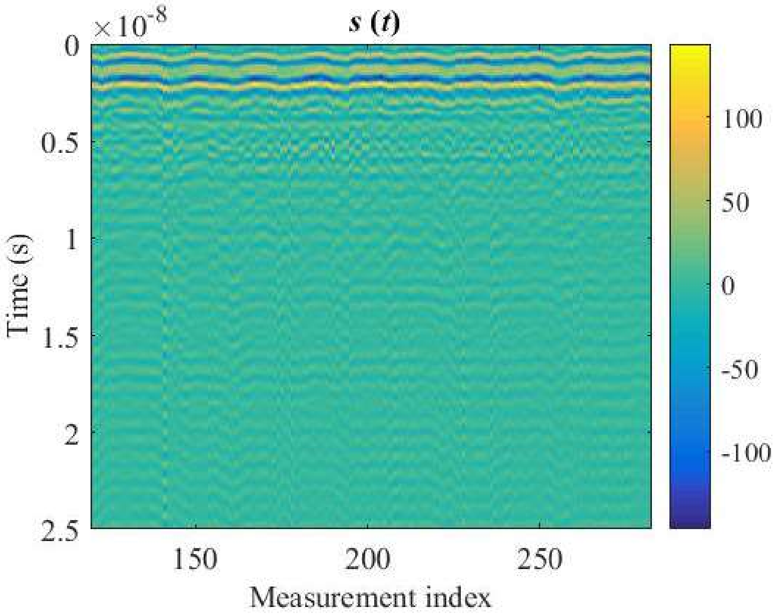

Figure 4.12: Wall field test: GPR image with filtering.

This brings to an end the first part of this chapter. The presented results showed that our new lightweight frequency domain GPR is operational. The second part of this chapter exposes the field results in Morocco.

4.2 Dendrometric results

For each plot, mean circumference (C_{mean}), mean height (H_{mean}), survival rate (S_r), dominant height (H_{dom}) and basal area (G) are indicated in Table 4.2. Table 4.1 below shows the basic statistics related to each variable presented in Table 4.2.

Table 4.1: Basic statistics of the dendrometric variables (mean, minimum, maximum, median, variance and standard deviation).

	mean	min	max	median	var	std
C_{mean} [cm]	35.8	16.0	60.3	34.6	117.9	10.9
H_{mean} [m]	5.0	2.2	8.9	4.5	3.3	1.8
S_r [%]	58.2	5.6	100.0	61.8	651.3	25.5
H_{dom} [m]	6.3	2.2	10.2	5.9	5.0	2.2
G [m^2/ha]	9.5	0.1	34.8	7.6	59.4	7.7

As expected, we observe that there is a high variability in terms of mean circumferences, mean heights and survival rates (H_{dom} and G are calculated based on C and H). Mean circumference varies between 16 cm and 60.3 cm, mean height between 2.2 m and 8.9 m and survival rates range between 5.6 % and 100 %. The high standard deviations further prove this variability. In fact, this measure is used to quantify the amount of dispersion of the data values. If the value is high, this means that the data points are spread out over a large range of values.

Table 4.2: Dendrometric results per plot: C_{mean}, H_{mean}, S_r, H_{dom} and G

Plot	C_{mean} [cm]	H_{mean} [m]	S_r [%]	H_{dom} [m]	G [m^2/ha]
1	40.6	5.1	64.3	6.4	9.9
2	47.3	7.0	80.0	9.6	18.7
3	39.1	5.4	85.7	7.4	11.6
4	48.0	7.0	70.6	9.4	17.8
5	27.4	3.6	45.7	4.6	3.9
6	35.2	4.2	20.5	4.9	2.4
7	30.4	4.1	55.2	5.6	6.7
8	24.1	3.1	34.3	4.6	2.9
9	16.0	2.2	5.6	2.2	0.1
10	27.3	3.1	41.2	4.0	3.3
11	32.7	4.2	82.4	6.8	11.8
12	36.0	4.5	69.4	6.1	7.8
13	36.2	4.9	80.0	4.7	11.9
14	34.3	4.7	86.1	5.9	11.1
15	33.9	4.7	71.4	6.1	7.4
16	27.0	3.4	37.1	4.9	2.6
17	19.7	2.5	9.1	2.8	0.4
18	25.5	3.1	28.6	3.5	1.8
19	22.8	3.3	46.3	4.2	3.1
20	34.8	4.6	69.7	5.9	10.0
21	25.2	3.5	51.4	4.8	4.1
22	28.3	3.7	42.9	5.9	3.4
23	28.1	3.6	24.1	4.4	1.9
24	30.4	4.2	53.1	5.7	6.0
25	47.1	7.3	85.7	9.5	16.8
26	51.0	7.2	93.8	8.1	18.2
27	35.5	4.7	41.9	5.4	6.4
28	24.2	3.1	31.3	4.1	1.9
29	46.3	5.9	59.4	8.4	16.7
30	30.6	3.9	28.1	5.1	3.1
31	38.6	5.8	68.2	9.4	11.4
32	52.8	7.4	73.3	9.7	16.5
33	48.2	7.2	80.6	9.2	14.5
34	60.3	8.9	82.4	9.4	34.8
35	50.2	8.2	100.0	9.3	20.7
36	54.0	8.9	96.4	10.2	21.4

(a) (b)

Figure 4.13: Comparison of tree heights and circumferences of two dendrometric plots. (a) Cork oaks located in plot 34. (b) Cork oaks located in plot 9.

The two pictures depicted in Figure 4.13 illustrate the high variability described previously. The left picture (Fig. 4.13(a)) shows trees located in plot 34. Regeneration was successful in this area of the study plot. In contrast, the right picture (Fig. 4.13(b)) reveals the important contrast observed in the field. These trees are located in plot 9, only 500 m away from plot 34. It has many regeneration issues and the lowest survival rate.

To support this, the two histograms presented in Figure 4.14 indicate the frequency (in %) of tree circumferences and heights of every tree located in the 36 dendrometric plots.

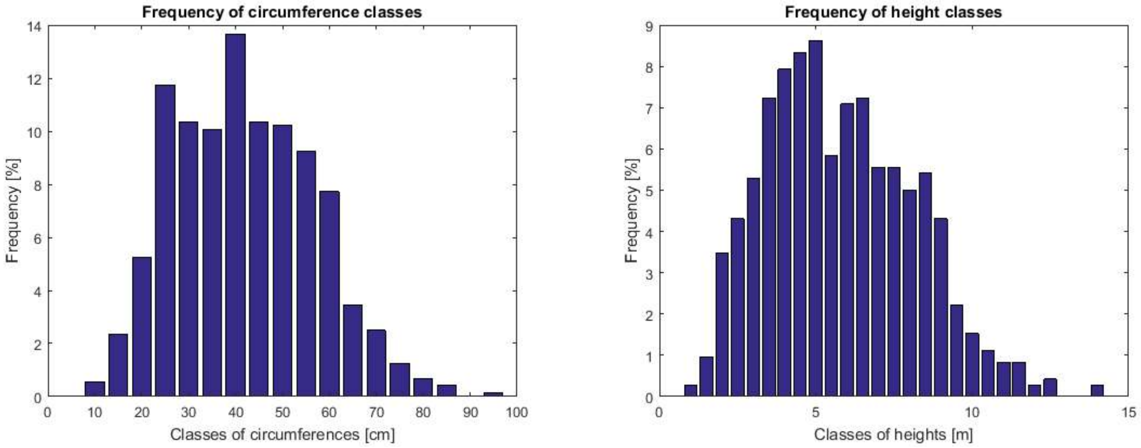

(a) (b)

Figure 4.14: (a) Frequency of tree circumferences [cm], (b) Frequency of tree heights [m].

Once more, we observe the same high variability in terms of circumference (10-95 cm) and height (1-14 m). Both histograms have a distribution that looks like a Gaussian curve. This is discussed in the next section.

In addition of this high variability in terms of tree growth, our study area has survival issues. In fact, one third of our study plots have survival rates below 50 %. Plots 9 and 17 are characterized, respectively, by 5.6 % and 9.1 % of survival rates. These are the lowest rates measured in our study area. Both plots are also characterized by the lowest dominant heights (2.17 m and 2.80 m, respectively).

The dominant height varies between 2.2 m and 10.2 m with a mean value of 6.3 m for all 36 dendrometric plots. This variable varies on an ongoing basis. Consequently, it represents more precisely the forest growth than the mean height (Rondeux, 1993). Figure 4.15 shows a map of the dendrometric plots classified according to the dominant height. It gives us an idea of the successful regeneration plots. The map shows each plot represented by a colour code from best (dark green) to worst (bright red).

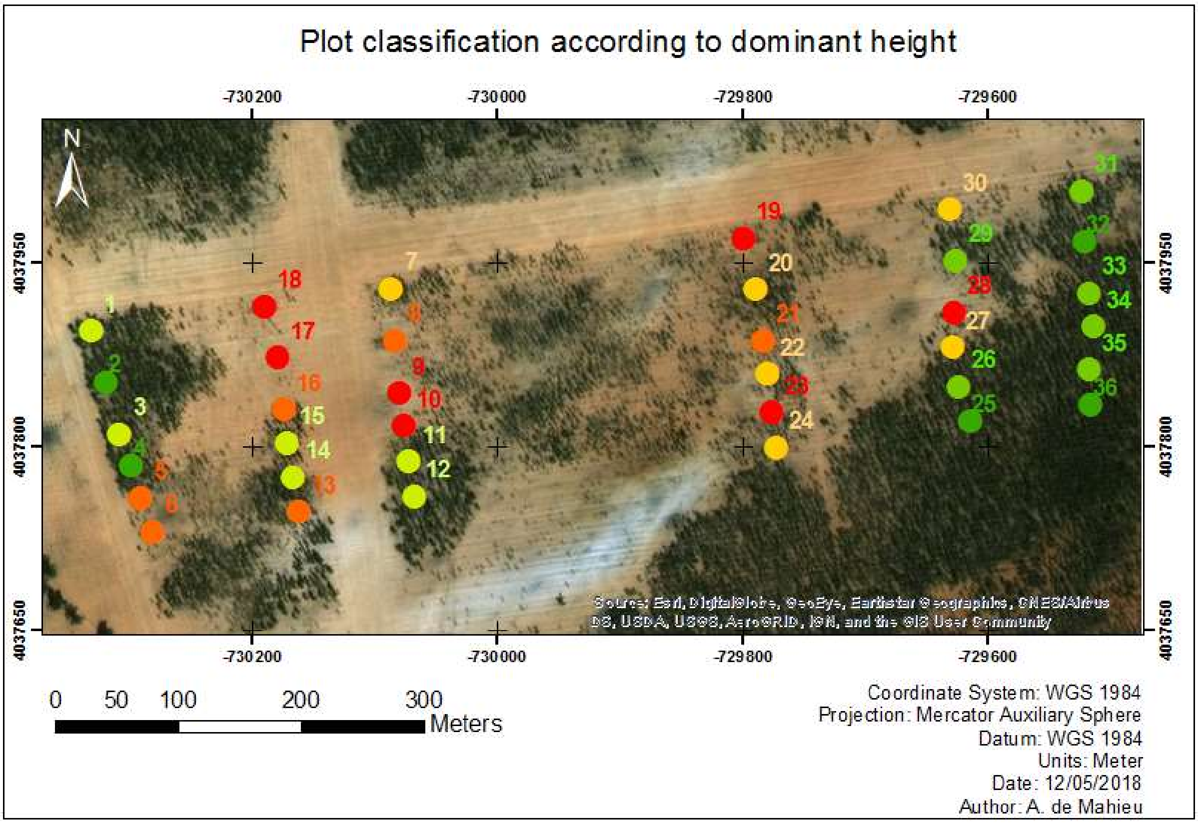
Plot classification according to dominant height

Source: Esri, DigitalGlobe, GeoEye, Earthstar Geographics, CNES/Airbus DS, USDA, USGS, AeroGRID, IGN, and the GIS User Community

Coordinate System: WGS 1984
Projection: Mercator Auxiliary Sphere
Datum: WGS 1984
Units: Meter
Date: 12/05/2018
Author: A. de Mahieu

Figure 4.15: Plot classification according to dominant height from best (green) to worst (red). Each dendrometric plot is marked by its respective plot number.

The upper left corner and the right side of the study plot are the most successful areas in terms of tree growth. The main causes that led the other plots to decline are discussed below.

Finally, the basal area calculated per plot based on circumference measurements is rather uneven. In forestry, basal area is a good indicator of forest density. It varies between 0.1 m^2/ha and 34.8 m^2/ha.

Table 4.3 shows the determination coefficients (R^2) between each dendrometric variable presented in this section.

Table 4.3: Determination coefficient R^2 between the different dendrometric variables.

	C_{mean}	H_{mean}	H_{dom}	S_r	G
C_{mean}	1.00	0.96	0.86	0.63	0.88
H_{mean}		1.00	0.89	0.66	0.89
H_{dom}			1.00	0.66	0.76
S_r				1.00	0.67
G					1.00

We observe that there is a strong correlation between C_{mean} and H_{mean} ($R^2 = 0.96$, p-value < 0.05). Figure 4.16 shows the mean circumference per plot as a function of the mean height per plot.

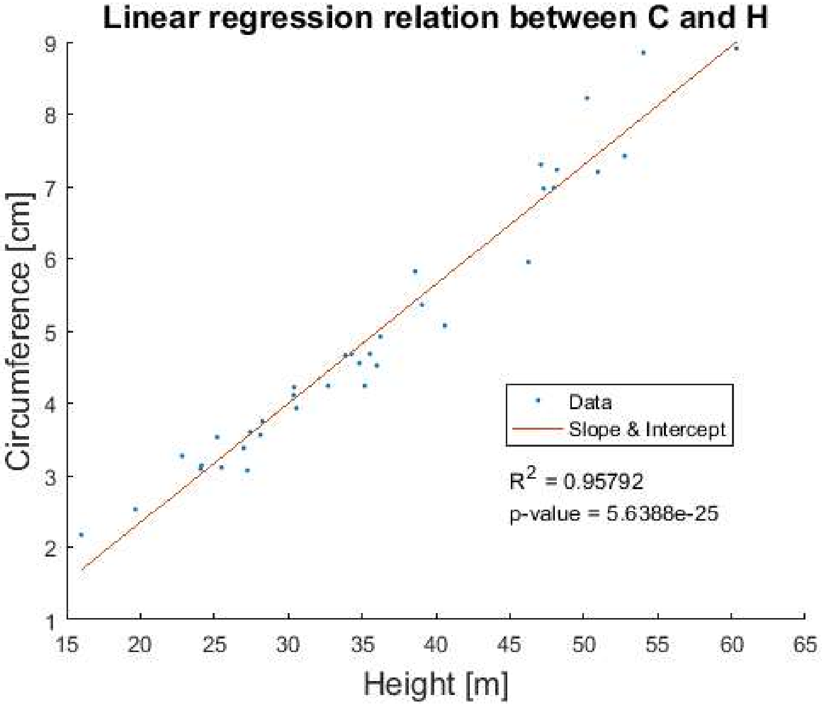

Figure 4.16: Mean circumference as a function of mean height with linear regression.

As expected, this graph shows that there is a strong correlation between both variables as the data points are not scattered and are close to the regression line.

Growth status of cork oaks

It is hard to imagine that our study area is composed of cork oak trees of the same age. The high variability observed in terms of tree circumference and tree height is quite impressive in my opinion. Mean circumference per plot ranges between 16 cm and 60 cm, which is almost four times more. Quite a few trees are characterized by low circumferences ($<$ 20 cm) which is surprising considering the age of the cork oaks. This may be linked to regeneration issues. Nevertheless, according to Figure 4.14(a) the circumference distribution looks like a Gaussian curve which is specific of even-aged stands. These observations are also applicable to tree heights. The mean height per plot throughout our study area is equal to 5 m whereas trees higher than 10 m were measured. In contrast, a large amount of small trees ($H < 2$ m) were identified. According to Figure 4.14(b), the height distribution looks more or less like a Gaussian curve. In a even-aged stand, tree heights should have lower variations than the ones observed in our study area. The soil characteristics seem to be the principal reason of these variations as discussed in the next section.

Survival rates are quit erratic from one plot to another. The most successful plots are characterized by high rates ($>$ 80 %) and the worst plots in terms of regeneration have rates below 10 %. Note that these rates are estimations as the survival rates were calculated by counting the number of living and dead trees, tree stumps and empty locations (see Section 3.3). This was based on the initial distance separating the seedlings (3 m). Moreover, it is also important to mention the human pressure that is exerted on our study plot. In fact, the plot is prone to different kind of pressures. Shepherds let their animals graze in the middle of the forest. Sheep and cattle feeds on acorns, small bushes and on young tree seedlings when the vegetation is scarce (particularly during summer). Shepherds even sometimes cut down cork oak branches to feed their animals with leaves. Axe blows were identified on some trees. This is illustrated in Figures 4.17. Additionally, local inhabitants fell trees to sell the firewood to local markets. Finally, traces of ancient fires were observed near plots 9 and 28 (illustrated in Figure 4.18) which can explain their very low survival rates. Human pressure is certainly not the main factor that impacts successful regeneration of cork oak plots but I found it important to mention it as Maâmora forest has been subject to this issue for many years.

(a) (b)

Figure 4.17: Impact of local inhabitants on cork oak growth. (a) Cut branch by shepherd to feed sheep and cattle. (b) Axe blow on cork oak tree.

Figure 4.18: Traces of ancient fires in the middle of our study area.

4.3 GPR results

4.3.1 Soil surface water content estimation using the frequency domain GPR

Relative dielectric permittivity map of the study area

Figure 4.19 shows the map of the relative dielectric permittivity of our study area obtained by kriging using the frequency domain GPR. It is based on the 14 GPR transects that were drawn with the radar system. A map of the data points derived from the inversion method is available in Appendix A.8. These points are stacked over the kriging map to compare both results.

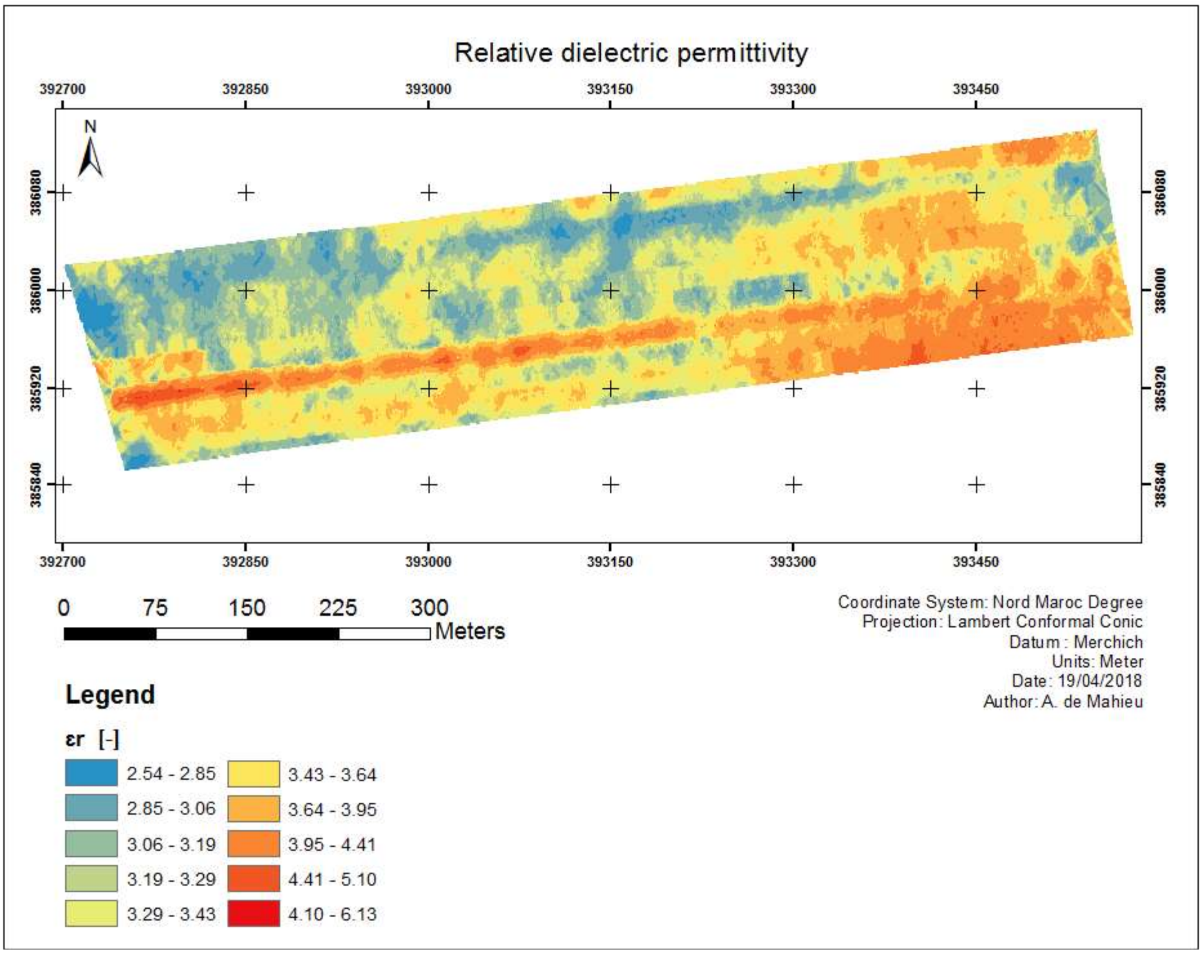

Figure 4.19: Relative dielectric permittivity (ε_r) map of our study area obtained by kriging using our frequency domain GPR.

When ε_r increases, this means that water content is higher at the soil surface. This is represented by orange and red colours in Figure 4.19. Bright blue colour represents drier areas whereas red colour illustrates more moist areas. When comparing this map to the satellite view of the plot, we can easily distinguish that trees are in better shape where ε_r is higher. This is observable in the lower right corner of this map. However, in the upper left corner, which is characterized by successful regeneration plots (i.e., high dominant heights and high survival rates), the relative dielectric permittivity seems low (blue color). We discuss the possible links between these variables in Section 4.5.

In addition, a red line with high permittivities crosses the study plot. It corresponds to the first transect (T2) where GPR data was recorded. We believe that the measuring points were overestimated for this transect. This may be linked to the fact that the GPR had not yet reached a constant functioning temperature. Hence the recorded data for this transect may not reflect the reality in the field.

Figure 4.20 shows the histogram of the relative dielectric permittivity values of all GPR recorded data points. The y-axis represents the number of data points.

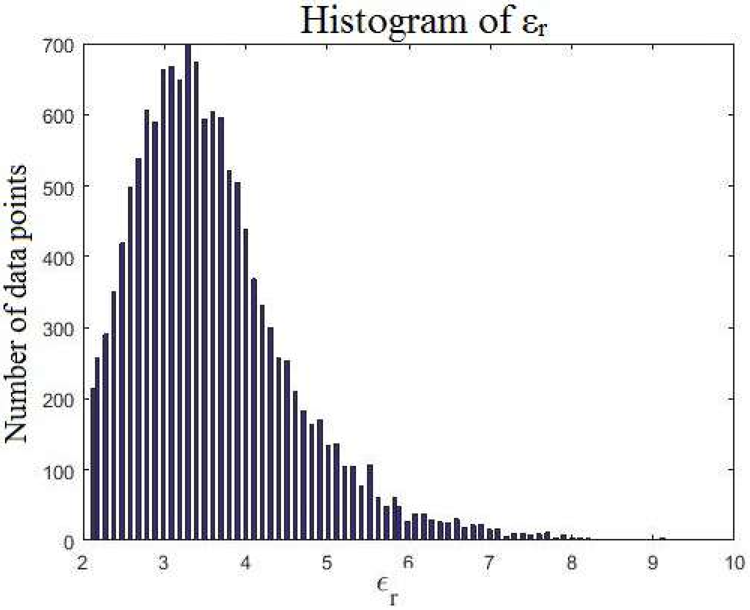

Figure 4.20: Histogram of relative dielectric permittivity (ε_r data points).

The values of ε_r range between 2.1 and 9.7 (see Fig. A.17). As you can see on the bar chart, a large number of the recorded data points range between 3 and 4. Note that ε_r increases or decreases significantly from one point to another.

Mean dielectric permittivity estimated per plot

Using *ArcGIS* tools, the mean dielectric permittivity per plot was estimated. For each plot, every GPR permittivity point included in a dendrometric plot was selected and a mean value of these points was calculated. These values are presented in Table 4.4 below. The number of points selected varies from one plot to another. For plots 1 and 8 no mean value was calculated because the GPR did not record any values in these zones.

Table 4.4: Mean relative dielectric permittivity (ε_r) per plot.

Plot	ε_r **[-]**	**Plot**	ε_r **[-]**	**Plot**	ε_r **[-]**
1	N/A	13	3.43	25	4.01
2	4.00	14	3.44	26	3.96
3	3.83	15	4.19	27	4.33
4	4.96	16	3.47	28	3.51
5	3.67	17	3.90	29	3.67
6	3.44	18	2.79	30	2.77
7	3.02	19	2.74	31	3.02
8	N/A	20	3.31	32	3.64
9	3.49	21	3.26	33	3.37
10	4.10	22	4.11	34	3.18
11	3.42	23	3.23	35	4.09
12	3.60	24	3.28	36	4.43

In Figure 4.19, we observe that the upper left corner of the map (plots 1, 2, 3 and 4) is characterized by lower permittivity values (blue colour). The table above shows that the mean permittivity calculated for plots 2, 3 and 4 is higher than expected. This proves that ε_r can very significantly over short distances and the interpolation applied by the kriging method therefore mislead our interpretation. In contrast, the plots located in the eastern part of our study area (plots 25, 26, 27, 34, 35 and 36) have higher values as expected (red colour in Fig. 4.19).

The mean permittivity per plot is used in further analyses to link soil surface moisture to other variables such as tree growth and clay layer depth.

Soil surface water content map of the study area

Figure 4.21 shows the estimated soil surface water content map of the study area. For each permittivity point obtained by the radar data inversion method, we calculated the volumetric water content (θ_v) using Topp's equation. The same kriging method was applied to obtain this map.

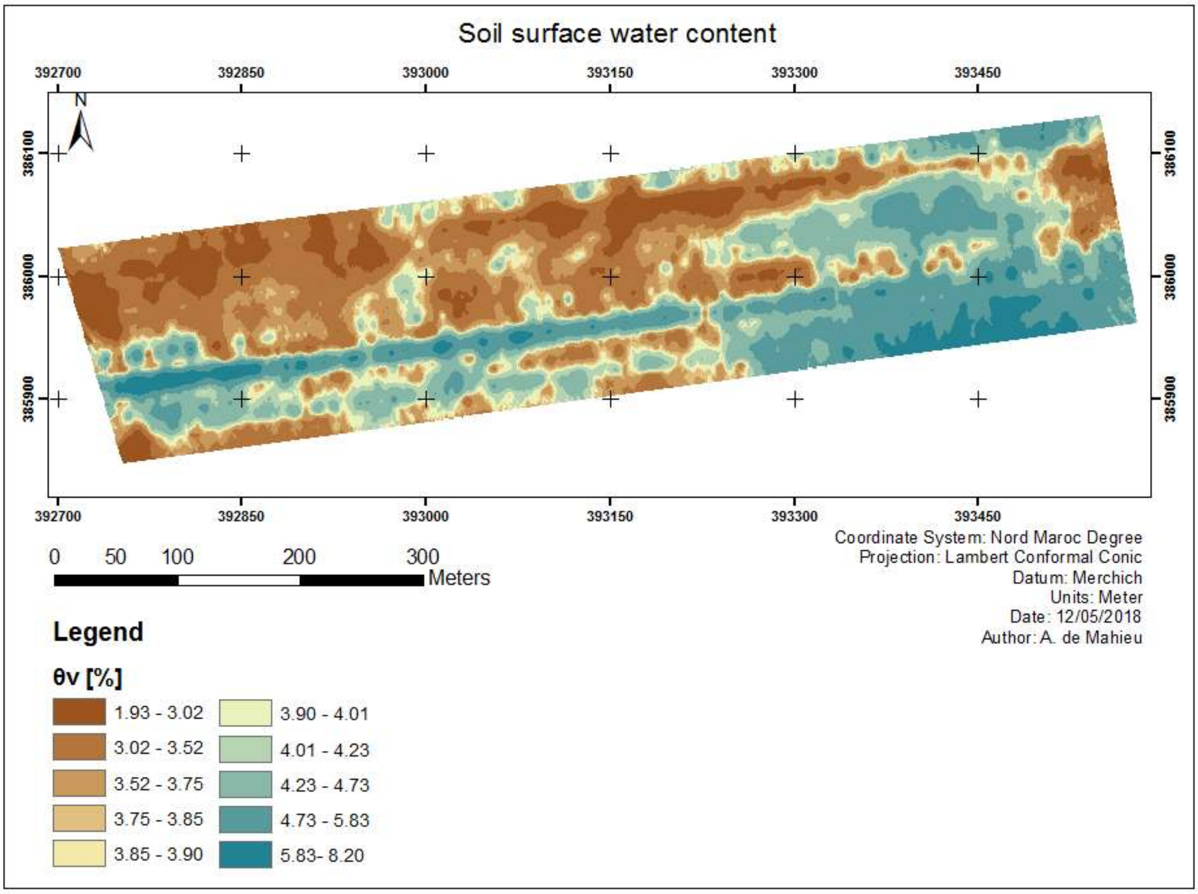

Figure 4.21: Surface volumetric water content (θ_v) map of our study area obtained by kriging using our frequency domain GPR.

The drier areas (brown colours) have an estimated volumetric water content (θ_v) equal to 2 % - 3 % whereas the most humid areas (dark blue colours) have a θ_v that ranges between 6 % and 8 %. The observations described in the previous map are applicable to this one as the calculated values of θ_v only depend on ε_r.

Drift in the GPR data

Because the first transect (T2) does not seem to indicate values that reflect the field reality (see above), we decided to remove all the recorded GPR data points from the first transect as we were unable to determine wheter and when the GPR started to work properly. Figure 4.22 shows the new map of the estimated mean dielectric permittivity of the study plot obtained by kriging without the data points of the first transect. The red line disappeared and the rest of the map appears coherent.

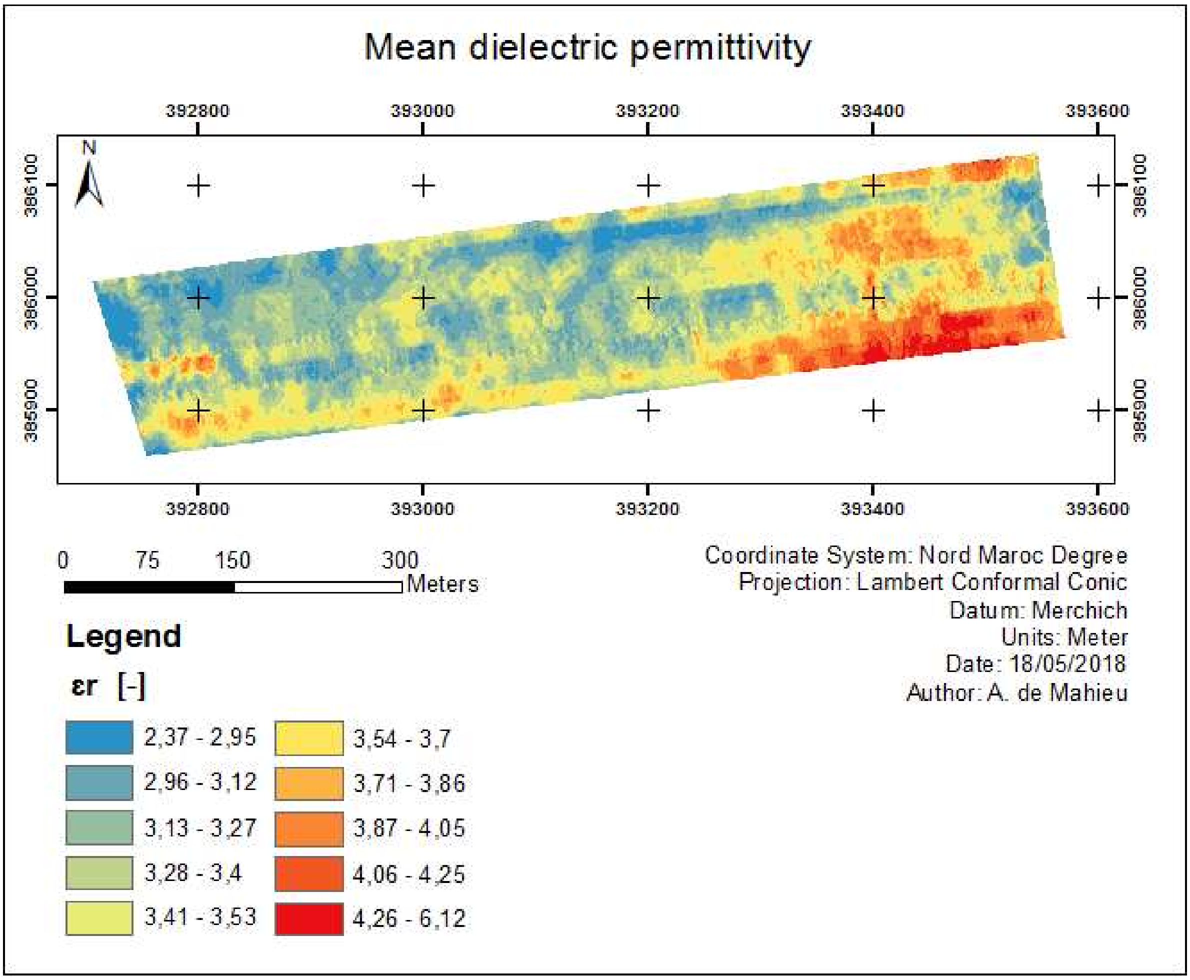

Figure 4.22: Relative dielectric permittivity (ε_r) map obtained by kriging without the first transect using our frequency domain GPR.

Without the data points of this first transect, it is no longer possible to estimate the mean ε_r of plots 4, 10, 15, 22, 27 and 34 which are the plots crossed by this GPR transect. Later in this chapter, we will not be using these permittivity values as they are probably overestimated as explained before.

Limitations

It is important to mention that the values of ε_r were probably underestimated. The dielectric permittivity of a dry sand is around 3. The values observed in the field by GPR are close to that value. However, although the top first centimeters of sand appeared to be indeed dry, the lower layers looked relatively moist. As a result, either our characterization depth was lower than expected, the dry-moist dielectric contrast led to interferences, or the obtained values were underestimated. Nevertheless, the map presented in Figure 4.19 is especially useful to highlight soil relative moisture patterns within the field. The values of mean ε_r are hence compared from one plot to another and not values as such, so the underestimation is not significant for our data analysis.

Regarding the acquisition of the radar data, let us recall that the calibration of the antenna carried out at UCL was not applicable in Morocco as the VNA was disconnected from the antenna during transportation. Fortunately, we were able to carry out a calibration on top of a daya (temporary pond). For further field measurements abroad, I would suggest the GPR operator to have access to a perfect electrical conductor (PEC) on site to avoid this kind of problem or to avoid separating the VNA from the antenna during transportation. Finally, we suspect that carrying the radar with a handle is not the most appropriate way to record GPR data. In fact, the GPR is very close to the operator's leg which may create interference around the antenna. By placing the radar system on a quad, we could avoid this kind of issue.

Finally, the GPR system could have been tested in more moist conditions than a perfectly dry sand (see Section 2.2.2). The soil was more moist in the field than expected which prevented us of detecting the clay layer interface as the EM waves were rapidly attenuated in the soil profile. Another idea would be to carry out the same measurements in summer with drier conditions and see if the clay layer depth is observable on these radar images.

4.3.2 Clay depths estimation using the time domain commercial GPR

Figures 4.23 and 4.24 show the radar image of sub-transects 2A and 4. All seven 2015 radar images are displayed in Appendix A.9. As a reminder, this time domain commercial radar has a central frequency of 400 MHz and frequencies that range from 80 MHz up to 800 MHz were considered (band-pass filter).

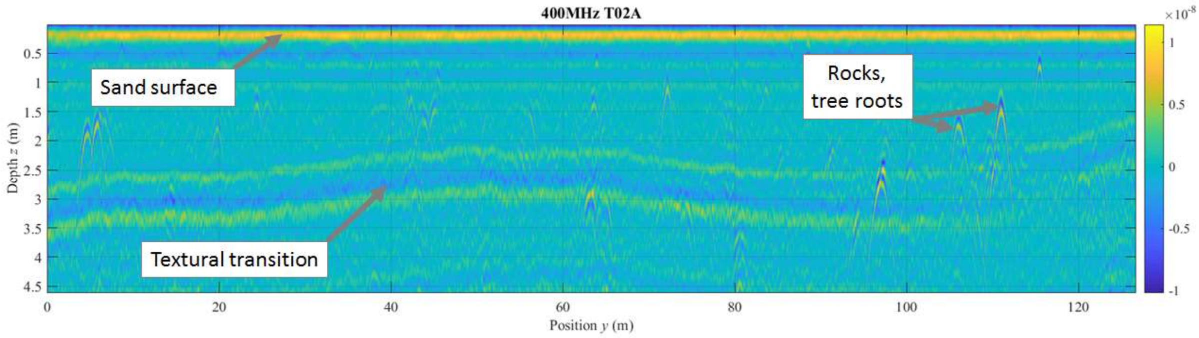

Figure 4.23: Radar image of sub-transect 2A using a time domain commercial GPR and GSSI positioning wheel (central frequency = 400 MHz) (F. André, 2015).

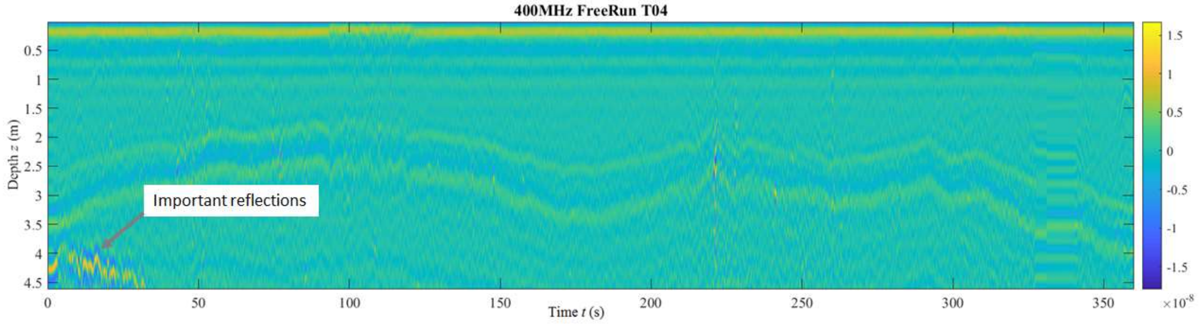

Figure 4.24: Radar image of sub-transect 4 using a time domain commercial GPR in "Free Run" (central frequency = 400 MHz) (F. André, 2015).

The surface reflection is distinguishable on the radar image of sub-transect 2A (Fig. 4.23) by a bright blue-yellow coloured stripe (at $z = 0$ m). At a depth $z \approx 3$ m, important reflections are observable along the sub-transect. These are due to a change in soil electromagnetic properties most likely originating from a textural transition or waterfront. Along the transect, this textural transition varies from about 2 m to 4 m. Moreover, small reflections on short distances are observable. These local reflections with a hyperbolic shape must be small rocks or tree roots. We cannot say with certainty that the continuous wave reflection indicates the clayey layer. In fact, in certain GPR images like sub-transect 4 (Fig. 4.24), other important reflections are observable beneath this main reflection. This means that the EM waves were not completely attenuated within this second layer and thus its clay content is expected to remain relatively low. Additionally, we assume that this reflection is rather a textural transition than a contrasted waterfront for the same reason as EM waves would have been much more attenuated if this second layer would have been very moist.

Nevertheless, these radar images allow us to estimate the textural transitions depths for both transects. For each dendrometric plot crossed by one of the two transects, the depth of the textural transition measured by the radar is indicated in Table 4.5. Note that the first GPR transect of 2015 matches with transect T28 (see Fig. 3.5) and hence crosses six dendrometric plots (plots 6, 12, 13, 24, 25 and 36, see Fig. 3.2). The second transect is located between GPR transects T14 and T16 and thus does not cross any dendrometric plot. However, as the distances separating the dendrometric plots and this second transect were shorter than 15 m, we chose to take into account of all twelve plots as well.

Table 4.5: Estimated textural transition depth per plot using the 2015 radar images.

Plot	Depth [m]	Plot	Depth [m]	Plot	Depth [m]
1	N/A	13	3.0	25	3.5
2	N/A	17	2.2	29	1.8
6	3.0	18	2.2	30	1.8
7	3.0	19	4.2	31	2.5
8	3.0	20	4.2	32	2.5
12	1.8	24	3.0	36	N/A

By connecting soil profile locations of every dendrometric plot with these two transects, we are able to compare the results given by the radar system and the ones obtained by the soil laboratory analyses. These analyses are presented in the next section.

4.4 Soil results

4.4.1 Hand-touch analysis to estimate soil texture in depth

Results from hand-touch analyses are shown in Table 4.6. Only depth samples (> 1.6 m) were analyzed, knowing that the surface horizons are mainly composed of sand.

Table 4.6: Hand-touch analyses results to estimate the soil texture of depth soil horizons. Three soil textures are determined: sand, sandy clay (in italic) and clay (in bold).

Plot	**Depth [cm]**	**Texture**	**Plot**	**Depth [cm]**	**Texture**
1	200	**clay**	19	200	sand
2	200	**clay**	20	200	sand
3	200	sand	21	200	sand
4	200	sand	22	200	*sandy clay*
5	200	sand	23	200	sand
6	200	*sandy clay*	24	200	*sandy clay*
7	200	*sandy clay*	25	200	**clay**
8	200	**clay**	26	180	**clay**
9	200	*sandy clay*	27	180	**clay**
10	200	sand	28	180	*sandy clay*
11	200	**clay**	29	160	**clay**
12	180	**clay**	30	160	**clay**
13	200	sand	31	160	**clay**
14	180	*sandy clay*	32	160	**clay**
15	200	sand	33	160	*sandy clay*
16	200	sand	34	200	*sandy clay*
17	200	**clay**	35	180	**clay**
18	200	**clay**	36	200	*sandy clay*

Three types of textures are predicted using this method: sand, sandy clay and clay textures. These textures vary from one plot to another. We observe that plots located on the right side of our study area (plots 25-36) are characterized by sandy clay or clay textures in depth. Most of these plots have high dominant heights as discussed in Section 4.2. Moreover plots 1 and 2 are also characterized by clay textures in contrast to plots 3 and 4 which also have high dominant heights. Clay texture at approximately 2 m depth seem to be linked to a successful regeneration of cork oaks in contrast to sand texture. However, some plots (plots 8, 17, 18) have a predicted clay texture at 2 m depth although they have regeneration issues. This is discussed in the following section.

4.4.2 Laboratory analyses

Laboratory analyses results are depicted in Table 4.7, in Table 4.8 and in Appendix A.10. At UCL (Table 4.7), soil texture was determined for three soil profiles (plots 2, 7 and 11). pH_{H_2O} of all sixteen soil samples was also measured. At INRA (Table 4.8), soil texture was identified for thirteen soil profiles and the soil organic content of all thirteen surface soil samples was measured as well. Soil water content for all 36 soil profiles are indicated in Table A.1 (Appendix A.10).

Table 4.7: Laboratory analyses (pH_{H_2O} and soil texture) of soil profiles n° 2, 7 and 11 at UCL. Four soil textures are determined: fine sand, sandy loam (in blue), loamy fine sand (in green) and sandy clay loam (in red).

Plot	Depth [cm]	pH_{H_2O}	Clay [%]	Silt [%]	Sand [%]	Texture
2	0-20	6.12	2.90	1.91	95.20	fine sand
	40-60	6.51	2.69	0.98	96.34	fine sand
	100-120	6.57	1.73	1.08	97.19	fine sand
	160-180	6.73	1.45	2.52	96.03	fine sand
	180-200	6.66	1.95	2.10	95.95	fine sand
	200-220	6.32	15.11	3.43	81.56	sandy loam
7	0-20	6.09	3.30	2.45	94.25	fine sand
	20-40	6.38	2.62	2.40	94.98	fine sand
	100-120	6.37	1.81	2.06	96.13	fine sand
	140-160	6.20	1.56	2.07	96.37	fine sand
	180-200	6.28	5.65	3.92	90.43	fine sand
	200-220	6.24	7.12	4.94	87.94	loamy fine sand
11	0-40	6.10	3.15	3.37	93.48	fine sand
	120-140	6.46	2.76	2.59	94.65	fine sand
	180-200	6.75	7.54	5.37	87.09	loamy fine sand
	200-220	6.51	22.23	5.00	72.77	sandy clay loam

Regarding the samples analyzed at UCL (Table 4.7), pH_{H_2O} is more or less constant throughout the soil profiles. It varies only between 6.09 and 6.75, the soil is not very acidic. Regarding the samples analyzed at INRA (Table 4.8), the soil surface organic content is lower than 1 % in every sandy surface horizon except in plot 1 ($OM = 1.96$ %). According to Lepoutre (1965), the sandy layers of Maâmora soils contain very little humus and are grey coloured and carbon contents range between 0.3 % and 1.1 % (Lepoutre, 1965). The sandy layers of the soil increase the decomposition rate of organic matter as it is characterized by a high porosity and thus a high aeration of the soil. This way, it is expected to find low organic matter contents in these kinds of soils.

Generally, the surface soil horizons are mostly characterized by fine sand textures. Clay contents are very low and never exceed 5 %. Silt contents are quite low as well in the majority of these horizons but the percentages increase in some profiles. When summing up clay and silt contents of these profiles, we obtain high contents of fine elements (> 15 % for profiles 12, 25, 26, 29, 32 and 34). These surface horizons are therefore characterized as loamy fine sands. The presence of fine elements ($\varnothing < 50$ μm) may influence water retention. This assumption is tested in Section 4.6.1.

Below 1.40 m of depth, sand prevails with contents exceeding 85 %. However in deep soil horizons (2.0 m mainly), the clay contents increase in a significant way. Profiles 1, 2, 9, 11, 12, 25 and 26 have clay contents above 9 % (maximum of 22 %) at 2 m of depth. These soil horizons are hence characterized by sandy loam (or sandy clay loam) textures. Profiles 29 and 32 also have high clay contents but at lower depths. Profile 29 is characterized by 21 % of clays at 1.60 m and profile 32 by 16 % of clays at 1.60 m. Thus, the textural transition is shallower in these profiles. According to Lepoutre, the red clays of Maâmora have a clay content that can vary between 20 and 40 %, usually ranging between 25 and 30 %. In contrast, clay contents in a few profiles do not exceed 5 %, even at important depths. This is the case for plots 4, 16 and 19. Note that silt contents in depth for the profiles analyzed at INRA (Table 4.8) are quite high (>10 %) in comparison to those analyzed at UCL (Table 4.7) with contents below 5 %. This is certainly due to the methodology used at INRA for the sieve analysis. Indeed, the soil samples were not placed under ultrasounds to separate clays and silts from sands. As clay dispersion is complicated, we presume the clay contents in depth were underestimated in these analyses.

Soils of our study plot are hence composed of a sandy layer on top of a sandy-clay layer. The transition between the sand and clay layers can be abrupt (ex: plot 2) or progressive by means of a sandy-clay layer frequently ochre coloured and where traces of hydromorphy can be found (ex: ferruginous concretions). Sand types and clay structure are discussed in Sections 4.4.3 and 4.4.4 below.

Table 4.8: Laboratory analyses (organic matter content and soil texture) of thirteen soil profiles at INRA, Morocco. Four soil textures are determined: fine sand, sandy loam (in blue), loamy fine sand (in green) and sandy clay loam (in red).

Plot	Depth [cm]	OM [%]	Clay [%]	Silt [%]	Sand [%]	Texture
1	0-20	1.96	2.35	7.06	90.58	fine sand
	160-180		2.41	6.02	91.57	fine sand
	200-220		9.48	13.04	77.48	sandy loam
4	0-20	0.79	2.44	3.67	93.89	fine sand
	140-160		2.44	3.66	93.89	fine sand
	200-220		2.23	5.57	92.20	fine sand
9	0-20	0.98	2.22	9.98	87.80	fine sand
	60-100		2.18	9.80	88.02	fine sand
	200-220		9.69	14.53	75.78	sandy loam
12	0-20	0.91	2.34	12.86	84.81	loamy fine sand
	100-120		2.28	10.28	87.44	fine sand
	180-200		9.17	10.32	80.51	loamy fine sand
	200-220		18.08	6.05	75.86	sandy loam
14	0-40	0.33	2.43	3.65	93.92	fine sand
	100-120		2.52	1.26	96.22	fine sand
	180-200		4.69	14.08	81.22	loamy fine sand
16	0-40	0.90	2.48	3.73	93.79	fine sand
	140-160		2.41	3.62	93.97	fine sand
	200-220		2.38	9.52	88.10	fine sand
19	0-40	0.64	2.40	7.20	90.40	fine sand
	100-120		2.34	3.52	94.14	fine sand
	200-220		2.45	3.68	93.87	fine sand
22	0-40	0.75	2.47	6.18	91.35	fine sand
	120-140		2.36	9.43	88.21	fine sand
	200-220		7.52	10.02	82.46	loamy fine sand
25	0-40	0.63	4.59	13.76	81.65	loamy fine sand
	160-180		2.32	10.45	87.23	fine sand
	200-220		14.27	11.89	73.83	sandy loam
26	0-40	0.75	4.74	9.49	85.77	loamy fine sand
	160-180		9.36	10.53	80.11	loamy fine sand
	200-220		19.01	15.84	65.15	sandy loam
29	0-40	0.72	2.17	16.27	81.56	loamy fine sand
	140-160		11.63	15.12	73.24	sandy loam
	160-180		20.62	16.04	63.34	sandy clay loam
32	0-40	0.68	2.33	13.98	83.69	loamy fine sand
	80-100		2.32	10.45	87.23	fine sand
	160-180		15.75	20.25	64.00	sandy loam
34	0-20	0.97	2.28	17.13	80.58	loamy fine sand
	120-140		2.19	18.60	79.21	loamy fine sand
	180-220		6.71	15.67	77.62	loamy fine sand

4.4.3 Sand types

Figure 4.25 illustrates two soil profiles of our study area. The left profile corresponds to plot 19 and is composed of beige sands whereas the right profile corresponds to plot 34 and is composed of red sands.


(a) (b)

Figure 4.25: Comparison of sand types in two soil profiles. (a) Soil profile of plot 19 characterized by beige sands. (b) Soil profile of plot 34 characterized by red sands.

Three types of sands are found in Maâmora soils: beige-pink sands, red sands and white-grey sands. When all three types are found on the same profile, they overlap in the order presented. According to Lepoutre, beige-pink sands and white-grey sands are essentially siliceous and do not contain fine elements of a size lower than 20 μm. In contrast, red sands can contain up to 15 % - 18 % of fine elements such as clay (Lepoutre, 1967). In some soil profiles, hydromorphic traces are observable in the sands overlaying the clay layer: white and red spots, ferruginous concretions etc. This is observable on the picture shown in Figure 4.26.

Figure 4.26: Hydromorphic traces observable in a deep sandy horizon overlaying the clay layer.

As explained above, profiles 25, 26, 29, 32 and 34 have a loamy fine sand texture in surface and contain more than 15 % of fine elements in the first soil horizons (0-20 cm or 0-40 cm), they must therefore correspond to red sands and better retain water than beige sands which are characterized by a very high permeability. These sands are more recent than the red sands. The colour of the red sands is linked to the presence of iron oxides which are hydrated under important water regimes. The enrichment in clay in these sandy profiles is variable from one dendrometric plot to another and can lead to a localized successful regeneration of seedlings when the clay contents reach 10 %. This was confirmed by Lepoutre which observed this phenomenon in plots located in A canton (Lepoutre, 1965).

Thus, a certain clay content in the sandy layers of cork oak plots may influence the regeneration success of the species as it has better access to water for its roots to take up. Note that these sandy layers containing clay must be located at a certain proximity of the soil surface for the seedlings to grow (< 2 m). We see below if the presence of fine elements in the sandy surface horizons influence the permittivity measured by the GPR.

4.4.4 Clay horizons

Clay colour and structure varies from one soil profile to another. For example, plots 12 and 25 both have similar clay contents at a depth of 2 m. Plot 12 has 18 % of clay whereas plot 25 has 14 %. However, the clay observed in plot 12 was grey coloured and very moist (Fig. 4.27(a)) in contrast to the clay observed in plot 25 which was drier and ochre (Fig. 4.27(b)). In general, grey clays (plots 8, 11, 12, 17 and 18) were moist whereas red clays (plots 25, 26, 29, 33, and 35) were dry and friable. Moreover, the grey clays were observed in the western part of the study plot while the red clays were located in the eastern part.

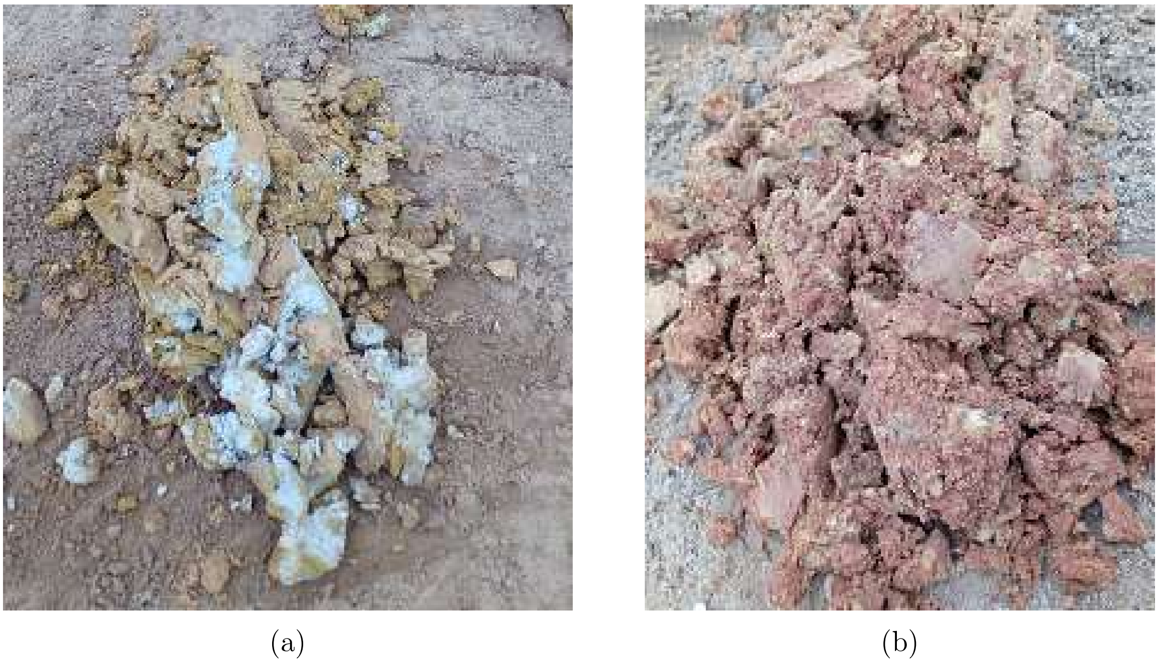
(a) (b)

Figure 4.27: Comparison of clay horizons (at 2 m deep) in two soil profiles. (a) Clay horizon of plot 12 composed of gley. (b) Clay horizon of plot 25 composed of red Maâmora clay.

The formation of red clays is due to rubefaction[1]. According to Lepoutre, rubefaction is a fossil character of Maâmora soils and it occurred when the red sands were deposited on top of the clay layer (Lepoutre, 1967). Additionally, sandy clay morphology is also fossil but hydromorphic characteristics may have superimposed under the effect of temporary perched water tables when the lateral drainage conditions were poor.

We assume that the grey-blue clays observed in our study area were subject to the effect of temporary perched water tables and were thus under temporary water-logging conditions. The formation of gley results from the presence of a perched water table which provokes anaerobic conditions and the reduction of iron. It is unfavorable to vegetation growth. When this water table disappears in summer, the soil is exposed to oxygen, and iron is oxidized. This is observable by red, yellow and orange spots in the upper soil horizons (as seen in Fig. 4.26). The formation of a perched water table on top of the clay horizon occurs in winter (high precipitations) in areas where the sand cover is not too thick and where the slope is not too important (Lepoutre, 1965). This is the case on our study area as the slope is almost nil and the concerned soil profiles have an estimated textural transition depth below 2.2 m (see Table 4.5). This water table can lead to adverse effects on young seedlings. As explained in Chapter 2, it can create anaerobic conditions and asphyxiate tree roots. This occurs when the perched water table is very shallow. Moreover, if the young roots stop growing at the water table level, during the next summer, the roots not having reached the clay layer will dry up. Unfortunately, we do not have

---

[1] reddening of rock or soil due to the deposition and oxidation of iron.

enough information to confirm this hypothesis but the concerned plots have lower heights and sometimes very low survival rates. For example, plot 17 has a mean height of 2.5 m and a survival rate of 9.1 %.

The red clays of Maâmora are essentially composed of kaolinites ($AlSi_2O_5(OH)_4$) (Lepoutre, 1965). Kaolinites have a low cation-exchange capacity and are charged negatively. Iron oxides are positively charged and are also found in these red clay horizons. Therefore, the opposite charges will be attracted and this will form micro-aggregations (Chauvel, 1976). Water will infiltrate throughout the macropores whereas it will be retained in the micro-aggregates and adsorbed by very fine pores (Delvaux, 2018). A better water retention in these types of clay provide water for tree roots to take up. As these types of clay are observed in plots 25, 26, 29, 33, 35 etc, these well drained soils may explain the better regeneration success of cork oaks.

All these findings are only based on field observations and on sand, silt and clay contents measured in the laboratory. Obviously, we do not have sufficient information to draw conclusions on the types of sands and clay structures of our different soil profiles. It would have been necessary to carry out far more soil analyses to define additional soil properties such as the iron oxide contents, the pH_{H_20} and pH_{KCl}, the available water capacity in the sandy and clay horizons, apparent density, etc. But this was not the main aim of the study. Therefore, the following analyses will only be based on soil textures.

4.5 Tree growth and soil surface moisture

In Section 4.3.1, we observed on the map of our study area that the mean dielectric permittivity seemed to be higher in areas where trees were bigger and in better shape. To verify this assumption, we compared tree growth (dominant height) and the mean dielectric permittivity estimated per plot (see Table 4.4).

Figure 4.28 shows the dominant height per plot as a function of the mean dielectric permittivity per plot. Plots 1 and 8 are not included considering that no GPR data points crossed these plots. Moreover, plots 4, 10, 15, 22, 27 and 34 are not included either because, as said previously, the first transect may be subject to significant errors.

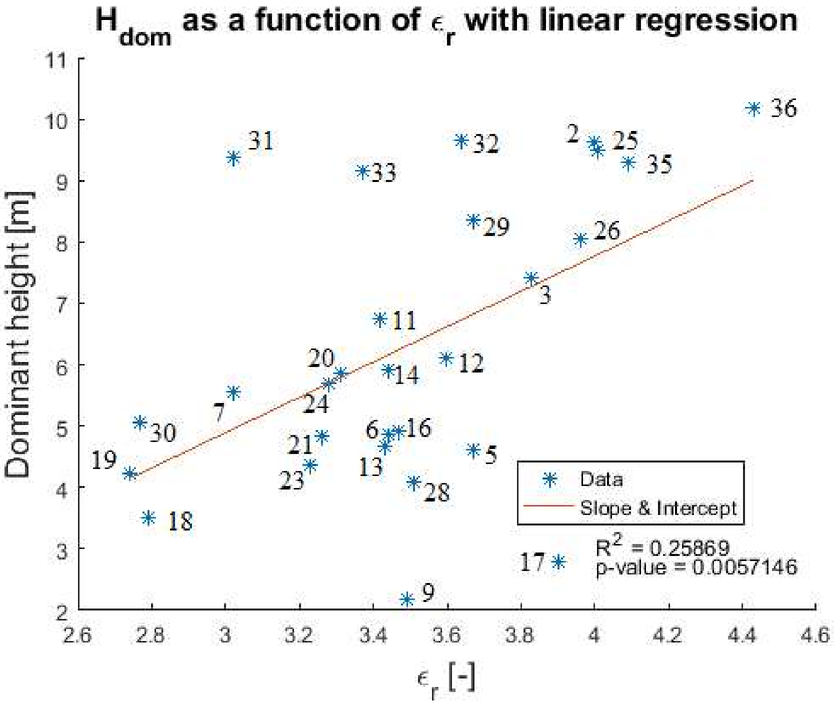

Figure 4.28: Dominant height (H_{dom}) as a function of the mean relative dielectric permittivity (ε_r) with linear regression. Data points (*) are marked by their respective plot number.

We observe a positive correlation between both variables. Plots characterized by a higher permittivity have a higher dominant height as well. This is the case for plots 2, 25, 26, 35 and 36: dominant height is above 8 m and permittivity is higher than 4 for all five plots. In contrast, other plots are characterized by low dominant heights. This may be linked to their low permittivity. Plots 18, 19 and 30 have lower permittivities ($\varepsilon_r < 2.8$). Their low dominant height may be due to poor soil water retention which prevents tree roots to take up water. Nevertheless, plot 31 has a high dominant height ($H_{dom} = 9.4$ m) but its mean permittivity is low ($\varepsilon_r = 3.02$) whereas plot 17 has a high permittivity ($\epsilon_r = 3.9$) but a low dominant height ($H_{dom} = 2.8$ m).

4.6 Soil surface moisture and soil texture

4.6.1 Surface sandy horizons

To test our assumption on the impact of sand types (beige and red sands) on water retention (see Section 4.4.3), we compared the mean dielectric permittivity and the clay content in the first sandy horizon.

Figure 4.29 shows the mean dielectric permittivity per plot as a function of the clay content in the first surface horizons (0-20 cm or 0-40 cm deep). As the number of soil texture analyses was limited and as we did not have values of ε_r for plots 1, 4, 22 and 34, twelve soil profiles were plotted in this graph.

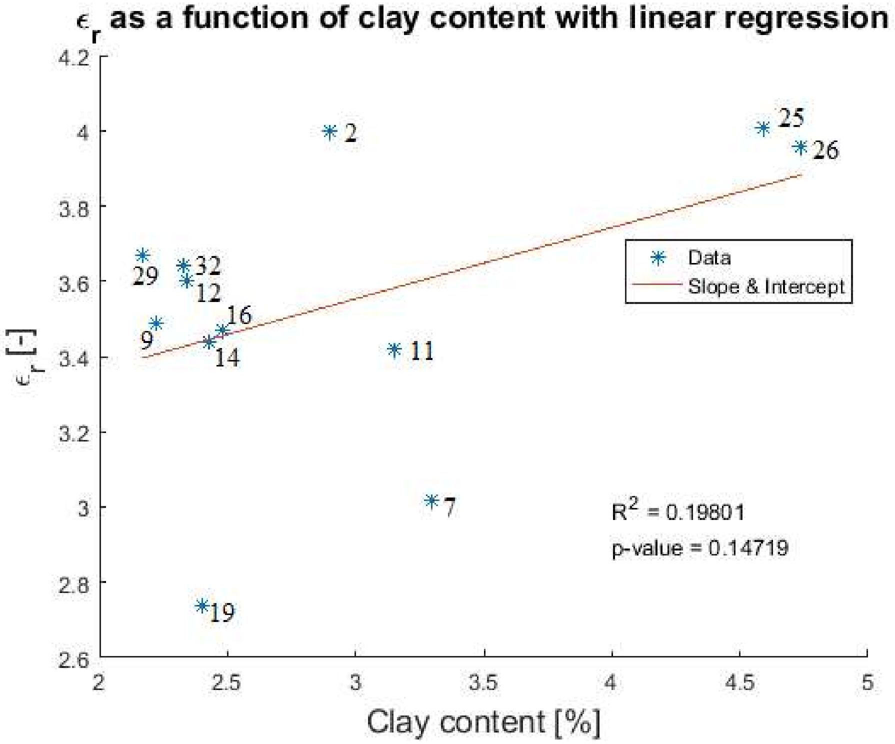

Figure 4.29: Mean relative dielectric permittivity (ε_r) as a function of the clay content in the soil surface layer with linear regression. Data points (*) are marked by their respective plot number.

Most of the plots have low clay contents (< 2.5 %) in surface horizons as the first soil layer is mainly composed of sand. For plots 9, 12, 14, 16, 29 and 32, ε_r ranges between 3.4 and 3.7 and they have relatively low clay contents. However, it is clear that plots 25 and 26 are more moist in surface and hence have a higher ε_r. This may be explained by the higher clay contents which reach almost 5 %. In contrast plot 19 has a lower permittivity ($\varepsilon_r = 2.7$) and a lower clay content in the surface layer.

As reported in Section 4.4.2, silt contents are quite high in some surface samples; thus, the sand content is lower. Figure 4.30 shows the mean dielectric permittivity per plot as a function of the clay and silt contents in the first surface horizons.

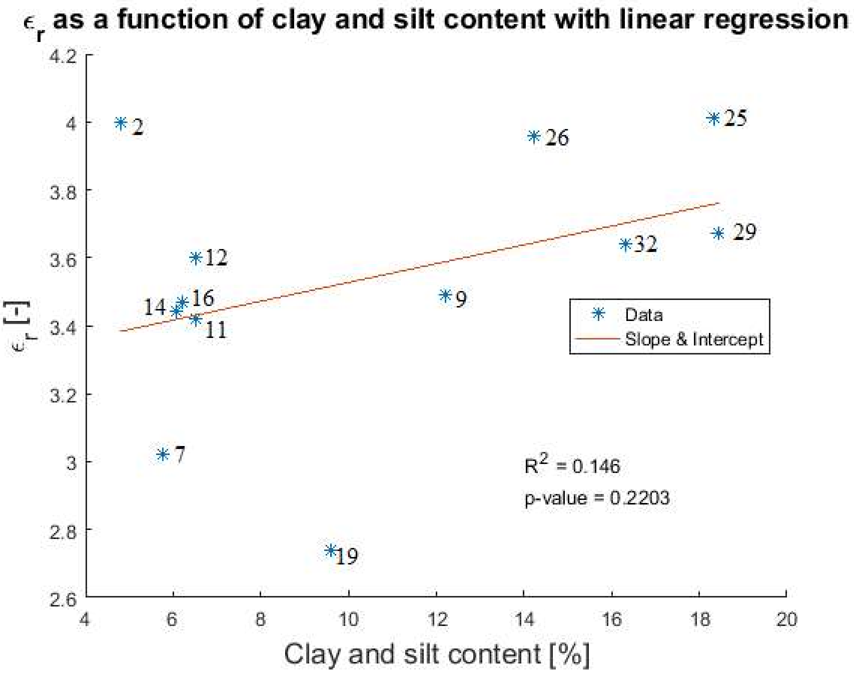

Figure 4.30: Mean relative dielectric permittivity (ε_r) as a function of the clay and silt content in the soil surface layer with linear regression. Data points (*) are marked by their respective plot number.

By adding the silt contents to the clay contents, the general appearance of the graph changes (in contrast to Fig. 4.29). In fact, plots 29 and 32 which are characterized by high silt contents (respectively, 16.3 % and 14.0 %) are now on the upper right side of the graph and join plots 25 and 26 which have high clay and silt contents as well as a high permittivity. As fine elements retain water better than coarse elements such as sand, water retention in these surface horizons may explain their higher permittivities.

In spite of these observations, we can not say with certainty that the surface texture influences the permittivity as the correlation between both variables is not significant (p-value > 0.05), as in the previous graph. For example, plot 2 has low clay and silt contents but a high permittivity whereas plot 19 has a more or less high clay and silt content but a relatively low permittivity.

4.6.2 Deep clay horizons

We also compared the mean dielectric permittivity and the clay content in the deeper horizons. Figure 4.31 shows the mean relative dielectric permittivity per plot as a function of the clay content in depth (≈ 2 m).

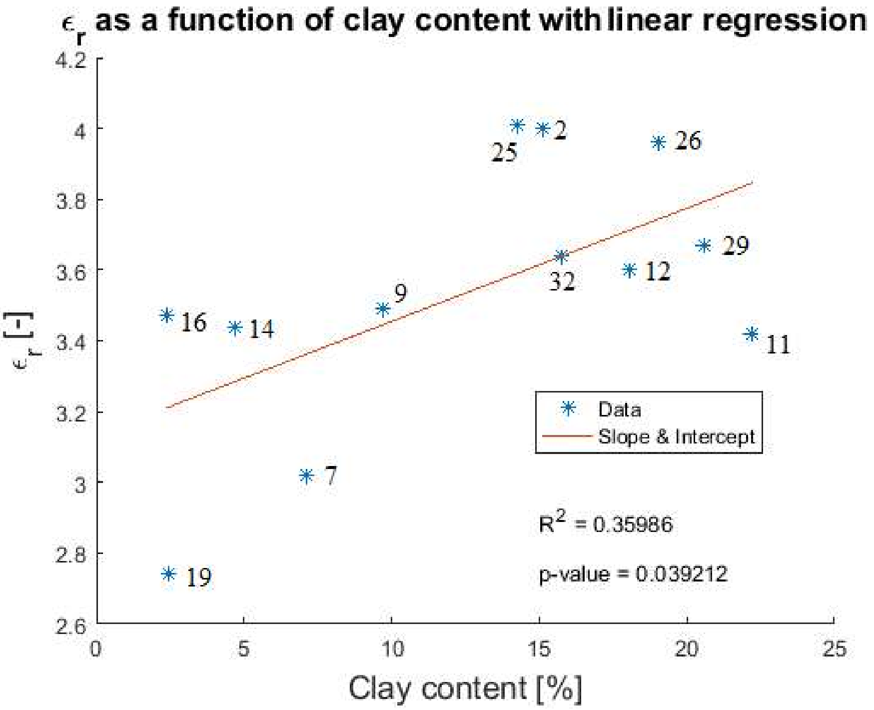

Figure 4.31: Mean relative dielectric permittivity (ε_r) as a function of the clay content at a depth of about 2 m with linear regression. Data points (*) are marked by their respective plot number.

We observe a positive correlation between both variables. The permittivity increases when the clay content measured in depth increases. When the clay content at 2 m deep is higher, the clay layer must be shallower than in profiles where the clay content is lower at the same depth. Plots 26 and 29 have relatively high clay contents beyond 1.5 m of depth ($>$ 18 %). Moreover, plot 26 has a successful tree growth characterized by high trees as discussed above. When a soil is humid (wet season), the surface horizons provide more water to the shallow tree roots than deep horizons. When the soil starts to dry up (dry season), water extraction by tree roots will gradually occur deeper and deeper as less water is retained in the soil profile. In summer, only the deep tap roots will take up water. Hence, water uptake by tree roots occurs in different soil horizons according to the season. As clays retain water more efficiently than sands which drain water more rapidly, these plots must have better water retention. Soil surface moisture depends on what lies underneath the sandy layer and the higher clay contents at 2 m deep may explain the higher permittivities.

In contrast, clay contents in depth are very low for plot 19. This profile has a fine sand texture. Hence, the soil profile must be very dry and water retention is poor as soil horizons are mainly composed of sand. This plot is also characterized by a low dominant height as pointed out in the previous section.

Again, as we assumed that the clay content was underestimated, we summed up the clay and silt contents in depth. Figure 4.32 shows the mean relative dielectric permittivity per plot as a function of the clay and silt content in depth.

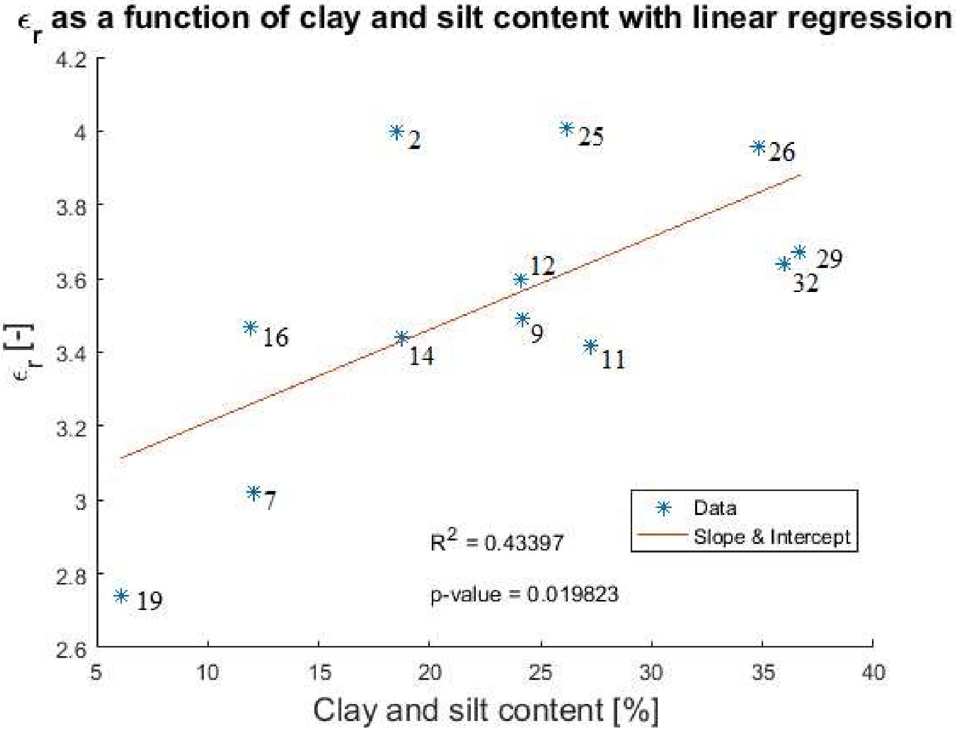

Figure 4.32: Mean relative dielectric permittivity (ε_r) as a function of the clay and silt content at a depth of about 2 m with linear regression. Data points (*) are marked by their respective plot number.

The general appearance of the graph is similar to the previous one. The correlation is a bit better using these values: in Figure 4.31, $R^2 = 0.36$ (p-value = 0.04) whereas in Figure 4.32, $R^2 = 0.43$ (p-value = 0.02). The same observations described previously are applicable to this graph as well.

One may wonder if the high permittivities are due to the presence of trees which provide shade and thus reduce evaporation of water. However, the correlation between permittivity and clay and silt contents indicate that soil textures influence water retention. For example, plot 9 has a more or less high ε_r and a high clay and silt content in depth whereas it is the most exposed plot to evaporation as it has the lowest survival rate ($<$ 10%). Evaporation occurs on the first few mm but the permittivity is measured on the first 10 cm -15 cm of the soil profile (as explained in Section 4.3.1). Hence, the higher values of permittivity may explain better tree growth as explained above.

In general, in addition to the measured permittivity, it would have been interesting to calculate the available water capacity[2](θ_a) of our soil profiles. It equals to the difference between the water content at field capacity (θ_{fc}) and at the permanent wilting point (θ_{pwp}). In the future, it would be interesting to model the water retention curve using pedotransfer functions to estimate hydraulic properties. In that case, measuring the bulk density would provide valuable information in addition to texture. With such information, we could strengthen our assumptions.

4.7 Tree growth and soil texture

As dominant height has a positive correlation with relative permittivity (Fig. 4.28) and relative permittivity has also a positive correlation with clay content in depth (Fig. 4.31), we assumed that the dominant height would be correlated to clay content in depth as well. This is illustrated in Figure 4.33 which shows the dominant height per plot as a function of the clay content in depth (≈ 2 m). The same twelve plots than in Figure 4.31 are presented in the following graph.

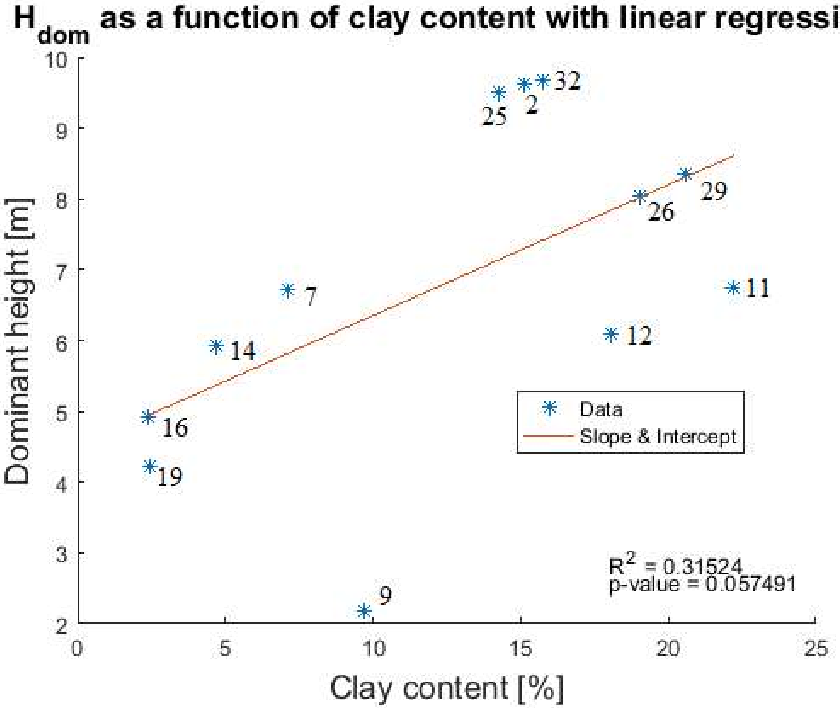

Figure 4.33: Dominant height (H_{dom}) as a function of the clay content at a depth of about 2 m with linear regression. Data points (*) are marked by their respective plot number.

As expected, a positive correlation is observed between both variables. For example, plots 26 and 29 are characterized by high dominant heights and high clay contents in depth.

---

[2] available water that can be stored in soil and that is available for plants to take up.

In contrast, plots 16 and 19 have lower dominant heights which might be explained by the low clay contents in depth. As explained above, when the clay content at 2 m deep is higher, the clay layer must be shallower than in profiles where the clay content is lower at the same depth. Hence, we assume that the clayey layer is shallower in plots 26 and 29 than in plots 16 and 19. The radar images of 2015 confirm our assumption. In fact, the textural transition depth estimated for plot 19 equals to 4.2 m whereas the estimated textural transition depth for plot 29 equals to 1.8 m (see Section 4.3.2).

Finally, plot 9 draws our attention. In fact, although it is characterized by a more or less high clay content in depth (9.7 %), it has the lowest dominant height of all dendrometric plots (2.17 m). It also has the lowest survival rate (5.56 %). We assume that this dendrometric plot was cut down by local inhabitants. In fact, the remains of a wood fire were observable right by the concerned plot. This outlier therefore skews the distribution of the results presented in Figure 4.33.

As we had more information regarding the clay contents for additional plots (plots 1, 4, 22 and 34), we drew the same graph but with the four additional plots (total of sixteen plots). This is illustrated in Figure 4.34.

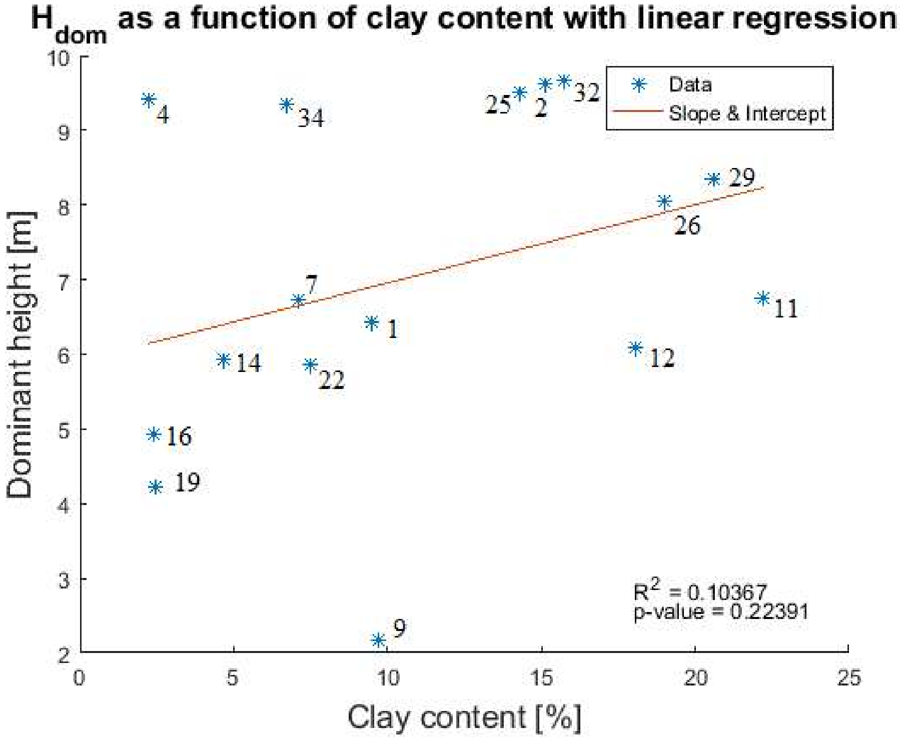

Figure 4.34: Dominant height (H_{dom}) as a function of the clay content at a depth of about 2 m with linear regression. Data points (*) are marked by their respective plot number.

By adding information, we observe a weaker correlation between both variables. This is due to the addition of plots 4 and 34. Plot 4 is characterized by a very high dominant height (9.4 m), it is indeed one of the highest of our study area. However, its clay content in depth is very low with less than 2.2 %. Plot 34 is also characterized by a high dominant height, it has a bit more clay at 2 m deep than plot 4 (6.7 %) but twice less than plots 2, 26, 29, 32, etc.

Because the clay content at 2 m deep of plot 4 is low (2.2 %), we assume that the clay layer must be deeper. However, because it has a high dominant height, we presume that it must not be too far from 2 m of depth. In fact, we observed in the previous section that when the clay layer is too deep (ex: plot 19 which has an estimated textural transition depth of 4.2 m), tree growth is difficult. This plot must therefore be characterized by a brutal textural transition as in plot 2. This plot has indeed a clay content of only 2 % at 1.80 m deep whereas it increases up to 15 % at 2 m deep. To verify this assumption, we should have had a longer auger to find out at which depth appears the clay layer in this soil profile.

4.8 Clay layer depth

In Section 4.7, we discussed the correlation between dominant height and clay content in depth and we assumed that when the clay content at 2 m deep is higher, the clay layer must be shallower. This assumption is tested in the following graph shown below (Figure 4.35).

This graph shows the textural transition depth estimated per plot using the 2015 radar images as a function of the clay content in depth per plot ($\approx$ 2 m). For each plot crossed by one of the two transects, the depth of the textural transition measured by the radar was plotted in the vertical axis. As we did not carry out soil analyses on all soil profiles, a total of six profiles were plotted on this graph.

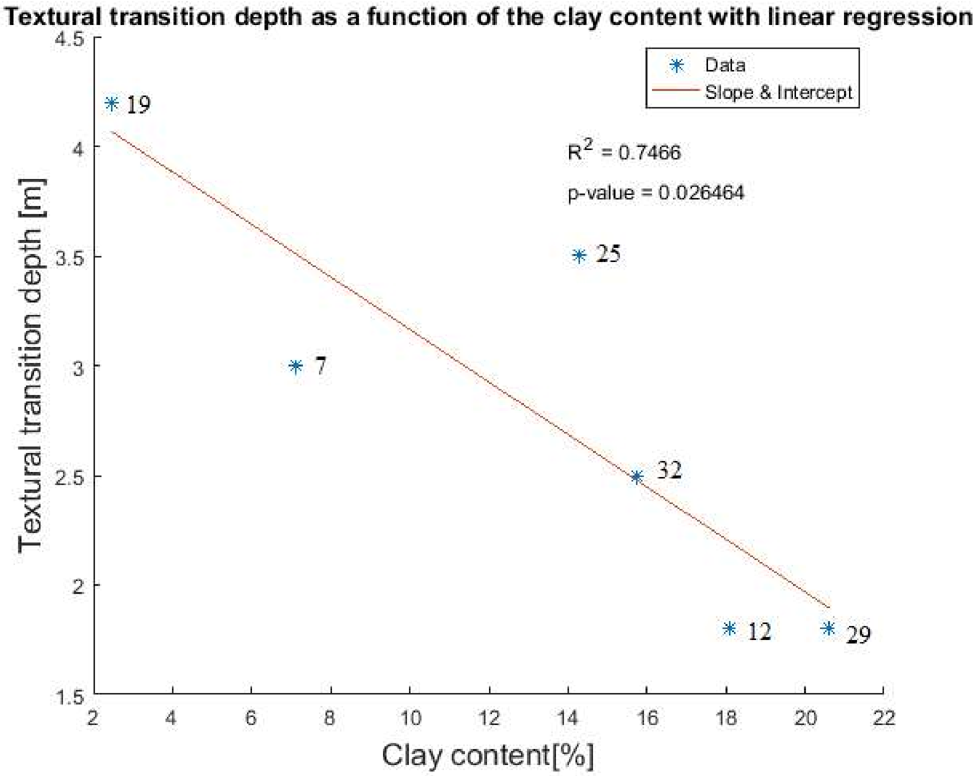

Figure 4.35: Textural transition depth as a function of the clay content at a depth of about 2 m with linear regression. Data points (*) are marked by their respective plot number.

As the textural transition depth decreases, the clay content in depth increases. Plots 12 and 29 have both high clay contents in depth (18 % and 21 %). The radar image confirms that there is a textural transition at approximately the same depth (1.8 m). When the clay content at 2 m deep decreases down to 2 % (plot 19), the textural transition depth measured by the radar is much deeper (4.2 m). The low clay content indicates that the sand layer is thicker in this profile than in plots 12 and 29. The correlation between these variables confirms the compliance of the 2015 radar data with our soil laboratory results and enables us to utilize the approximated textural transition depths in further analyses including the one below.

As said above, we observed a correlation between dominant height and clay content in depth (Figure 4.34). As the clay content in depth is also correlated to the textural transition depth (see Figure 4.35), we expect that the textural transition depth must indeed have an impact on tree growth.

Figure 4.36 shows the dominant height per plot as a function of the estimated textural transition depth. The same plots than in Figure 4.35 are drawn on this graph.

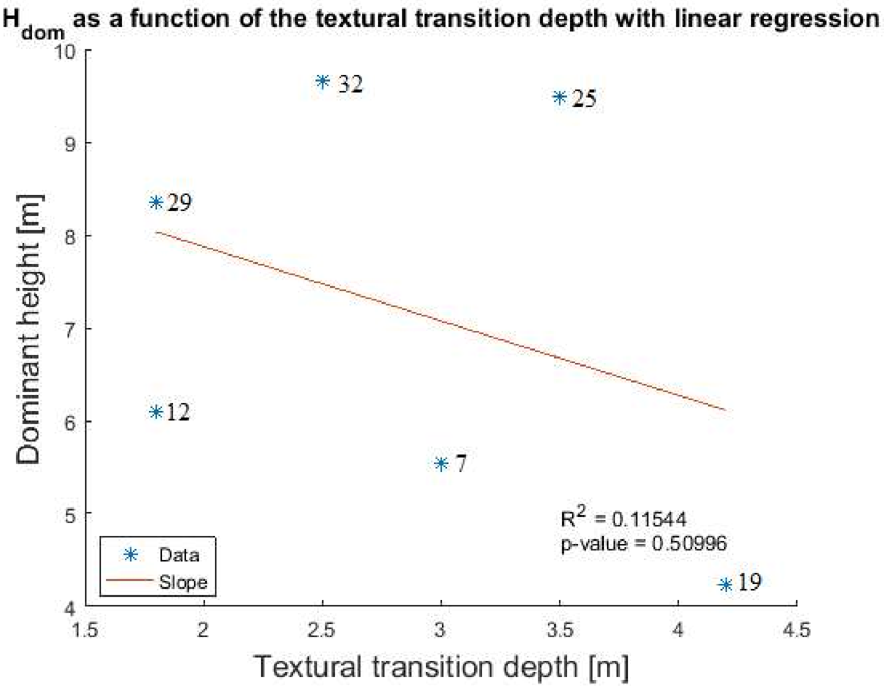

Figure 4.36: Dominant height (H_{dom}) as a function of the textural transition depth with linear regression. Data points (*) are marked by their respective plot number.

No correlation is observable between these two variables. We assumed that the dominant height would increase when the textural transition depth decreased as many studies have proven that cork oaks have a more successful regeneration when the clay layer is shallower than two meters (see Chapter 2). Although plot 12 has an estimated textural transition depth of 1.8 meters, its dominant height (H_{dom} = 6.1 m) is lower than most successful plots which have dominant heights above 9 meters. In contrasts, plot 25 which has the fourth best dominant height (H_{dom} = 9.5 m) is characterized by a deeper textural transition depth (D = 3.5 m).

Plot 12 and 29 both have the same estimated textural transition depths (1.8 m) but more than 2.5 m of difference in terms of dominant height. Hence, the textural transition depth must not be the factor that determines a better tree growth in this case. To detect this factor, we compared both plots. They both have a similar permittivity (3.6 and 3.67 for plot 12 and 29, respectively) and similar textures (surface clay contents : 2.34 % and 2.17 % and depth clay contents : 18.08 and 20.62 %). However, the clay structure is different. As shown in Figure 4.27(a), the moist clay contained in profile 12 is composed of gley and is grey coloured in contrast to the the dry red clay in profile 29 which is similar to the one presented in profile 25 (see Section 4.4.4). Hence, plot 29 must be characterized by a better water drainage throughout the soil profile than plot 12 which explains this difference in terms of tree growth.

As we had more information regarding the textural transition depths for additional plots (see Table 4.5), we plotted a new graph showing the dominant height as a function of the textural transition depth. This is illustrated below in Figure 4.37.

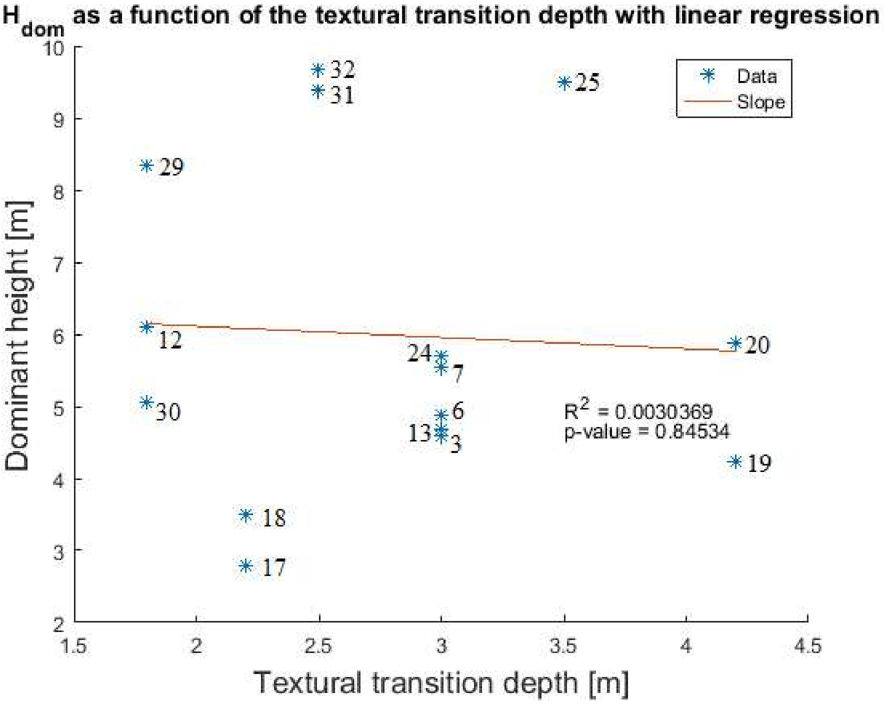

Figure 4.37: Dominant height (H_{dom}) as a function of the textural transition depth with linear regression. Data points (*) are marked by their respective plot number.

Once again, no correlation is observable: the data points are scattered. Plots 17 and 18 have dominant heights below 3.5 meters although the textural transition depth is estimated at 2.2 meters deep. In contrast, plot 31 and 32 have much higher dominant heights while the estimated depth indicates 2.5 m. This graph makes us think that the clay layer depth must not be the only factor that influences cork oak growth as explained above.

Unfortunately, soil texture was not determined for profiles 17 and 18. However, using the hand-touch method described previously, we were able to detect clay at 2 m depth in both soil profiles (see Table 4.6). These clays resembles the clay of profile 12: grey coloured with hydromorphic traces on top of the clay layer. Once again, a poor water drainage in these soil profiles may explain their low dominants heights.

Finally, as mean dielectric permittivity showed a positive correlation with the clay content in depth (see Figure 4.31) and as clay content in depth showed a correlation with the estimated textural transition depth (see Figure 4.35) we compared the permittivity and the textural transition depth at the scale of the study area.

Figure 4.38 shows the relative dielectric permittivity as a function of the textural transition depth. Textural transition depth was estimated every 20 m - 25 m along both transects and combined with the corresponding permittivity data points. This way, 57 points were plotted in Figure 4.38.

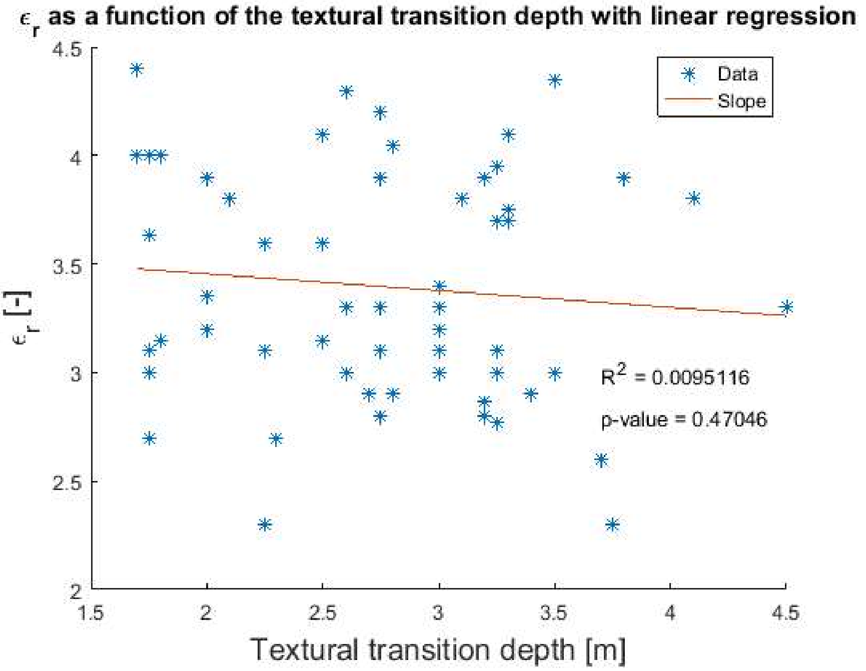

Figure 4.38: Relative dielectric (ε_r) permittivity as a function of the textural transition depth with linear regression

The data points are scattered, there is no correlation between both variables. We initially believed that there must exist a correlation between these variables. In fact, if the textural transition is shallower, more water is retained near the soil surface and the permittivity must be higher. According to this graph, our assumption can not be confirmed. Hence, this proves that the clay layer depth is not the only factor that contributes to soil moisture. Other factors such as soil texture must also intervene.

4.9 Summary

Throughout this chapter, we have presented numerous results regarding the regeneration success of cork oak plots of our study area and the soil properties that may be linked to it. This last section briefly recaps the main findings of our study.

Our study plot can be roughly divided into three areas in terms of successful regeneration (see Fig. 4.15): (i) the upper left corner comprising plots 1, 2, 3 and 4, (ii) the right side comprising plots 25, 26 and 31 to 36, and (iii) the 24 remaining dendrometric plots located in the middle. Areas (i) and (ii) are both successful in terms of cork oak growth:

the 12 plots have high dominant heights and high survival rates. Both areas have similar properties: they have higher permittivities and the clay contents increase in depth from 1.8 m up to 3.5 m. At 2 m of depth, clay contents are around 15-20 %. However, the right side area (ii) is supposedly composed of red sands and red Maâmora clays whereas the upper left corner (i) is composed of beige sands and hydromorphic traces are found on top of the clay layer.

The clay layer depth does not seem to be the key factor responsible of cork oak regeneration success on our study area. In fact successful regeneration plots have estimated clay layer depths comprised between 1.8 m (plot 29) and 3.5 m deep (plot 25). However, when this estimated depth exceeds 4 m deep, low dominant heights and survival issues were observed (plot 19). Certainly, it plays an important role but other factors must also be taken into account.

Sand types seem to influence the water retention in the surface soil horizons. In fact, when the content of fine elements increases (red sands in contrast to beige sands), the permittivity is higher. This is the case for the plots located in area (ii) (plots 25, 26, 29, 32). Nevertheless, we can not confirm this assumption as the correlation is not statistically significant enough (ex: plot 2 in area (i)). I would suggest to carry out further analyses to study the impact of these different sand types.

Moreover, we observed that clay structure may also influence the permeability of the clay horizon. We discussed the possible impact of a perched water table and the resultant poor water drainage in the soil profile (plot 17) in contrast to the red Maâmora clays which provide better drainage and better water retention (plot 29). Again, we did not have enough results to confirm this hypothesis so I would suggest to deepen this topic as it is most certainly a key factor for tree roots water uptake.

In relation to that, it would be interesting to study the root system of cork oaks in the different soil profiles to better understand where the roots take up water and if they are capable of sinking into the clay layer or if they remain in the superficial layers of clay horizons. In addition, I would suggest to measure the soil water capacity.

Conclusion and future outlook

The overall aim of this thesis was to study the relationship between cork oak growth and soil factors using GPR techniques. To reach this aim, two sub-objectives were defined:

1. The set up of a new lightweight frequency domain ground-penetrating radar (GPR);
2. The research of soil factors that lead to successful regeneration of cork oaks.

To reach the first specific objective, several steps were necessary. The first step consisted of calibrating the horn dipole antenna to filter out the antenna effects of the radar images. Three transfer functions resulting from the antenna calibration were hence identified and the complex return loss transfer function (H_i) provided information on the low frequencies where the antenna is efficient. Then, laboratory tests on top of a sandbox allowed us to define the best antenna height to carry measurements and also proved that the new radar system worked correctly in similar conditions to those expected in the Maâmora forest (i.e., dry sands). Numerical simulations were also carried out and provided more information on the maximum sandy soil depths where the GPR is effective. Finally, field tests helped ensure the complete functioning of our new lightweight GPR system (and associated GPS).

The second specific objective was achieved by analyzing numerous field measurements. First, dendrometric measurements related to cork oak growth confirmed our observations on the high variability that prevails in our study area. Then, using our lightweight frequency domain GPR, relative dielectric permittivity was measured and hence, we were able to map the soil surface moisture of the study area. Using past historic time domain GPR data, we were also able to detect at which depths the textural transitions between sandy and clay layers occur which are specific to the Maâmora soil profiles. Finally, soil surveys down to 2 meters deep provided information on the sandy and clayey layers through laboratory analyses.

The soil moisture map of our study area was a first indicator of successful cork oak regeneration. In fact, we linked the measured permittivity to the dominant heights of cork oaks and observed that the most successful plots were characterized by higher permittivities. These higher values were mostly explained by the soil texture as we observed that permittivities increased as the clay content increased as well. Hence, this proves that soil texture influences the success of cork oak growth. Moreover, sieve analyses confirmed that the high clay contents at approximately 2 m deep positively influenced cork oak growth as well. Hence when the clay layer is shallower, the trees grow better. Using the previous historic time domain radar images, we soon realized that clay layer depth was not the only factor that is responsible of cork oak regeneration success as we did not observe any positive correlation between dominant height and textural transition depth. We observed that the most successful plots had a clay layer depth comprised between 1.8 m and 3.5 m. In contrast, beyond 4 m, the trees had more difficulties to grow.

Both radar systems provided information on soil properties and allowed us to analyze their impact on cork oak growth. These properties are soil moisture and textural transition depth. When soils are more moist, this means that soil water retention is better than in dry soils. This water retention is an important factor that allows tree roots to take up water and nutrients throughout the soil profile. The clay layer depth must also be taken into account as the root system must reach the clay layer in order to extract water when the soil profile is completely dry. We also discussed the possible influence of sand types on water retention and on the permeability of different soil profiles. Moreover, clay structures must also impact the permeability. I would suggest to deepen these topics to confirm these assumptions.

Thus, throughout this study, we were able to detect soil factors that influence cork oak regeneration using a near-surface remote sensing tool which is GPR. Obviously, further soil analyses would allow us to fully understand the soil water hydrodynamics. In addition, studying the root system of the cork oak would also elucidate where and how water is extracted from the different soil horizons. Of course, we were not able to unravel all the factors that can contribute to successful cork oak regeneration but GPR provided us very valuable information. Using GPR for future cork oak plantings would allow the forester to detect the best areas where trees shall be planted in order to have a successful regeneration.

Moreover, only edaphic factors were addressed in this research study at the field scale but it is clear that climate plays a vital role for cork oak growth at the forest scale. A decreasing rainfall gradient from West to East is observable and is likely to amplify in the future. Climate change should hence also be taken into account in the future regeneration of cork oaks plots of Maâmora. In addition, we mentioned the impact of local inhabitants on the cork oak growth. Let us not forget that, even though their actions are sensible in that socio-economical context, it pressures the forest and an appropriate balance must be found between different interests.

Before closing this chapter, I would like to add that this master thesis was not only a scientific research study but also a human experience. My journey to Morocco allowed me to discover a new culture rich in tradition and meet great people. I will always remember the warm hospitality and friendly assistance of Moroccans.

Bibliography

[1] Ardekani, M.R.M. and Lambot, S. (2014). *Full-wave calibration of time- and frequency-domain ground-penetrating radar in far-field conditions.* IEEE Transaction on geoscience and remote sensing, Vol.52(1). pp 664-678.

[2] Aronson, J., Pereira, J.S. and Pausas, J.G. (2009). *Cork Oak Woodlands on the Edge: Ecology, Adaptive management, and Restoration.* Society for Ecological Restoration International. 352 pages.

[3] Artiguesm R. and Lepoutre, B. (1969). *Influences du sol et de la densité du peuplement sur la faculté de rejeter du chêne-liège en forêt de la Mamora.* Annales de la recherche forestière au Maroc, Tome 10, rapport 1966-1967. pp 5-22.

[4] Bagaram, B.M., Mounir, F., Lahssini S. and Ponette, Q. (2016). *Site suitability analysis for cork oak regeneration using GIS based multicriteria evaluation techniques in Maamora forest-Morocco.* Open Access Library Journal, Vol.3: e2483.

[5] Bagaram, B.M. (2014) *Elaboration d'une base de données géographiques et catalogue des stations de la subéraie de la Maamora.* Mémoire online, Ecole Nationale Forestière d'Ingénieurs, Salé (Maroc).

[6] Belghazi, B., Badouzi, M., Belghazi, T. and Moujjani, S. (2011). *Semis et plantations dans la forêt de chêne-liège de la Maâmora, Maroc.* Forêt méditerranéenne, Tome 32, Vol. 3. pp 301-314.

[7] Billaux, P. and Bryssine, G. (1966). *Les sols du Maroc.* Les cahiers de la recherche agronomique, Vol.24, Tome 1, Première partie, Chap. III. pp 59-101.

[8] Chauvel, A., Pedro, G., Tessier, D. (1976). *Rôle du fer dans l'organisation des matériaux kaoliniques. Etudes expérimentales.* Bulletin de l'association française du sol. Edité par l'Association Française pour l'Etude du Sol, VERSAILLES. pp 102-114.

[9] Climat: Maroc, Salé. `https://fr.climate-data.org/country/181/#example4` viewed on 14/05/2018.

[10] Cordonnier T., Tran-ha, M., Piat, J. and François, D. (2007). *La surface terrière: méthodes de mesure et intérêts.* RDV techniques n^{o}18 - automne 2007 - ONF. pp 9-16.

[11] de Beaucorps, G., Marion, J. and Sauvage, Ch. (1956). *Essai monographique sur une parcelle d'expériences dans la forêt de chêne-liège de la Mamora (Maroc).* Annales de la recherche forestière au Maroc, Rapport annuel, Tome 4, Fascicule 2. Rabat: Editions Techniques Nord-Africaines. 262 pages.

[12] de Potter, B. (2011). *La surface terrière des peuplements: mesures et aspects pratiques.* Forêt wallonne n^{o}111 mars/avril 2011. pp 10-15.

[13] Daniels, D.J. (2004). *Ground-penetrating radar.* 2nd edition. 752 pages.

[14] Delvaux, B. (2018). *Gestion et aménagement des sols en régions chaudes.* LBRES2203, UCL.

[15] Duchaufour, P. (1992). *Pédologie: sol, végétation, environnement.* 4^e ed, 1995, Masson, Paris (France).

[16] El Alami Idrissi, N. (2013). *La faune de la litière de la suberaie de la Mâamora.* Rev. Mar. Sci. Agron. Vét., Rabat (2013). pp 50-57.

[17] El Boukhari, E.M., Brhadda, N. and Gmira, N. (2015). *Bilan actualisé et facteurs impliqués dans le succès des reboisements du chêne-liège (Quercus suber L.) dans la forêt de la Maâmora, Maroc.* Geo-Eco-Trop, Vol. 38(2). pp 325-338.

[18] El Boukhari, E.M., Brhadda, N. and Gmira, N. (2015). *Contribution à l'étude de la régénération artificielle du chêne-liège (Quercus suber L.) vis-à-vis du contenu minéral des feuilles et des paramètres physico-chimiques des sols de la Maâmora, Maroc.* Nature et Technologie, Vol. 14. pp 26-39.

[19] El Boukhari, E.M., Gmira, N. and Brhadda, N. (2013). *Effet des traitements physiques sur la croissance et le développement des semis de glands de chêne-liège (Quercus suber L.) en pépinière forestière au Maroc.* Geo-Eco-Trop, Vol.37(2). pp 177-190.

[20] Environmental Systems Research Institute (ESRI). (2016). *How Kriging works.* ArcMap 10.3. `http://desktop.arcgis.com/en/arcmap/10.3/tools/3d-analyst-toolbox/how-kriging-works.htm#ESRI_SECTION1_E112B7FAED26453D8DA4B9AEC3E4E9BF` viewed on 27/07/2018.

[21] Faraj, H. (1963). *Etude pédologique des sols de la Maamora.* INRA, Rabat. 110 pages.

[22] Fennane, M. and Rejdali, M. (2015). *The world largest cork oak Maamora forest: challenges and the way ahead.* Flora Mediterranea 25 (Special issue). pp 277-285.

[23] Food and Agriculture Organization of the United Nations (2016). *State of the world's forests, Forests and agriculture: land-use challenges and opportunities.* Rome. 126 pages

[24] Food and Agriculture Organization of the United Nations (2016). *Forests and the forestry sector, Morocco.* `http://www.fao.org/forestry/country/57478/en/mar/` viewed on 03/04/2018.

[25] Food and Agricultural Organization of the United Nations (2001). *Lecture notes on the major soils of the world.* World Soil Resources reports, edited by Driessen, P., Deckers J., Spaargaren O. and Nachtergaele F., Rome, 2001. pp 265-270.

[26] FAO, IIASA,ISRIC, ISS-CAS and JRC. (2009). *Harmonized World Soil Database (version 1.1).* FAO, Rome, Italy and IIASA, Laxenburg, Austria. `http://www.fao.org/soils-portal/soil-survey/cartes-historiques-et-bases-de-donnees-des-sols/base-harmonisee-mondiale-de-donnees-sur-les-sols-version-12/fr/` viewed on 15/04/2018.

[27] Gil, L. and Varela, M.C. (2008). *EUFORGEN Technical Guidelines for genetic conservation and use for cork oak (Quercus suber).* Biodiversity International, Rome (Italy). 6 pages.

[28] Haut Commissariat aux Eaux et Forêts et à la Lutte contre la Désertification (Royaume du Maroc). (Avril 2015). *Caractérisation des agents et causes de la déforestation et de la dégradation forestière dans le site de la Maâmora au Maroc.* Version provisoire.

[29] Hiebel, M. (2005). *Fundamentals of vector network analysis.* Germany. Rohde and Schwarz, Sixth edition (2014). 420 pages.

[30] Himpens, S. (2015). *Impacts de la profondeur d'apparition de la couche d'argile sur le succès de reboisement en chêne-liège en forêt de Maâmora (Maroc).* Mémoire de fin d'études, UCL. 116 pages.

[31] Houston Durrant T., de Rigo, D. and Caudullo, G. (2016). *Quercus suber in Europe: distribution, habitat, usage and threats.* European Atlas of Tree Species. Luxembourg. pp 164-165.

[32] Jol, H.M. (2009). *Ground-penetrating radar: theory and applications.* Amsterdam: Elsevier Science. 508 pages.

[33] Lahssini, S., Lahlaoi, H., Alaoui, H.M., Hlal, E.A., Bagaram, M. and Ponette, Q. (2015). *Predicting cork oak suitability in Maâmora forest using random forest algorithm.* Journal of Geographic Information System, Vol.7. pp 202-210.

[34] Lambot, S., Slob, E.C., van den Bosch, I., Stoeckbroeckx, B. and Vanclooster, M. (2004). *Modeling of ground-penetrating radar for accurate characterization of subsurface electric properties.* IEEE Transactions on geoscience and remote sensing, Vol. 42(11). pp 2555-2568.

[35] Lambot, S., Rhebergen, J., van den Bosch, I., Slob, E.C. and Vanclooster, M. (2004). *Measuring the soil water content profile of a sandy soil with an off-ground monostatic ground penetrating radar.* Vadose Zone Journal, Vol.3. pp 1063-1071.

[36] Lambot, S., Antoine, M., van den Bosch, I., Slob, E. C. and Vanclooster M. (2004). *Electromagnetic inversion of GPR signals and subsequent hydrodynamic inversion to estimate effective vadose zone hydraulic properties.* Vadose Zone Journal, Vol.3. pp 1072-1081.

[37] Lambot, S., Antoine, M., Vanclooster, M. and Slob, E.C. (2006). *Effect of soil roughness on the inversion of off-ground monostatic GPR signal for noninvasive quantification of soil properties.* Water Resources Research, Vol. 42. 10 pages.

[38] Lambot, S. and André, F. (2014). *Full-wave modeling of near-field radar data for planar layered media reconstruction.* IEEE Transaction on Geoscience and remote sensing, Vol 52, NO.5. pp. 2295-2303.

[39] Lambot, S. (2018). *VI. Méthodes diélectriques de la teneur en eau du sol.*, BRES2102, Hydrodynamique des sols. UCL. pp 12, 32.

[40] Laoouina, A., Nafaam R. and Watfeh, A. (1997). *Occupation des sols et dégradation des terres, le cas de la Mamora et de ses bordures.* In: Méditerranée, Tome 86. Impact anthropique en milieu méditerranéen. pp 45-51.

[41] Lepoutre, B. (1965). *Régénération artificielle du chêne-liège et équilibre climacique de la subéraie en forêt de la Mamora.* Annales de la recherche forestière au Maroc, Rapport annuel, Tome 9. 185 pages.

[42] Lepoutre, B. (1967). *Excursion au Maroc, description des régions traversées.* Les cahiers de la recherche agronomique, Vol.24, Tome 1, Deuxième partie, Chap. VII. pp 279-295.

[43] Lopera, O., Slop, C., Milisavljecvic, N. and Lambot, S. (2007). *Filtering soil surface and antenna effects from GPR data to enhance landmine detection.* IEEE Transactions on geoscience and remote sensing, Vol. 45(3). pp 707-717.

[44] Mallahzadeh, A.R. and Karshenas, F. (2009). *Modified tem horn antenna for broadband applications.* Progress in electromagnetics research, PIER 90. pp 105-119.

[45] Marion, J. (1951). *La régénération naturelle du chêne-liège.* Annales de la recherche forestière au Maroc, rapport annuel. Rabat. pp 25-57.

[46] Metro, A. and Sauvage, Ch. (1957). *Observations sur l'enracinement du chêne-liège en Maamora (Maroc occidental).* Annales de la recherche forestière au Maroc, Tome 5. Rabat. pp 4-25.

[47] Minet, J., Bogaert, P., Vanclooster, M. and Lambot, S. (2012). *Validation of ground penetrating radar full-waveform inversion for field scale soil moisture mapping.* Journal of hydrology 424-425 (2012). pp 112-123.

[48] Minet, J., Lambot, S., Delaide, G., Huisman, J.A., Vereecken, H. and Vanclooster, M. (2010). *A generalized frequency domain reflectometry modeling technique for soil electrical properties determination.* Vadose Zone Journal, Vol. 9. pp 1063-1072.

[49] Monition, L. (s.d.) *Bilan des eaux souterraines profondes de la plaine du Rharb.* Office national des irrigations Rabat. pp 438-441.

[50] Mustapha, B. and El Houssine, J. (2013). *Atelier pour définir et adopter une méthodologie commune pour les analyses de vulnérabilité des sites pilotes du projet FFEM, "Optimiser la production de biens et services par les écosystèmes boisés méditerranéens dans un contexte de changements globaux".* Présentation du site pilote MAAMORA (Maroc). Solsona, Espagne: 27-31 Mai 2013.

[51] Pauwels, D. (2001). *Le VERTEX: une nouvelle génération de dendromètres multi-usages.* Note technique forestière de Gembloux n^{o}1. FSAGx - mai 2001. 13 pages.

[52] Reynders, J.J. (1972). *A study of argillic horizons in some soils in Morocco.* Geoderma, 8. Utrecht (The Netherlands). pp. 26-279.

[53] Rondeux, J. (1993). *La mesure des arbres et des peuplements forestiers.* Les Presses agronomiques de Gembloux, 1ère édition. 522 pages.

[54] Roose, E., Sabir, M. and Laouina, A. (2010). *Gestion durable des eaux et des sols au Maroc.* Marseillle: IRD Editions. 316 pages.

[55] Said, L., Najib, G. and Assmaa, A. (2010). *Towards a coordinated development of the forest in Maamora, Morocco.* Kastamonu Univ., Journal of Forestry Faculty, Vol.10(2). pp 172-179.

[56] Texier, J-P., Lefèvre, D. and Raynal, J-P. (1992). *La formation de la Maamora. Le point sur la question du Moulouyen et du Salétien du Maroc Nord-Occidental.* In: Quaternaire, Vol.3(2). pp 63-73.

[57] Topp, G.C., Davis, J.L. and Annan, A.P. (1980). *Electromagnetic determination of soil water content: Measurements in coaxial transmission lines.* AN AGU Journal. pp 574-582.

[58] United States Department of Agriculture (USDA) (s.d.) *Soil texture calculator, NRCS Soils.* Natural Resources Conservation Service Soils. `https://www.nrcs.usda.gov/wps/portal/nrcs/detail/soils/survey/?cid=nrcs142p2_054167` viewed on 15/04/2018.

Using GPR to analyze regeneration success of cork oaks in the Maâmora forest (Morocco)

Présenté par Aurore de Mahieu

UCL
Université catholique de Louvain

Abstract

Maâmora forest is considered as one of the world's largest cork oak forest. Located in North-West Morocco, it covers a total area of 133 000 ha. The forest consists of about 65 000 ha of cork oaks, while the rest of its area is covered by eucalyptus, acacias and maritime pines. In the past several decades, it has been suffering from degradation, yet it plays an important economic and social role. Studies identified that water balance (climate and soil factors) is one of the main factor that regulates the success of cork oak regeneration. In fact, the forest's soil is composed of a more or less deep sand layer (0.3 m - 6 m) laying above a clay layer.

The overall goal of this thesis is to study the relationship between the growth of cork oaks and soil factors using GPR techniques. More specifically, it consists of first, setting up a lightweight frequency domain GPR then, studying the vigor of trees and detecting the soil properties that can lead to successful cork oak regeneration. The forest plot chosen for this study is located in B canton of Maâmora forest (plot VI-6) and has a high variability in terms of tree growth and regeneration success. It is also characterized by variable sand and clay layer depths.

Two different GPR were used in this study: a lightweight frequency domain GPR, to map the surface soil moisture and a time domain commercial GPR, to detect soil textural transitions in depth. Results show that both GPR provided information on soil properties. Generally, the most humid areas were characterized by successful regeneration plots of cork oaks. Soil texture (red sands), clay layer depth (< 3.5 m), and clay structure (red clays of Maâmora) are among the factors that influence cork oak growth. Hence, GPR provided valuable results even though further soil analyses would allow to fully understand the soil water hydrodynamics.

Key-words: cork oak, GPR, clay layer, water retention, Maâmora

Année académique 2017-2018

AGRO LOUVAIN
BIOINGÉNIEURS